ALMA MATER STUDIORUM · UNIVERSITY OF BOLOGNA

School of Science
Department of Physics and Astronomy
Master Degree in Physics

Study and characterisation of Low Gain Avalanche Diode (LGAD) for the Time-of-Flight system of the experiment ALICE 3 at LHC

Supervisor:
Prof. Andrea Alici

Co-supervisor:
Dr. Sofia Strazzi

Submitted by:
Edoardo Rovati

Academic Year 2023/2024

Abstract

This thesis presents an analysis of the performance of ultra-thin Low-Gain Avalanche Detector (LGAD) prototypes. The analysis consists of an experimental verification of the expected characteristics of these sensors that have become a workhorse for high resolution silicon timing detectors for charged particles and that have been selected as potential candidates for the Time-Of-Flight (TOF) system of the ALICE 3 experiment. As the successor to the current ALICE experiment at CERN, ALICE 3 is envisioned as the prototype for a new generation of heavy-ion collision experiments, and it is expected to start data collection in LHC Run 5 in 2035.

The study involved samples of LGAD sensors manufactured by Fondazione Bruno Kessler (FBK) with varying thicknesses, ranging from 50 μm to 15 μm. A key focus of the research was the innovative concept developed in Bologna, known as the double LGAD, designed for timing applications. The characterization of these sensors included standard timing applications with ultra-thin 20 μ- and 15 μ-thick, where the time resolution was measured with charged particles in dedicated beam tests. The results confirmed the excellent temporal performance of these sensors, with resolutions around 20 ps.

Additionally, a study on the energy resolution of these sensors was conducted using an ^{55}Fe source, which emits photons at approximately 6 keV. A comparison of the results obtained with the 20 μm and 15 μm sensors by using charged particles on beam was then carried out to observe how these sensors behaved. The results, including a first comprehensive study of the LGAD energy resolution as a function of gain and sensor thickness, are presented and discussed in details.

Introduction

The A Large Ion Collider Experiment (ALICE) at the Large Hadron Collider (LHC) has as one of its principal objectives the investigation of the Quark-Gluon Plasma (QGP). To deepen its research objectives, ALICE has undergone significant upgrades, particularly in its Inner Tracking System (ITS). Looking forward, the ALICE 3 experiment represents the next step and would replace the current ALICE detector in 2034. Building upon the advancements achieved with the upgraded ITS, ALICE 3 is a new generation experiment in heavy-ion collision physics, scheduled to start data-taking operations for LHC Run 5 in 2035. It aims to a significant advancement in our efforts to comprehend the challenging physics of ultrarelativistic heavy-ion experiments. The proposed experimental apparatus will be constructed entirely using state-of-the-art silicon technologies, with the aim of delivering exceptional spatial and temporal resolution. ALICE 3 boasts superior particle identification with a low-mass curved retractable tracking system with exceptional pointing and momentum resolution. This improved capability opens the door to a multifaceted physics programme, ranging from measurements with electromagnetic probes at ultra-low transverse momenta to precision studies in the fields of charm and beauty. The physics objectives of experiment demand a Time-Of-Flight (TOF) system with a a time resolution at least of 20 ps, never reached until now with a silicon detector.

Among the technologies considered most promising for such a detector are Silicon PhotoMultipliers (SiPM) and Low Gain Avalanche Detectors (LGAD). This thesis activity will focus on studying the performance of LGAD sensors with different thicknesses, from standard 50 μm to ultra-thin 20 and 15 μm. The thesis will include the functional characterisation of these silicon sensors with internal gain in the laboratory, through measurements of current and the measurement and study of temporal resolution through measurements with charged particle beams at the CERN beam facilities with a focus on 20 and 15 μm sensors. In addition, it is planned to study the energy resolution of all sensors using an ^{55}Fe source. Together, these measurements should lead to a better understanding of the properties of these sensors and possibly to the choice of LGADs as the technology that best meets the physical requirements for the timing layer of ALICE 3.

Contents

List of Figures

Chapter 1

The nuclear matter at extremely high energy density

ALICE (A Large Ion Collider Experiment) [1]-[2] is a general-purpose experiment at the CERN Large Hadron Collider (LHC) optimized to study the physics of ultrarelativistic heavy-ion collisions in order to recreate the conditions similar to those of early universe. The main goal of the ALICE Collaboration is to study the microscopic dynamics of the strongly interacting matter [3] produced in such collisions and, in particular, the properties of the Quark-Gluon Plasma (QGP) [4], a state of matter where quarks and gluons are almost-free.

1.1 Introduction to QGP

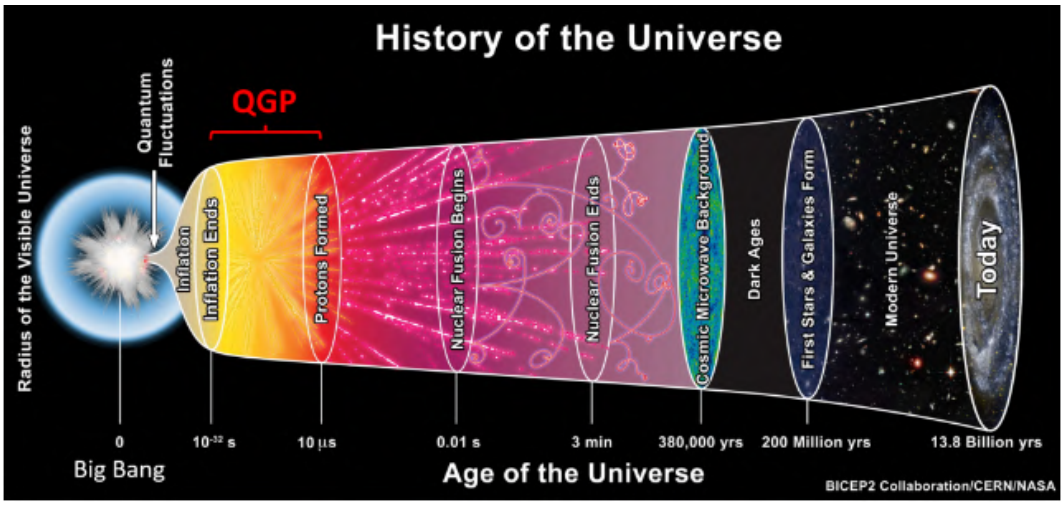

Figure 1.1: Schematic view of the universe's evolution: the QGP phase is a remarkable event in the history of the universe.

The basis of matter, composed of atoms with electrons orbiting around nucleus of protons and neutrons, originated in the Big Bang, an event characterised by colossal energy density and temperature (see figure 1.1). In the early moments, quarks, antiquarks and gluons formed a QGP before combining into hadrons. This process, known as hadronisation, occurred when the energy density of the universe went below 1 GeV/fm^3 and the temperature cooled to around 170 MeV. Following hadronization, the temperature decreased to approximately 100 keV over about 200 seconds, enabling the formation of small atoms. The first few minutes determined the elemental

composition of the early universe through chemical freeze-out. Around 300,000 years after the Big Bang, electrons and nuclei combined following primordial nucleosynthesis. This caused thermal freeze-out as the temperature reached approximately 3000 K, resulting in the decoupling of electromagnetic radiation and the cosmic microwave background observed today.

The enduring evidence of the Big Bang includes the Hubble expansion and density fluctuations seen in the distribution of celestial bodies. The cosmic evolution is reconstructed through observations, studying the Hubble expansion rate, microwave background spectrum, original nuclear abundances, and contemporary density fluctuations. Direct observation of events preceding 300,000 years after the Big Bang remains challenging due to the early universe's opacity. Relativistic heavy-ion collisions play a crucial role in recreating the quark-gluon plasma, offering insights into the universe's initial microseconds.

1.2 The QGP and Strongly Interacting Matter

At the forefront of high-energy nuclear physics lies the motivation to unravel the complexity of strongly interacting matter, manifesting in the exploration of the phase diagram, figure 1.2. The theory that governs the strong nuclear force, Quantum Chromodynamics (QCD) [3], predicts a significant transition from the usual hadronic matter to an exceptional state known as the QGP [5]. In this plasma phase, quarks and gluons that are normally confined in hadrons can move freely in large volumes because they are quasi-free. As a result of this phase transition, the chiral symmetry present in the QCD Lagrangian is restored, which leads to quarks with no effective mass.

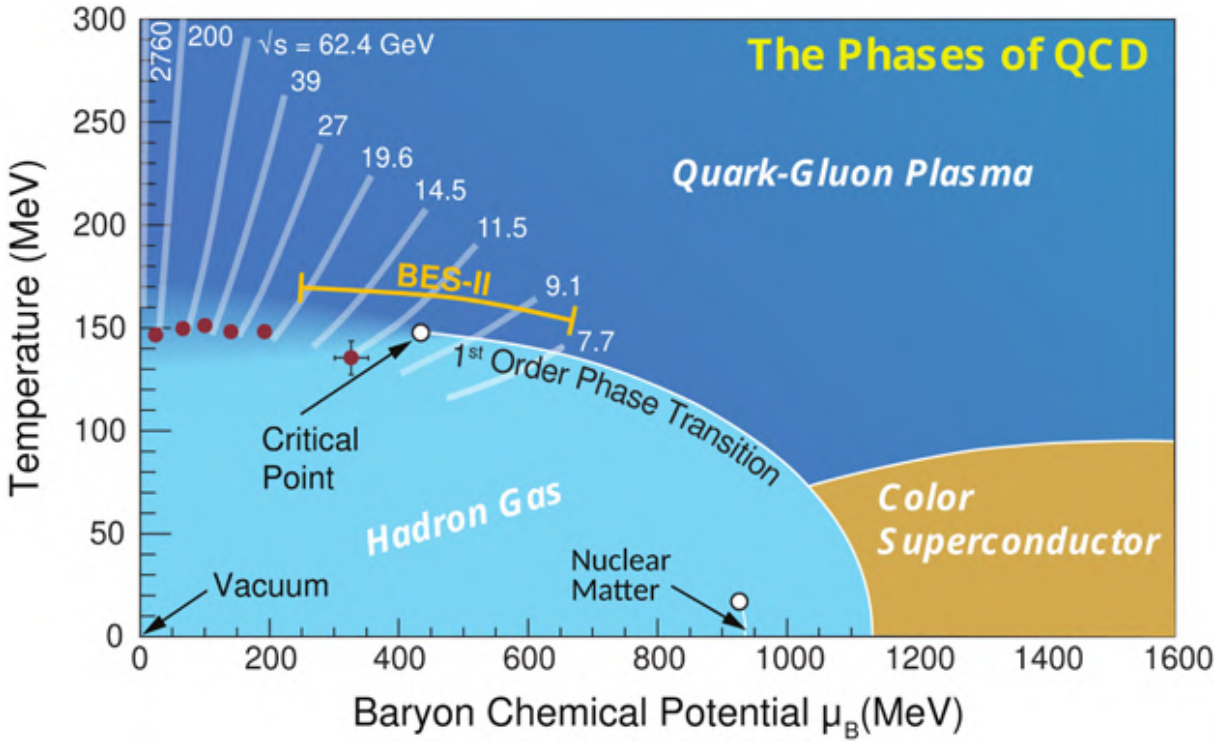

Figure 1.2: Diagram illustrating the phase structure of strongly interacting matter based on temperature and net baryon chemical potential.

The phase of quark-gluon plasma [6], in figure1.2, is present at high temperatures and high energy densities, with a transition to an hadron gas along the shown line.

High energy heavy-ion experiments investigate this baryon-rich regime. At low temperatures and finite densities, the transition from liquid-gas [7] associated with bound nuclear matter occurs, in addition to the existence of cold neutron stars containing a superconducting colour phase [8], hypothetically, at very high densities. Heavy-ion experiments at intermediate and low beam energies explore the first-order phase transition with a critical endpoint predicted at finite net baryon densities.

1.2.1 Ultra-relativistic Nucleus-Nucleus Collisions

Ultra-relativistic nucleus-nucleus collisions offer a unique opportunity to study QCD in extreme conditions. These collisions, like those observed in the ALICE [9] at CERN, allow for the recreation of the QGP in the laboratory. An example of a lead-lead collision recorded by ALICE is shown in figure 1.3.

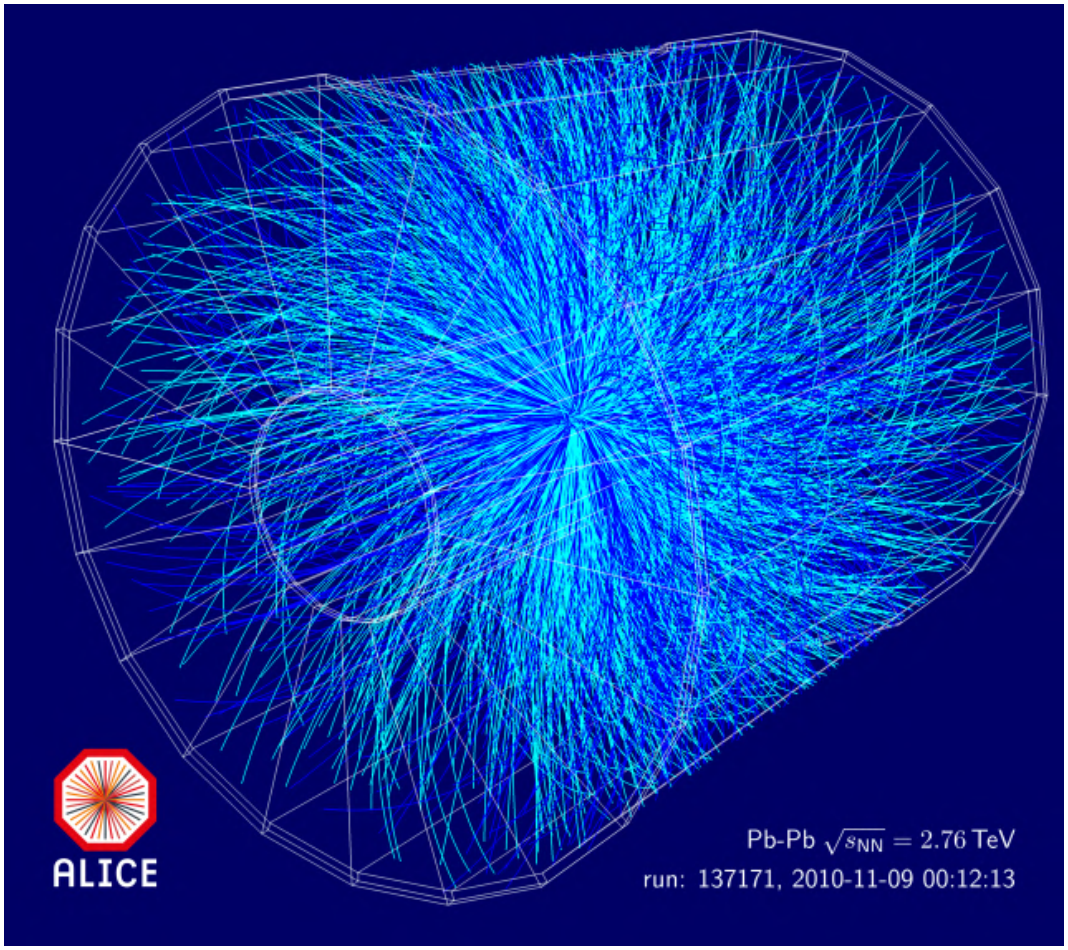

Figure 1.3: Lead-Lead ion collision recorded by the ALICE detector in November 2010 at a center of mass energy per colliding nucleon-nucleon pair of 2.76 TeV taken from [10].

The evolution of the QGP, from the initial collision to the final free-streaming of particles, is summarized schematically in figure 1.4, depicting the interplay of partonic interactions, hydrodynamic expansion, and hadronization. Such evolution can be described as a sequence of stages, each contributing to the overall understanding of QCD and the properties of QGP. These stages include:

- The **initial state**, defined by the wave-functions of the colliding nuclei, which are universal and independent of the specific scattering process [11]-[13].

- The **large-Q^2 interactions** of partons from the projectiles, followed by **smaller-Q^2 interactions** generating a pre-equilibrated parton gas.
- **Equilibration and expansion** of the QGP, during which the partons become quasi-free, and chiral symmetry is restored [14]-[15].
- The formation of **hadrons** from the cooling QGP [16].
- **Chemical freeze-out**, where the inelastic interactions cease, fixing the particle species composition [17].
- **Kinetic freeze-out**, where elastic hadronic interactions end, fixing the momenta of the particles [18].
- **Free-streaming** of stable particles to the detectors for experimental measurement.

The initial state consists of two Lorentz-contracted nuclei colliding with each other at ultra-relativistic speeds, generating a dense overlap region with high energy and entropy. The number of nucleons participating in the collision, N_{part}, and the number of inelastic nucleon-nucleon collisions, N_{coll}, depend on the impact parameter b, which measures the distance between the centers of the colliding nuclei. Nucleons not involved in the collision are referred to as *spectators* and continue traveling along the beam direction.

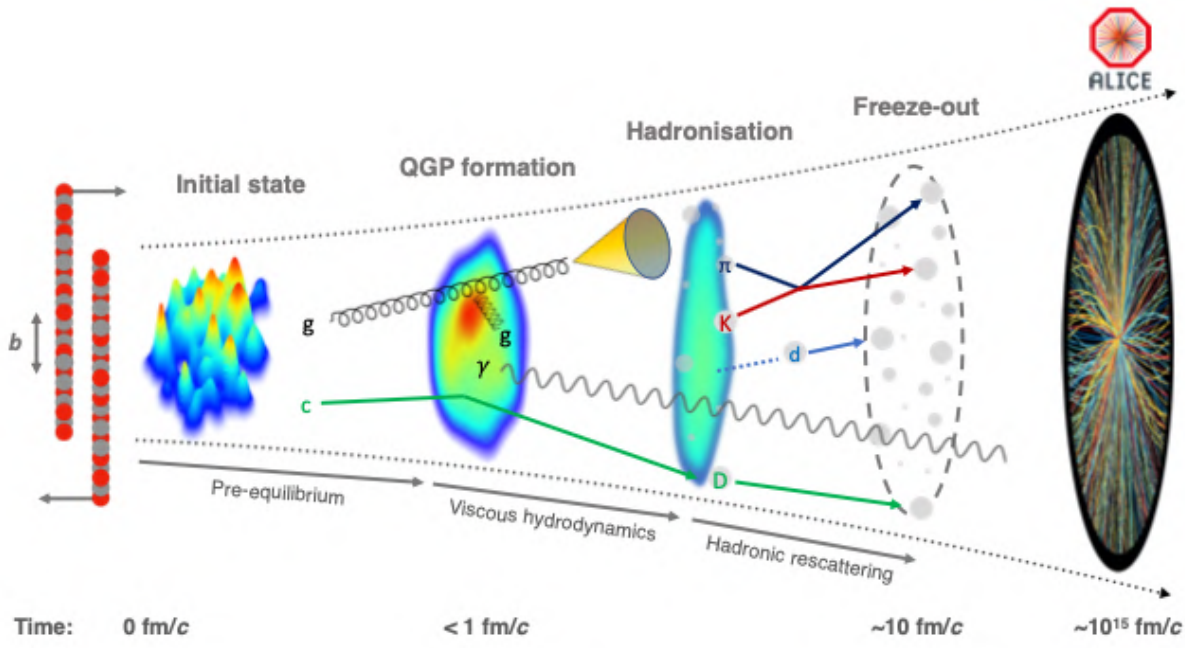

Figure 1.4: The evolution of a heavy-ion collision at LHC energies.

During the collision, the incident nuclei are composed of quarks and antiquarks, which generate strong color fields. As the two nuclei collide, partons (quarks and gluons) are excited, and an extremely dense region forms in the overlap. This region reaches such high energy density that it creates the QGP, a collective medium characterized by a low viscosity-to-entropy density ratio, η/s [19], and strong coupling between quarks and gluons. The QGP undergoes a dynamic evolution, expanding as a relativistic hydrodynamic fluid.

1.2.1.1 Parton Interactions in QGP

The interactions within the QGP can be classified according to the momentum transfer scale Q^2. Large-Q^2 interactions, involving high-momentum partons, lead to the creation of high-energy quarks and gluons, which subsequently interact with the medium [20]. These interactions provide crucial information about the opacity of the QGP. Partons lose energy through both radiative and elastic processes as they traverse the QGP. The energy loss is influenced by the color charge, mass, momentum, and path length of the partons. For instance, heavy quarks, such as charm and beauty, produced in the initial hard scatterings, may form bound quark-antiquark states, known as *quarkonia*. However, the presence of color charge in the QGP weakens the binding force, leading to *quarkonium suppression*.

Jets, arising from the fragmentation of high-energy partons [21], also provide insight into QGP properties. The pattern of jet fragmentation in the QGP differs from that in vacuum, as the QGP alters the parton shower development through multiple interactions. The formation of hadrons from parton jets is one of the primary signals studied in heavy-ion collisions.

1.2.1.2 Hydrodynamic Expansion and Flow

After the QGP is created, it expands due to pressure gradients arising from the non-uniform energy distribution in the initial state [22]. This leads to both *radial flow*, where the pressure pushes outward symmetrically, and *anisotropic flow*, where the azimuthal distribution of final-state particles reflects spatial asymmetries in the collision zone. These asymmetries are converted to momentum anisotropies by the QGP's hydrodynamic behavior. The expansion is also influenced by the QGP's *bulk viscosity*, which resists changes in volume, and *shear viscosity*[23], which resists deformations.

In addition to hydrodynamic effects, strong magnetic fields are generated during the collision due to the movement of charged nuclei at relativistic speeds. The *Chiral Magnetic Effect* (CME) [24] results from the interaction of quarks with these magnetic fields, leading to a separation of positive and negative charges along the field lines. Thermal radiation in the form of photons [25] and lepton-antilepton pairs, produced throughout the QGP's evolution, provides direct information about the temperature of the system at various stages.

1.2.1.3 Hadronization and Freeze-Out

As the QGP cools, it eventually undergoes *hadronization* [26], forming color-neutral hadrons such as pions, kaons, and protons. The transition from QGP to hadronic matter is expected to be a smooth cross-over, with hadronization occurring at different times and spatial locations within the expanding system. The temperature at which inelastic interactions cease, known as the *chemical freeze-out temperature*, T_{chem}, fixes the particle species composition. Beyond this point, only elastic interactions remain, and these continue until the *kinetic freeze-out temperature*, T_{kin}, is reached, marking the end of significant particle collisions.

After kinetic freeze-out, the particles move freely towards the detectors [27]. Approximately 10^{15} fm/c after the initial collision, these particles are measured, allowing researchers to analyze the properties of the QGP, such as its temperature, viscosity, and expansion dynamics.

1.3 Physical Objectives and Innovative Technology of ALICE 3

The main goal of the ALICE [28] Collaboration is to study the microscopic dynamics of the strongly interacting matter produced in heavy-ion collisions, and in particular the properties of the QGP. The LHC heavy-ion campaigns of Runs 1 and 2 have already led to decisive advances in our understanding of the properties of the QCD phase diagram and the QGP [2]-[29]. With the current ALICE 2 and the future ALICE 2.1 upgrade, LHC Runs 3 and 4 [30] will allow further systematic measurements of fundamental properties for our understanding of the QGP. However, despite the rich physics programme planned, fundamental questions will remain unanswered, and addressing such questions will require substantial improvements in detector performance and data rate, necessitating a next-generation heavy-ion experiment, the so-called ALICE 3 upgrade, planned for LHC Run 5 and beyond.

ALICE 3 [31], which is scheduled to be completed in 2034 after Long Shutdown 4 with data acquisition beginning in 2036, represents a significant step forward in our efforts to understand the complex properties of QGP. The new detector would be positioned around the nominal IP2. The primary physics goal of ALICE 3 is to achieve a deep understanding of the underlying mechanisms that affect the different stages of heavy-ion collisions, from the early stage of medium formation to the diffusion, thermalisation and hadronisation. The main new studies in the QGP sector focus on the production of low transverse momentum heavy flavours [32], including beauty hadrons, multi-charm baryons [33]-[34] and charm-charm correlations, as well as measurements of net quantum number fluctuations to constrain the susceptibilities of the QGP, and precise measurements of dilepton emission to probe the time evolution of the QGP, the early-stage temperature and the mechanism of chiral symmetry restoration. Besides QGP studies, ALICE 3 can uniquely contribute to hadronic physics with femtoscopic studies [35] of the interaction potentials between charm mesons and the search for charmed nuclei, and to fundamental physics with precise experimental tests of Low's theorem for ultra-soft photon emission [36]-[37] and the search for axion-like particles (ALP) in ultra-peripheral heavy-ion collisions via light-by-light scattering measurements.

1.3.1 Overview of the Large Hadron Collider

The LHC is the world's largest and most powerful particle accelerator. It is located at CERN (European Organization for Nuclear Research) near Geneva, Switzerland. The LHC occupies the same tunnel in the past housed the Large Electron Positron (LEP) collider, buried about 100 meters underground, with its lowest point reaching approximately 175 meters.

Proton beams travel quickly through the LHC ring within vacuum tubes, guided by a complex network of powerful magnets. Superconducting magnets, cooled by an extensive cryogenic system, are employed to maintain the trajectories of high-energy beams. The accelerator consists of 1232 dipole magnets, each 15 meters in length, that guide the beams, and 392 quadrupoles, spanning 5-7 meters, which focus the beams.

Four distinct points along the ring interrupt the chain of magnets. The four colossal caverns at these locations house the LHC experiments (ALICE, ATLAS, CMS, LHCb) and their associated detectors. Special X-shaped beam pipes within these caverns

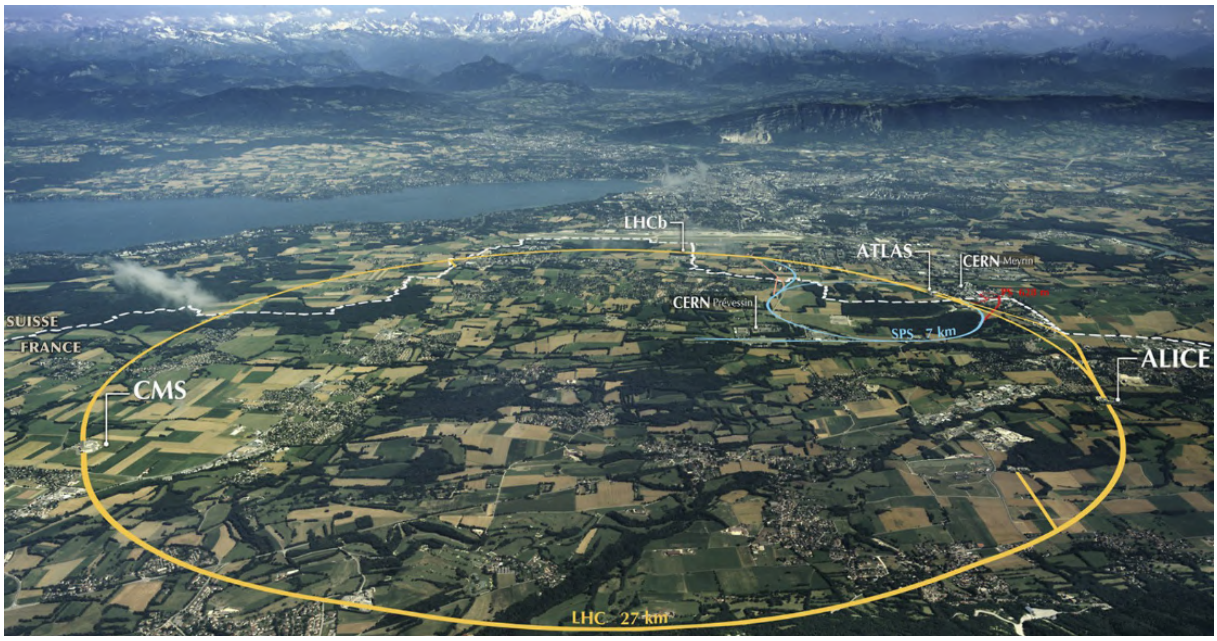

Figure 1.5: LHC ring and the four main experiments.

enable the trajectories of the two beams to intertwine and exchange positions. The beams collide at an angle of 1.5 degrees at these X-shaped junctions, allowing the particles to interact and produce new phenomena.

Unlike most of the ring, where the two LHC beams maintain separate vacuum chambers, at the collision points, they are brought together to engage in high-energy collisions. Figure 1.5 presents an updated depiction of the actual LHC ring.

1.3.2 ALICE 3: advancing Heavy-Ion Physics at the LHC

The ALICE experiment is conducted at the CERN Large Hadron Collider to investigate the physics of strongly interacting matter at extreme energy densities and temperatures.

Over the course of the first LHC Run (2009 to 2013) and the second Run (2015 to 2018), ALICE carried out a comprehensive set of QCD measurements to improve our understanding of the properties of QGP. In addition, ALICE has made discoveries including the evolution of strangeness enhancement from low-multiplicity pp to high-multiplicity Pb-Pb events and the regeneration mechanism of the $J\psi$ quark by the coalescence of charm and anti-charm quarks independently produced.

Significant upgrades to the detectors were put in place to fully exploit the scientific potential of the LHC upgrade after the Long Shutdown 2 (LS2). These upgrades include the new Inner Tracking System (ITS2) and Muon Forward Tracker, both based on Monolithic Active Pixel Sensors (MAPS) [38], new GEM-based readout chambers for the Time Projection Chamber (TPC), and the new Fast Interaction Trigger detector. Preparations for further detector upgrades during the next Long Shutdown (2025-2027) are underway, and future detector R&D programmes have started. The improved ALICE detector will address key measurements in heavy-ion collisions. These include the production of multi-charmed baryons, the elliptic flow of electron-positron pairs and the production of photons at very low momentum. However, there are still open questions in physics that need to be addressed with the upgraded machine's wide range of capabilities. The substantial increase in nucleon-nucleon luminosity at the LHC after LS4 is a promising opportunity to extend the heavy-ion programme. This gives access to

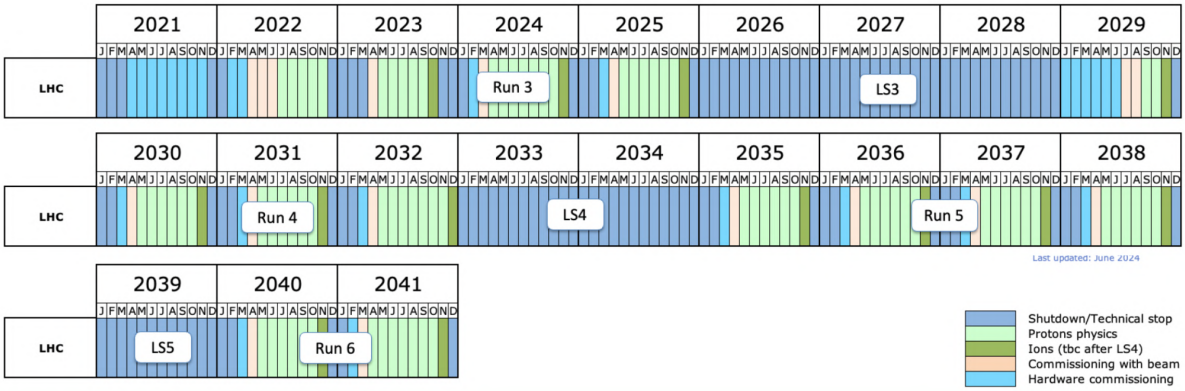

Figure 1.6: LHC schedule with the main foreseen upgrades. The red arrow indicates the scheduled ALICE 3 installation.

new probes of the QGP and heralds an era of precision in probes which have been yet scarce investigated. The maximum achievable interaction rate for the current ALICE experiment would be saturated at such luminosities. As a consequence, the current Time-Projection Chamber detector will have to be replaced by new, faster technologies. A compact next-generation heavy-ion experiment, ALICE 3, has been proposed for installation at the LHC's Interaction Point 2 during Long Shutdown 4 in 2033-2034 (LS4), starting to take data around 2035 (see figure 1.6), in order to take advantage of these interaction rates. ALICE 3 will be an all-silicon detector. Based on advances in novel silicon technologies, it will have an unprecedented low mass. This design will allow measurements in the ultra-soft region of phase space, focusing on the production of lepton pairs, photons and very low transverse momentum hadrons at the LHC.

1.3.3 ALICE 3: enhancing measurement capabilities to broaden scientific horizons

ALICE 3 represents a major leap forward with its extended capability to measure the production of leptons, photons and identified hadrons at low transverse momenta (p_T) in the range of tens of MeV/c. This improved capability opens the door to a multifaceted physics programme, ranging from measurements with electromagnetic probes at ultra-low transverse momenta to precision studies in the fields of charm and beauty. Some of the key themes proposed for ALICE 3 are outlined below.

1.3.3.1 The search for beauty in heavy-ion collisions: precision measurements

ALICE 3 will provide precise measurements of beauty mesons and baryons, providing new constraints on heavy-field transport and hadronisation, in particular on the diffusion coefficient (D_s). The theoretical control of the quark transport in the expanding QGP [39] will be improved by the larger mass of beauty quarks compared to charm quarks. The beauty measurements will provide experimental constraints on the temperature and momentum dependence of the drag coefficient, which is crucial for the understanding of the heavy quark interactions in the QGP medium [40]. Beauty's slower vanishing momentum velocity, coupled with its longer relaxation time compared to the QGP lifetime, will better constrain heavy quark propagation in later stages of medium evolution [41].

Preliminary studies indicate that, in particular at low transverse momenta, ALICE

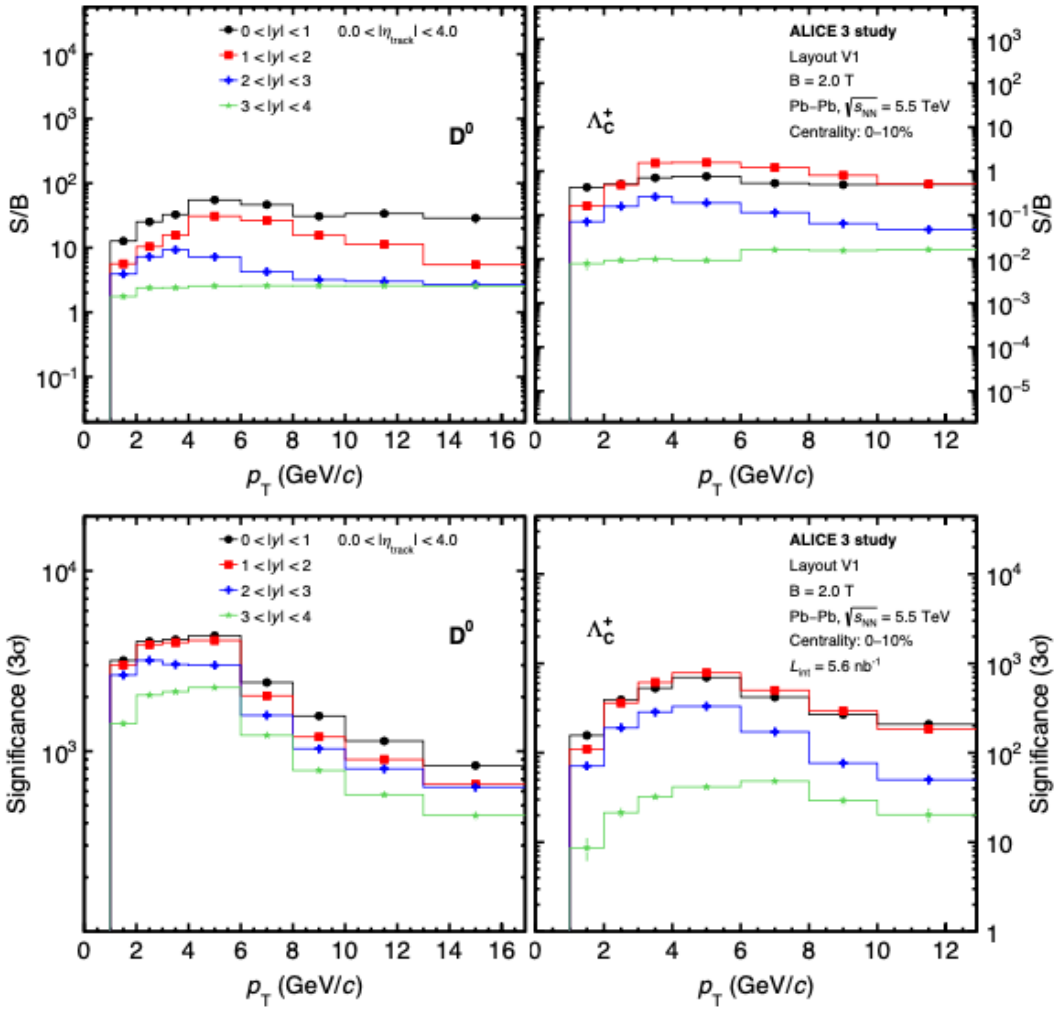

Figure 1.7: Signal to background ratio for D_0 (left) and Λ_c^+ (right) as a function of p_T in different velocity intervals in 0-10% central Pb-Pb collisions. Bottom panels: Significance evaluated by integrating signal and background in a 3σ window in invariant mass for 1 running year.

3 will significantly improve the accuracy of the reconstruction and the purity of the selection of D^0 mesons and Λ_c^+ baryons (see 1.7). An efficient separation between the phase-space region used for measurements and that considered for event characterisation will be possible thanks to the broad acceptance of ALICE 3. The broad rapidity coverage will allow the use of the Event Shape Engineering (ESE) technique to measure the differential yield of heavy-flavour hadrons in terms of transverse momentum and azimuthal asymmetry (v_2) in events with the same centrality but different bulk elliptic flow magnitudes. This extended coverage minimises the bias due to non-flow correlations and improves the ability of ESE measurements to discriminate between models.

1.3.3.2 Heavy-Flavor Dynamics: Correlations, Energy Loss in QGP

To accurately determine the transport coefficients for the QGP, it is necessary to measure the transverse momentum spectra and the azimuthal anisotropy of charm and beauty hadrons at low momenta. Although event averaging provides some sensitivity, more detailed measurements are essential to understand how heavy-flavour quarks propagate. This study investigates the correlations between heavy-flavour quarks and recoil partons to gain insight into the momentum and directional changes that char-

acterise the energy loss in the QGP [42]. Differences in energy loss between heavy quarks and light partons in the hot QCD medium have been highlighted by recent theoretical and experimental studies [43]. The emphasis will be on photon-jet measurements for the understanding of heavy quark kinematics before and after the interaction with the medium. At leading order, the azimuthal correlations of charm-anti-charm quark pairs exhibit a back-to-back configuration, while higher order processes lead to a moderate broadening around $\Delta\phi = \pi$. Precise measurements in proton-proton (pp) collisions serve as a baseline, while additional broadening in heavy-ion collisions is attributed to medium interactions. Radiative energy loss is mainly small-angle radiation, leading to limited broadening, whereas collisional processes, especially at low transverse momentum, lead to significant broadening of the initial correlation. Full equilibration would randomise the flight directions of the charm quarks, erasing any remnants of the initial correlation. Differential measurements of $D\bar{D}$ pairs in $\Delta\phi$, considered in terms of p_T, Δp_T and $\Delta\eta$, provide new constraints on the mechanisms of heavy quark parton propagation and, in particular, on the process of charm equilibration in the QGP. The expected performance of the ALICE 3 detector for such measurements is discussed, and the prospects for $B\bar{B}$ correlations are explored, while a study of the expected performance of ALICE 3 for the measurement of $\Delta\phi$ correlations of $D\bar{D}$ pairs is presented in figure 1.8. Meeting the stringent requirements of heavy flavour correlation measurements in heavy-ion collisions requires advanced detector design [44].

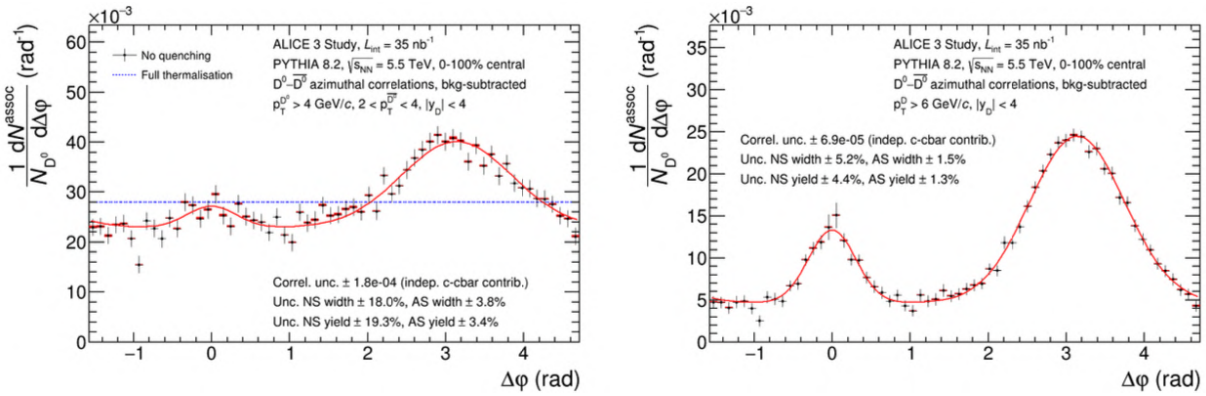

Figure 1.8: Azimuthal distribution of $D\bar{D}$ pairs with p_{T1} > 4 GeV/c, 2 < p_{T2} < 4 GeV/c (left panel) and p_T > 6 GeV/c (right panel) and |y| < 4 in minimum bias Pb-Pb collisions.

1.3.3.3 A comprehensive study of bound state formation and dissociation

A detailed study of the mechanisms involved in the formation and dissociation of bound states is crucial for a comprehensive understanding of heavy quark dynamics in QGP.

Ultra-low momentum quarkonium states: ALICE 3 is expected to have unique capabilities for reconstructing quarkonium states [45] down to p_T = 0. It is well suited for precise measurements of low-energy photons (0.5 GeV and below), allowing accurate studies of $\chi_c \rightarrow J/\psi\gamma$ and $\chi_b \rightarrow \Upsilon\gamma$ in both proton-proton and heavy-ion collisions over a wide kinematic range at the LHC. Figure 1.9 is an illustration of the expected performance for the analysis of χ_c. Although the detailed performance of ALICE 3 for pseudoscalar states has not yet been thoroughly investigated, potential channels such as hadronic decays, for example $\eta \rightarrow p\bar{p}$ and $\eta \rightarrow \Lambda\bar{\Lambda}$, may be possible despite their relatively small branching ratios.

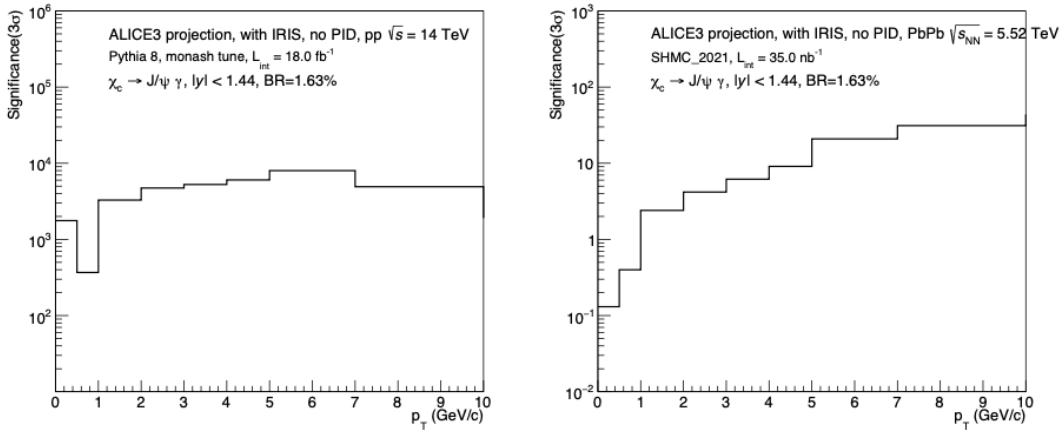

Figure 1.9: Significance of the χ_c signal as a function of transverse momentum in pp collisions at $\sqrt{s}$ = 14 TeV and in Pb-Pb collisions at $\sqrt{s_{NN}}$ = 5.5 TeV .

Ultra-low transverse momentum exotic states: The investigation of exotic Quantum Chromodynamic states in nuclear collisions holds significant importance for QCD physics [46]-[47]. Therefore, measuring the production of χ_{c1} (3872) at low p_T values, in particular p_T < 5 - 6 GeV/c, is one of the primary goal of ALICE 3. This region is critical because it is expected to have a substantial increase in yield. It is also inaccessible to other LHC experiments. To achieve this goal, it is necessary to identify muons down to a $p_T \simeq$ 1.5 GeV/c at η = 0 and to ensure high efficiency in the detection of hadronic decay products within a large pseudorapidity acceptance.

1.3.3.4 Study of electric conductivity in ALICE 3

The QGP has a fundamental property known as electrical conductivity [48] (σ), which relates the electric current density (j_μ) to the electric field ($\langle E_i \rangle$): $\langle j_i \rangle = \sigma \langle E_i \rangle$). The electrical conductivity is expected to be approximately proportional to temperature, with most theoretical computations predicting moderate temperature (T) dependence up to several times the critical temperature (T_c). Theoretical predictions vary widely. They are roughly characterised by $0.001 \lesssim \sigma/T \lesssim 0.1$ [49]. Experimental constraints are therefore crucial. The electrical conductivity of the quark gluon plasma plays a key role in the time evolution of the electromagnetic fields in non-central heavy-ion collisions produced by spectator protons. To understand phenomena such as the chiral magnetic effect associated with strong magnetic fields, an accurate knowledge of the electrical conductivity is essential.

Theoretical models link electrical conductivity to the conductivity peak of the spectral function, leading to increased production of low-mass, low-momentum photons and dielectron pairs. At present, the experimental constraints on the electrical conductivity are limited due to background contributions from the decays of the neutral pion, the η meson and other short-lived hadrons. Preliminary studies show that the background from the Dalitz decays of the neutral pion can be reduced by careful selection of the transverse momentum and mass. ALICE 3 aims to access the peak of thermal conductivity in the dielectron channel by applying these selections and identifying low-momentum electrons using the inner time-of-flight (TOF) layer. In addition, the use of photon Hanbury-Brown-Twiss correlations is being explored to access the signal in the photon channel, using photon pairs detected by the electromagnetic calorimeter and the conversion method in the tracker, as well as pairs reconstructed by the forward conversion tracker. To address this experimental challenge and to improve our under-

standing of the electrical conductivity in the QGP, detailed physics performance studies are underway.

1.3.3.5 Exploring Soft Photons in High-Energy Nuclear Collisions

In high-energy nuclear collisions, photons are essential for studying the hot QGP. They provide additional information because they escape without interacting with the QCD medium. The spectrum of the direct photons at low transverse momentum is mainly influenced by the thermalisation of the hadron gas after the collisions and, to a greater extent, by the QGP in ultra-relativistic heavy-ion systems. The production of thermal photons is a function of the properties of the hot medium, and this provides insight into the expansion and temperature of the medium, which is crucial for the study of the phase diagram of hadronic matter [50]-[51].

In a collider environment, due to significant background contributions from photons from hadron decays (mainly π^0), electron bremsstrahlung in the detector material and ultraperipheral collisions, the study of true soft photons in the low p_T region is challenging. At present, only 1 GeV is available for measurements in heavy-ion collisions. ALICE 3's ultra-low-mass tracker will extend the photon transverse momentum range

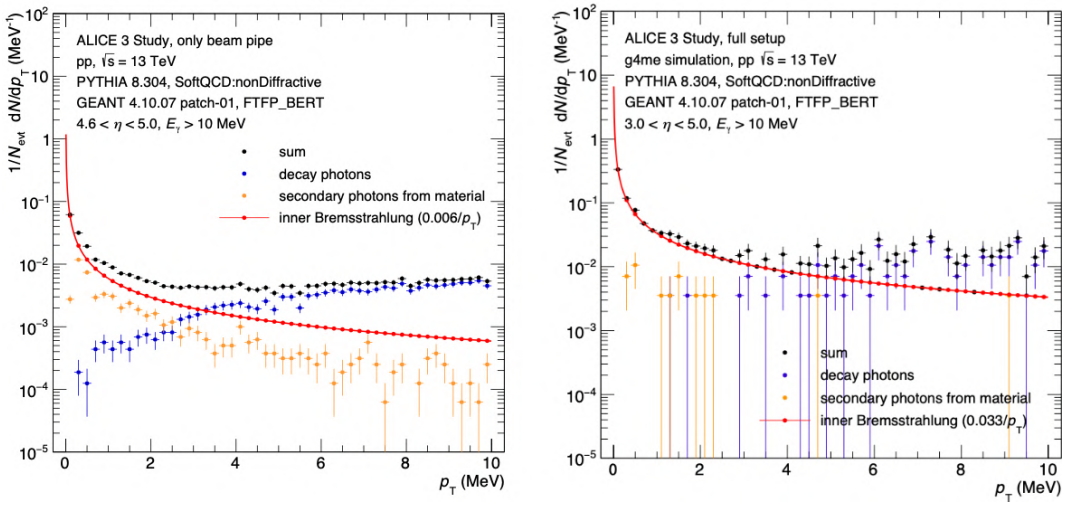

Figure 1.10: Transverse momentum spectra of signal and background photons in proton-proton (pp) collisions at a center-of-mass energy of $\sqrt{s}$ = 13 TeV, at forward rapidities. The background comprises photons originating from the decay of particles (π^0, η) and bremsstrahlung photons produced in front of the Forward Conversion Tracker.

to 50-100 MeV/c, allowing predictions for QGP radiation to be tested in unexplored phase space. The experiment will push the limits even further with a small spectrometer designed for forward rapdity (3.5 < $|\eta|$ < 5), allowing measurements in the range 1 MeV/c < p_T < 100 MeV/c. The measurement of low transverse momentum electromagnetic radiation below 100 MeV/c and approaching 1 MeV/c is crucial. The predictions of simple theories based on a few assumptions are not sufficient. Fundamental 'soft theorems' in quantum field theories link the production of such low p_T photons to the charged final state. Low's theorem, which is central to the consistency of quantum field theory, predicts a controlled divergence of the number of soft photons towards low p_T. To test these predictions and identify any deviations that may indicate fundamental gaps in understanding, experimental sensitivity to photons in this p_T region is crucial. The ALICE 3 experiment is well suited for measuring the infrared limit of two important quantum field theories: QED and QCD. To achieve this, it is necessary to have a dedicated detector for ultra-soft photons in the forward direction, together with a coverage

of charged particles over more than 8 units of rapidity. For the study of ultra-soft photons, this setup will also allow the selection of exclusive diffractive and ultra-peripheral collisions. The expected background levels for ultra-soft photon measurements with the proposed detector are shown in figure 1.10.

1.3.4 ALICE 3 detectors system

In this section, general overview of the ALICE 3 detector [31] is reported, as portrayed in figure 1.11, while in figure 1.12 the detectors requirements are shown. The detector comprises various essential elements, each intended to serve distinct purposes in the experiment.

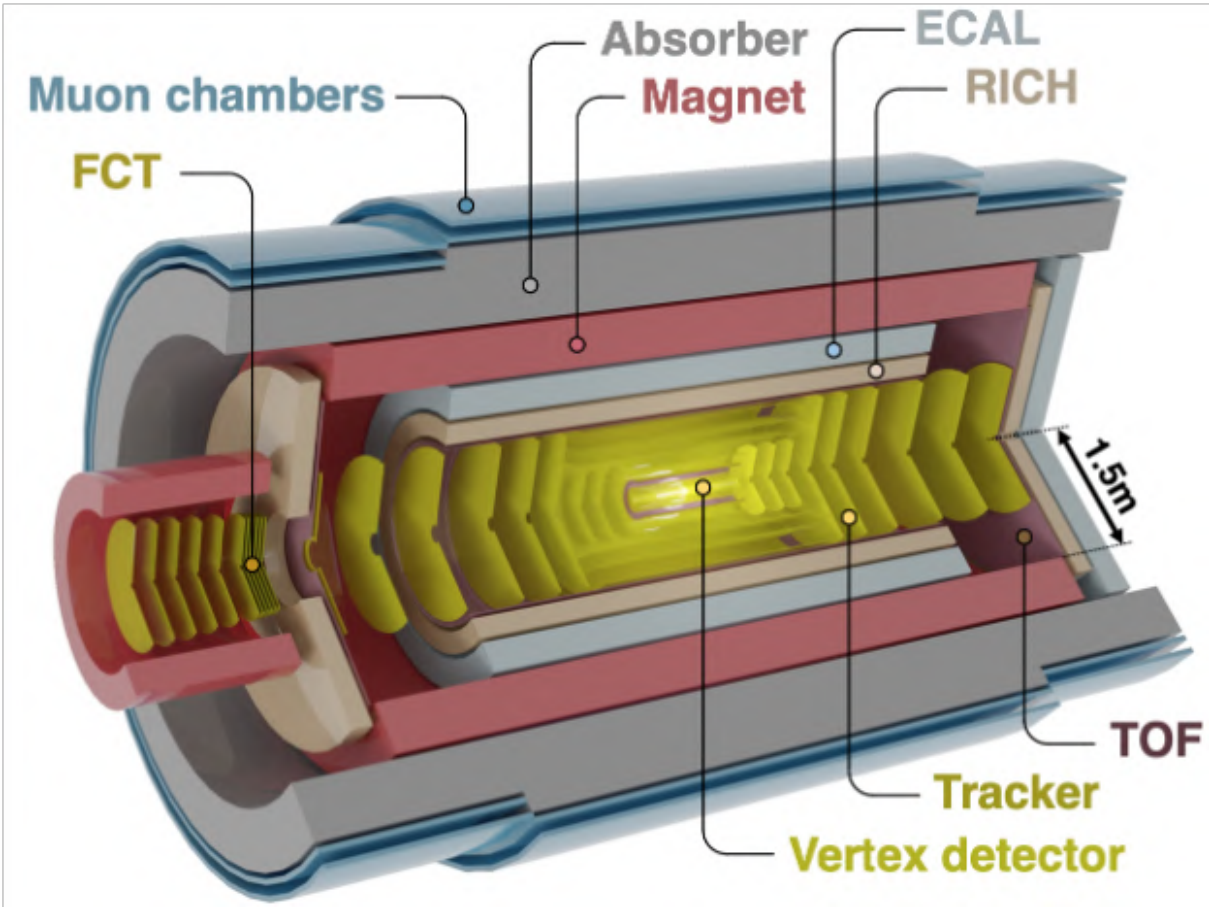

Figure 1.11: Schematic representation of the ALICE 3 Detector Concept. The detector's core consists of a silicon tracker with cylinders and disks allowing for precise track reconstruction in the magnetic field generated by the superconducting magnet. A vertex tracker is located within the beam pipe for optimal functionality. In order to identify particles, a time-of-flight detector, RICH detector, electromagnetic calorimeter, and muon system are included in the setup. Additionally, a conversion tracker is located in a dedicated dipole magnet, improving the experiment's ability to detect particles in the forward direction.

- Tracker has been designed with 11 barrel layers and 2x12 forward discs; it consists of a Vertex Detector, see paragraph 1.3.4.1 (comprising the first 3 layers and 2x3 discs, retractably mounted within a secondary vacuum) and an Outer Tracker, see paragraph 1.3.4.1. The detector has a coverage extending to the pseudorapidity interval of $|\eta| < 4$. The selected technology for the Vertex Detector and Outer Tracker encompasses CMOS Monolithic Active Pixel Sensors.

- The Time-Of-Flight system will be constructed with an inner TOF layer (iTOF) at a radius of 20 cm, an outer TOF layer (oTOF) at a radius of 85 cm and forward TOF discs (fTOF) at a distance of $\pm$ 4.05 m from the interaction point. This will ensure e/π, π/K and K/p separations up to 0.5, 2 and 4 GeV/c respectively. For further details see section 1.3.4.2.

- The Ring Imaging Cherenkov Detector (RICH) placed outside the TOF detector separates e/π from 500 MeV/c to about 2 GeV/c and extends charged hadrons identification up to 10 GeV/c (π/K separation). The RICH detector uses aerogel tile and photo-detection layer made by SiPMs to detect photons. The angle reconstruction algorithm employed is a combination of the Hough Transform method and a time cut of 1 ns. Digital photon avalanche SPADs, such as 2DdSiPM and 3DdSiPM, are under development for improvements. These sensors could be used for both Cherenkov detection and TOF applications.

Component	Observables	|η| < 1.75 (barrel)	1.75 < |η| < 4 (forward)	Detectors
Vertexing	Multi-charm baryons, dielectrons	**Best possible DCA resolution, $\sigma_{DCA} \approx 10$ µm at 200 MeV/c**	**Best possible DCA resolution, $\sigma_{DCA} \approx 30$ µm at 200 MeV/c**	Retractable silicon pixel tracker: $\sigma_{pos} \approx 2.5$ µm, $R_{in} \approx 5$ mm, $X/X_0 \approx 0.1$ % for first layer
Tracking	Multi-charm baryons, dielectrons	**σ_{pT} / p_T ~1-2 %**		Silicon pixel tracker: $\sigma_{pos} \approx 10$ µm, $R_{out} \approx 80$ cm, $X/X_0 \approx 1$ % / layer
Hadron ID	Multi-charm baryons	**π/K/p separation up to a few GeV/c**		Time of flight: $\sigma_{tof} \approx 20$ ps RICH: aerogel, $\sigma_\theta \approx 1.5$ mrad
Electron ID	Dielectrons, quarkonia, $\chi_{c1}(3872)$	pion rejection by 1000x up to ~2 - 3 GeV/c		Time of flight: $\sigma_{tof} \approx 20$ ps RICH: aerogel, $\sigma_\theta \approx 1.5$ mrad possibly preshower detector
Muon ID	Quarkonia, $\chi_{c1}(3872)$	reconstruction of J/Ψ at rest, i.e. muons from 1.5 GeV/c		steel absorber: L ≈ 70 cm muon detectors
Electromagnetic calorimetry	Photons, jets	large acceptance		Pb-Sci calorimeter
	χ_c	high-resolution segment		$PbWO_4$ calorimeter
Ultrasoft photon detection	Ultra-soft photons		measurement of photons in p_T range 1 - 50 MeV/c	Forward Conversion Tracker based on silicon pixel sensors

Figure 1.12: Detector requirements of ALICE 3 detectors

- The Electromagnetic Calorimeter (ECal) covers the central barrel region and a forward region, primarily using a calorimetric sampling approach with alternating layers of lead tungstate ($PbWO_4$) and plastic scintillator. The ECal central barrel design includes a pseudorapidity range of $|\eta| < 1.6$ and extends between the RICH detector and the superconductive magnet. In addition, a disk-shaped endcap is positioned after the forward RICH covering the pseudorapidity interval between $1.6 < \eta < 4$.

- The Muon Identifier is crucial for reconstructing charmonia states in the muon channel, even down to very low transverse momentum ($p_T = 0$), by providing muon tagging for particles reconstructed in the tracker. This functionality complements electron identification capabilities. Positioned outside the magnet system, the Muon Identifier consists of chambers designed to track charged particles passing through the approximately 1 kt hadron absorber which could be iron or non-magnetic steel. The design of the muon system can incorporate resistive plate chambers (RPC), an economical option, or an alternative solution with scintillation rods equipped with wavelength-shifting fibres read by silicon photomultipliers (SiPM).

- The Forward Conversion Tracker (FCT) is a device designed to measure low-energy (up 50 MeV) photons by converting them into electron-positron pairs. The FCT uses a perpendicular magnetic field for precise measurements and features tracking layers with silicon disks. The proposed layout includes 9 silicon disks covering the pseudorapidity $3 < \eta < 5$. The optimal position depends on the final design. The silicon disks in front of the FCT in the ALICE 3 tracker can act as an active converter, eliminating the need for a dedicated converter.

1.3.4.1 The vertexing and tracking detectors

The Vertex Detector (see figure 1.13) in the ALICE 3 experiment is essential for precise determination of the primary vertex position.

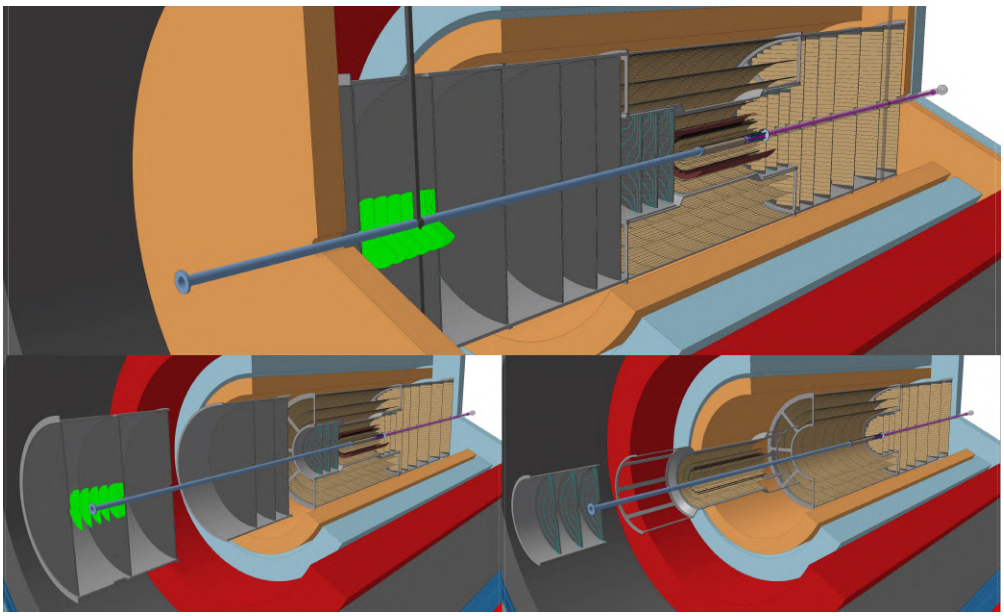

Figure 1.13: Overview of the Vertex Detector and Outer Tracker Assembly.

The silicon vertex detector has been designed to provide a pointing resolution σ_{DCA} better than 10 μm for p_T larger than 200 MeV/c. The required σ_{DCA} can be only achieved by using ultra-thin silicon sensors, featuring an unprecedented low material budget of 0.1% of a radiation length, and with the first tracking layer placed at a radius of 5 mm from the beam axis at top energy. However, a wider aperture of $\approx$ 15 mm is required at injection energy, demanding for a retractable detector design. The current baseline consists of wafer-sized, bent MAPS with 10 μm pixel pitch arranged in 3 barrel layers and 3 forward disks at each end-cap installed in a secondary vacuum inside the beampipe and mounted such that they can be retracted during LHC injection and placed close to the interaction point for data taking. The main R&D challenges concern mechanical supports, cooling and radiation tolerance of the sensors. The vertex detector is complemented by an outer tracker consisting of 8 cylindrical layers and 9 forward disks at each end-cap equipped with MAPS having a pixel pitch of 50 μm, with a material budget thickness of $\approx$1% of a radiation length per layer, and installed in a volume of 80 cm radius and $\pm$4 m length around the interaction point. The leading requirement for the outer tracker is a relative p_T resolution better than 1% over a wide p_T range. The momentum is reconstructed from the curvature in a solenoidal magnetic field of B = 2T provided by a superconducting magnet system featuring an inner radius of 1.5 m.

1.3.4.2 Time of Flight (TOF) System

The tracker is complemented by dedicated Particle Identification (PID) and TOF [52] systems with a pseudorapidity coverage of $|\eta| < 4$.

	Inner TOF	Outer TOF	Forward TOF
Radius (m)	0.19	0.85	0.15–1.5
z range (m)	–0.62–0.62	–2.79–2.79	4.05
Surface (m^2)	1.5	30	14
Granularity (mm^2)	1×1	5×5	1×1 to 5×5
Hit rate (kHz/cm^2)	74	4	122
NIEL (1 MeV n_{eq}/cm^2) / month	$1.3 \cdot 10^{11}$	$6.2 \cdot 10^{9}$	$2.1 \cdot 10^{11}$
TID (rad) / month	$4 \cdot 10^{3}$	$2 \cdot 10^{2}$	$6.6 \cdot 10^{3}$
Material budget ($\%X_0$)	1–3	1–3	1–3
Power density (mW/cm^2)	50	50	50
Time resolution (ps)	20	20	20

Figure 1.14: TOF specifications.

The specifications of the TOF system are given in table 1.14.

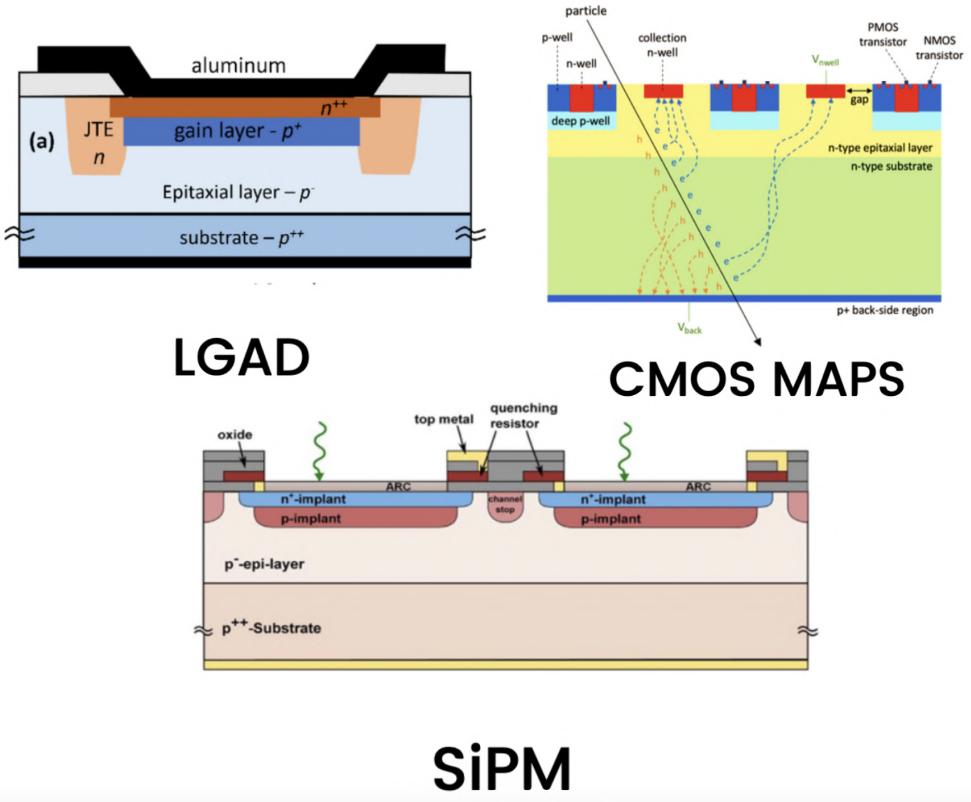

Figure 1.15: figure representing the silicon solutions considered as candidates for the TOF layers of the ALICE 3 experiment.

In order to limit the material budget and cost, the aim is to implement each TOF system with a single layer of sensors, where the front-end electronics combine multiple cells to achieve the desired granularity. A time resolution of 20 ps r.m.s. together with a low material budget of $1-3\%X_0$ and a power density of 50 mW/cm^2 with the required radiation hardness are the main requirements. The required cell size is 1mm x 1mm for

the iTOF and 5mm x 5mm for the oTOF driven by mismatch rate and allowing keeping the the e^{-}/π misidentification at the level of 10^{-3}. The actual cell size will be determined to maximize the sensor time resolution; several cells are the grouped toghether at the front-end electronics level to match the desired granularity for further processing.

The TOF system can be broken down into a few key building blocks: the sensor, the front-end, the time-to-digital converter (TDC), the clock management system and the readout system. The design of a TDC and clock management for a large system is still challenging, but the last decade has seen impressive improvements in this respect. TDCs with bin sizes in the ps range, resulting in RMS quantization noise of the order of a few ps, sampling rates of tens of MHz and power consumption below 10 mW per channel could be useful. The readout is based on an asynchronous communication scheme between the pixels and the peripherals to avoid high power dissipation. The architecture will be modular and assembled using a digital-on-top design flow. The data payload generated by the matrix is collected at the chip periphery, serialised and sent off-chip via high-speed serial links. Time-over-threshold will be used as a proxy for the signal amplitude in the time-walk correction. The calibration strategy will be modelled on the scheme adopted for the current ALICE TOF detector.

Three sensor technologies have been investigated and are currently under development for the TOF: fully depleted complementary metal-oxide-semiconductor (CMOS) sensors figure 1.15 on right [53], low-gain avalanche diodes (LGAD) figure 1.15 on left [54]-[55], and single-photon avalanche diodes (SPAD) 1.15 [56]-[57] in the middle.

1.3.4.3 Magnet system and infrastructure

The installation process of the ALICE 3 detector involves the removal of the current ALICE detector and dipole magnet, leaving only the L3 magnet yoke within the cavern. The installation will integrate a superconducting magnet within the volume of the L3 magnet, utilizing the yoke as a magnetic field shield towards the cavern.

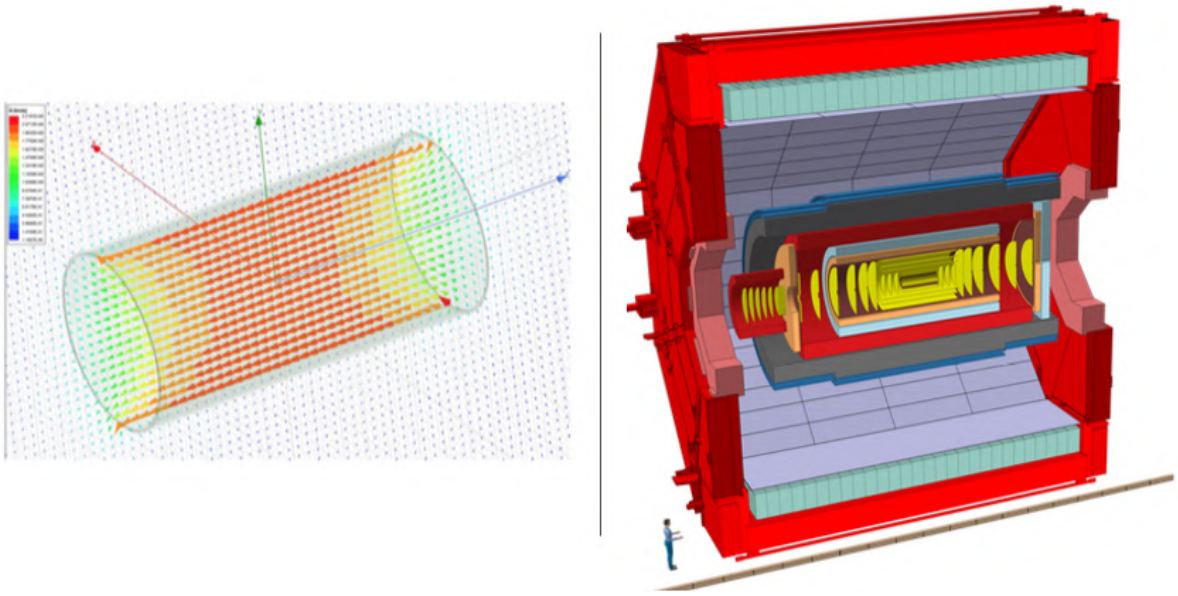

Figure 1.16: Solenoidal superconducting magnet system (left). Detector layout with a solenoid and a dedicated dipole magnet for the FCT (right)

This setup allows symmetric detector installation and assembly with a central barrel and two end caps, as depicted in figure 1.16 (right). The absorber material for the

muon system is primarily non-magnetic steel, with magnetic steel as a potential alternative. The superconducting magnet system for the ALICE 3 experiment considers the configuration shown in figure 1.16 (left): a solenoid coil of 2 T extending the full length of 7.5 m, with additional windings at the ends to achieve a 50% higher current density. The momentum resolution for muons with p_T = 1 GeV/c varies from 0.6% to 1% up to η = 2, deteriorating to about 5% at η = 4.

Chapter 2

Low Gain Avalanche Diode (LGAD)

Semiconductor materials[58], such as silicon, are the foundation of particle detectors, relying on high-purity crystals with precise lattice structures. The smallest repeating unit of atoms that forms the entire crystal is known as the primitive cell, with its dimensions determined by the lattice constant, which defines the crystal's periodicity. Although the electrons in individual atoms have different energy levels, when arranged in a lattice structure they can interact with each other, splitting their energy levels into states that differ only slightly from each other. It is important to note that this interaction is a result of the lattice structure, not of the individual atoms themselves. At room temperature, thermal energy can break covalent bonds in silicon, releasing electrons and creating holes [59].

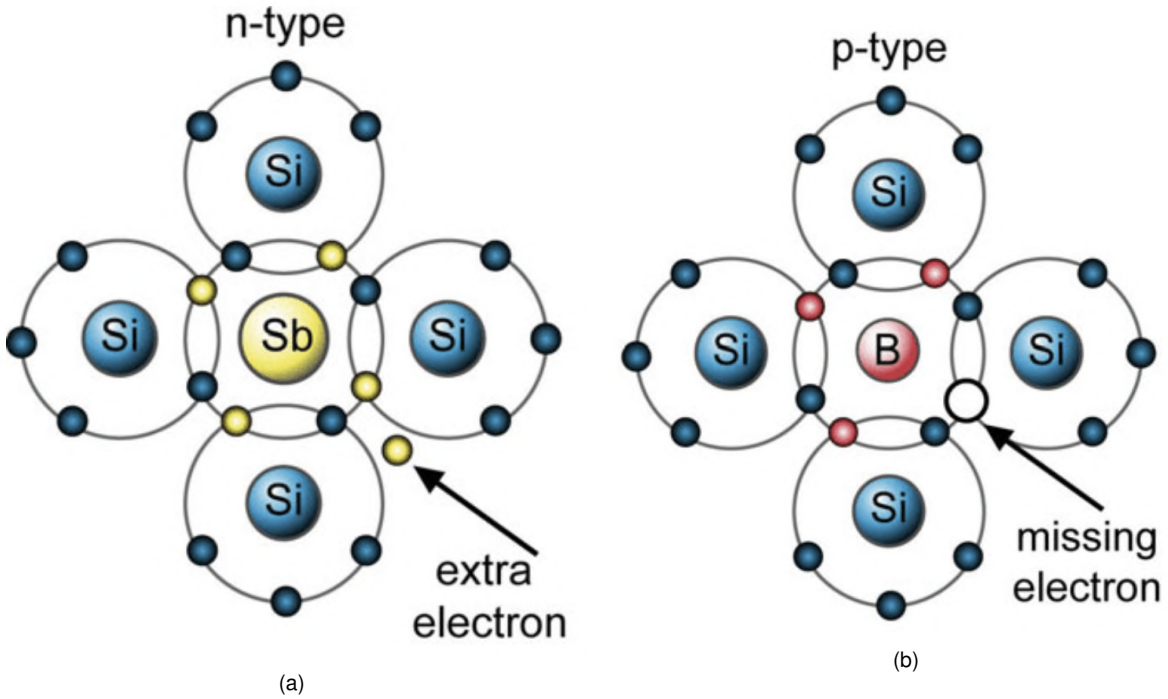

Figure 2.1: Effect of N-type doping (a) and P-type doping (b).

However, to detect crossing charged particles, it is necessary to distinguish clearly between the charge deposited in the silicon by ionization and the amount of free carriers originating from thermal effects (noise). In order to reduce the noise, controlled impurities, known as dopants, are artificially introduced into the intrinsic silicon lattice, creating additional levels within the band gap and altering the electrical properties of the material. This process is known as doping. The silicon semiconductor, which is typ-

ically not pure and contains impurity atoms occupying some silicon positions, is called extrinsic. Replacing a silicon atom with an atom of a group V (III) element, increase the concentration of free electrons (holes). This type of extrinsic silicon is known as N-type (P-type) doping, see figures 2.1a (2.1b). In the case of doped semiconductors, the density of free carriers is often too high to make silicon suitable as a particle detector.

However, by connecting semiconductors with opposite doping, a region without free charges can be created and exploited. The pn junction is the basis for semiconductors devices, which are important part of the technological evolution of recent years, leading to modern devices for research use. The boundary between these regions is known as the metallurgical junction. In a simplified step junction, there is a uniform doping concentration within each region, resulting in a change at the junction. Initially, there's a significant density gradient in electron and hole concentrations [60]-[61] at the junction. Electrons diffuse from the n region to the p region, where they undergo a recombination process with holes which are the majority charge carriers in this region, leaving behind positively charged donor atoms. Simultaneously, holes diffuse from the p region to the n region, uncovering negatively charged acceptor atoms. The diffusion process cannot continue indefinitely without external connections to the semiconductor. The resulting net positive and negative charges create an electric field across the junction, leading to the formation of a space charge or depletion region where mobile charges are swept out.

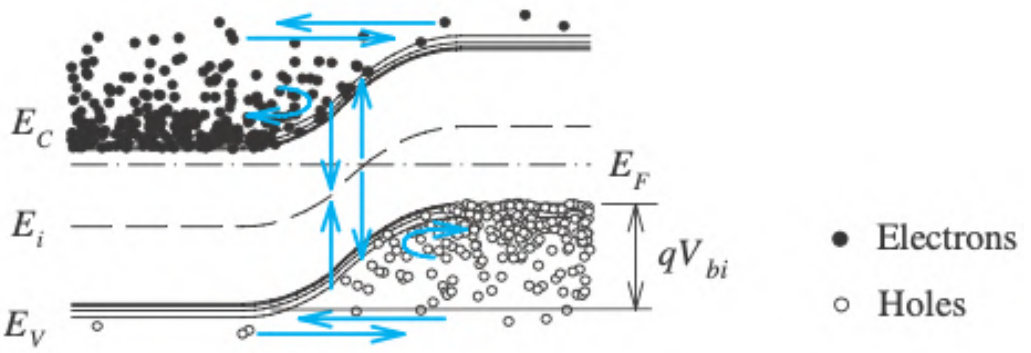

Figure 2.2: This image illustrates the band bending in the depletion region of a semiconductor. It is important to note that the Fermi level (E_F) remains constant. The built-in potential represents the energy barrier that electrons/holes must overcome to move to the other side and is depicted as a type of wall.

At the edges of the space charge region, there are still density gradients that cause diffusion forces to act on majority carriers. However, these forces are counteracted by the electric field in the space charge region during thermal equilibrium. The built-in electric field results in a built-in voltage across the depletion layer, represented as the energy barrier qV_{bi}, where V_{bi} is the built-in potential, in figure 2.2. The equation 2.0.1 provides the built-in voltage at a pn junction, where V_T is the thermal voltage, n_i is referred to be intrinsic charge carrier concentration, $N_{A/D}$ is the concentration of acceptor and donor [62]:

$$V_{bi} = V_T ln(\frac{N_D N_A}{n_i^2}) \tag{2.0.1}$$

The balance between the diffusion and drift currents of electrons and holes is disturbed when an external voltage is applied to a pn junction. The forward bias allows more electrons to diffuse from the n to the p side and holes to diffuse in the opposite direction [63], reducing the electrostatic potential across the depletion region (see figure

2.3a). This results in minority carrier injections, with electrons injected into the p-side and holes into the n-side.

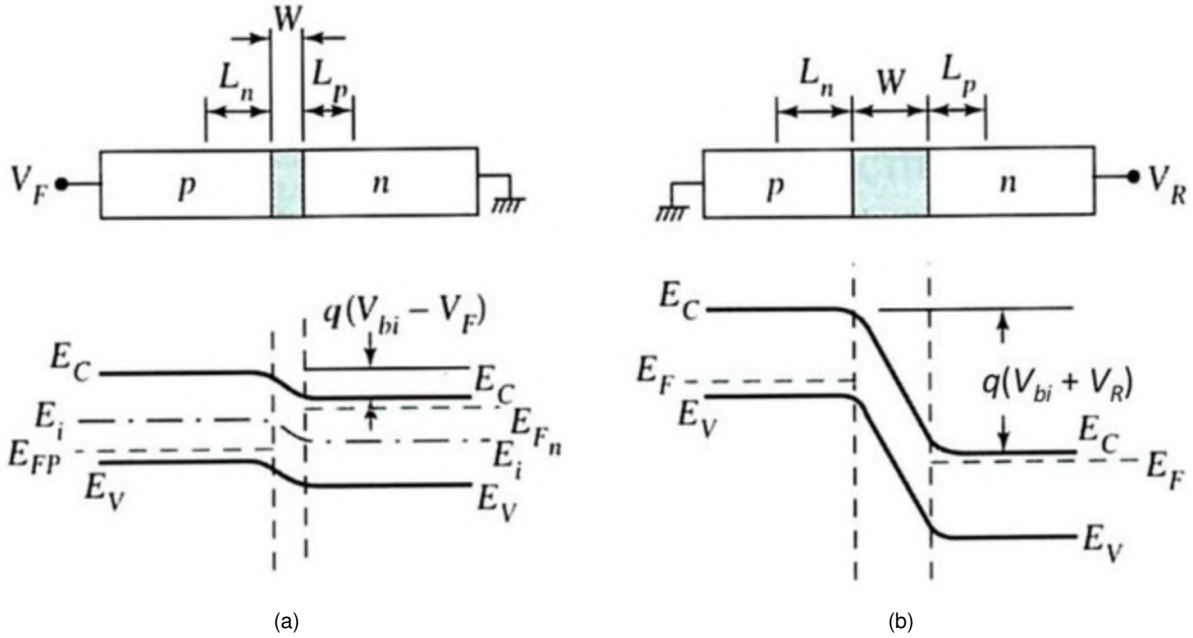

Figure 2.3: This diagram illustrates the depletion region and energy band diagram under forward (a) and reverse bias (b).

Conversely, under reverse bias (see figure 2.3b), the applied voltage increases the electrostatic potential across the depletion region, significantly reducing diffusion currents. The drift current remains almost the same due to the low concentration of minority carriers. The coexistence of drift and diffusion currents in the depletion region complicates the derivation of current equations, leading to a focus on diffusion equations outside this region.

2.1 Operating Principles of silicon detector

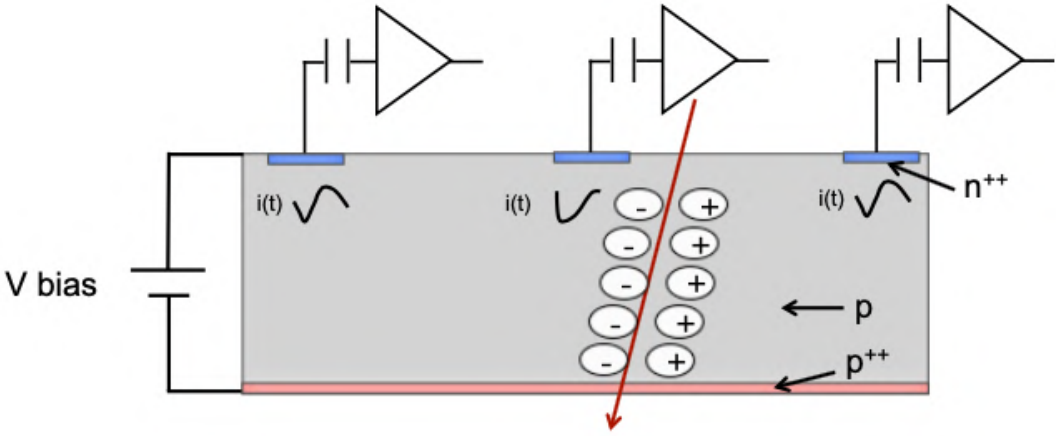

Figure 2.4: An external bias voltage is used to reverse-polarise the pn junction, creating a large depleted volume. Incoming charged particles create electron-hole pairs and whose drift motion induces a current in the electronics. The Bethe-Bloch formula describes the average energy loss of a charged particle in a medium based on its energy.

The basic operating principles of an n-on-p silicon detector are shown in figure 2.4 [67]. When a charged particle passes through the sensor (which is inversely polarized), it creates electron-hole pairs (e-h) along its path. The number of pairs generated depends on the particle type, energy, and sensor thickness. An induced current is generated on the electrodes as the electrons drift towards the n^{++} contact and the holes towards the p^{++} contact under the influence of the electric field. In applications, the amplifier integrates the current over time, producing a signal with an amplitude proportional to the integral of the induced current. This is approximately 1 fC for every 100 microns of sensor thickness. Accurate measurement of a particle's hit time requires a high signal with a short rise time, it was shown [65] that this can be achieved by very-thin sensor with internal gain.

2.2 Design and structure of LGAD

The design and construction of particle physics experiments could be revolutionised by the integration of time data. This is because the process of event reconstruction can be greatly enhanced by the inclusion of time information. In particular, time data can help event reconstruction by excluding tracks that cannot be associated with an event due to significant time differences, distinguishing between overlapping events, improving the precision of reconstructed kinetic parameters, protecting the trigger bandwidth from being overwhelmed by spurious events, and distinguishing between events with the same topology but originating from one or more collisions. Implementing particle detectors which can provide simultaneously an excellent timing and space resolution can bring to substantial advancements in research. Silicon detectors have unique properties that make them extremely suitable for in a wide range of research areas. They are thin, lightweight, and can offer a position resolution better than 10 microns across large areas.

An Ultra-Fast Silicon Detector (UFSD) [64] is a silicon sensor with an very good space resolution optimized to provide also an excellent time resolution. This improvement gives the possibility to use the time information for a 4-D tracking [65] in particle physics experiments. Ultra-fast silicon diodes are based on Low-Gain Avalanche Diodes (LGADs) [68] that make use of the phenomenon of charge multiplication. Unlike devices such as Avalanche Photon Detectors (APD) and Silicon Photon Multipliers (SiPM), which have gains in the range of hundreds to thousands, LGAD operates with a moderate gain of 10-20.

The design of LGAD involves the modification of the doping profile by the introduction of an additional doping layer of p+ material (boron or gallium) near the N-P junction, see figure 2.5. At the edge of the pixel (or pad), an additional virtual Guard Ring (VGR) and a Junction Termination Extension (JTE) are implemented to prevent premature breakdown at the pad's border and ensure uniformity of the electric field. The Guard Ring comprises a gap between the end of the gain layer and the n^{++} edges, while JTE is a deep low-concentration n-type region at the junction edge. These termination structures utilise a portion of the sensor area and consequently introduce an inter-pad region where the gain is completely suppressed. This region is known as the no-gain region, which is defined as the distance between two adjacent gain regions. Neighboring pads can be electrically isolated by a narrow p^{+} ring, called p-stop, which separates the n^{++} electrodes and stops the diffusion of electrons through adjacent pads. At the top, there are usually layers of silicon nitride and silicon dioxide present as an antireflective and insulating coating.

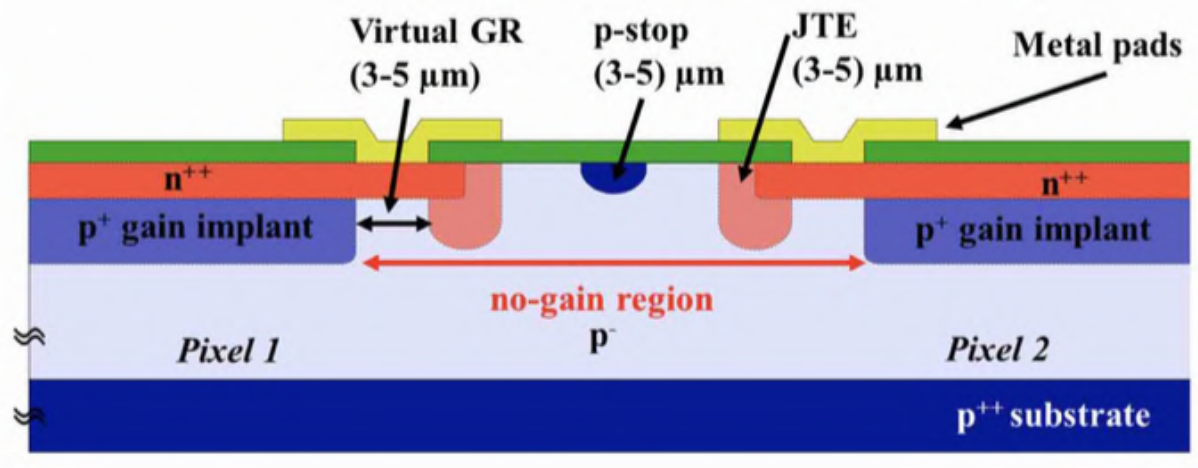

Figure 2.5: LGAD design, with an additional p^{+}-layer right below the n^{++}- junction.

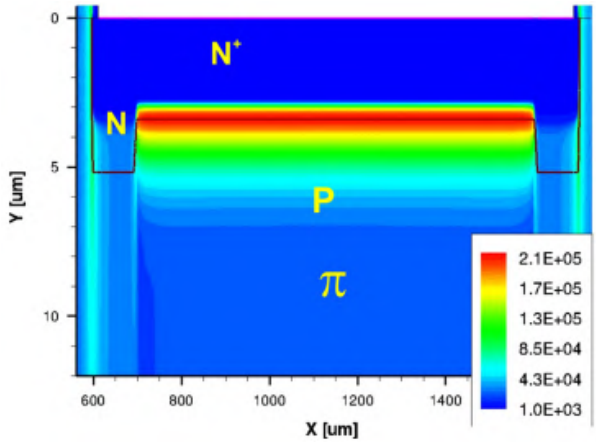

Figure 2.6: Simulated electric field distribution in the multiplication junction of an LGAD with a Junction Termination Extension.

The resulting doping profile creates a large electric field near the junction (see figure 2.6) due to a significant increase in doping concentration. Figure 2.7 illustrates the electric field in a 300 μmm thick LGAD at different bias voltages and that of a p-in-n (PIN) diode at V = 600 V, with distinct zones: a drift volume with low electric field values (E $\simeq$ 30 kV/cm) and a thin multiplication zone with very high field values (E $\simeq$ 300kV/cm).

In LGAD design, it is necessary to carefully shape the implants to enable high bias-voltage operation without breakdown. The multiplication process in the n-in-p LGAD configuration is initiated by electrons drifting towards the n^{++} electrode. Compared to the p-in-n design, where holes initiate the multiplication process by drifting towards the p^{++} electrode, this design provides better control over the multiplication process.

The n-in-p design enables tuning of the electric field to ensure that only electrons drive the multiplication process. This results in reliable operation, as the gain becomes less sensitive to the exact electric field value. Furthermore, this tuning minimises noise from the multiplication process, known as the excess noise factor A.3, thereby improving LGAD performance.

Charged particles produce in mean 73 electron-hole pairs in one micron of silicon. This allows to have signals high enough also mantaining a low gain, thus avoiding problems related to power consumption, and having a low noise in the sensor. LGADs with a gain of approximately 20 are considered optimum for low-noise, low-power operation.

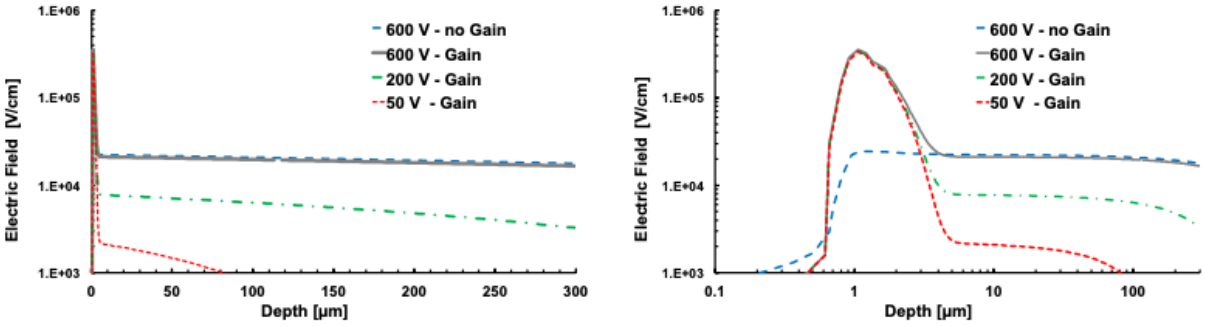

Figure 2.7: The electric field of a 300 μm thick LGAD at different bias voltages compared to a PIN (no gain) silicon sensor in linear (left) and logarithmic (right) scale.

The current value of di_G generated by a gain G within the multiplication layer can be estimated using Shockley-Ramo's theorem:

$$di_G \simeq \frac{G}{d} dt \tag{2.2.1}$$

The ratio between the gain value and the sensor thickness is proportional to the increase in the signal current derivative due to the gain mechanism. The thickness of the detector is the other important variable. This has an effect on the rise time (slew rate), which is determined by the drift time of electrons. Thin sensors have a much faster rising edge, improving time resolution by minimizing jitter and time walk. However, the detector cannot be too thin, othewise, large capacitance values are required to generate signals that are accurate enough to be measured by the read-out electronics. Both of these factors negatively impact time resolution.

2.2.1 Charge multiplication process

Charge multiplication in silicon sensors occurs when the charge carriers are in electric fields of the order of E $\simeq$ 300 kV/cm. Under this condition, the electrons acquire sufficient kinetic energy to generate additional e/h pairs. A field value of 300 kV/cm in the whole sensor thickness cannot be achieved by just applying an external voltage V_{Bias} but it can be achieved by implanting an appropriate charge density that locally generates very high fields ($N_D \simeq 10^{16} cm^{-3}$). The amplification has an exponential dependence on the electric field : $N(l) = N_0 e^{\alpha(E)l}$ where α is a function of the electric field and l is the path length inside the high field region.

2.2.2 Time resolution

Accurate time measurements [69]-[71] depend on both the time resolution of the sensor and the read-out electronics' ability to determine the particle's passage time using signals from the sensor. Figure 2.8 illustrates the key components of a time-tagging detector: the sensor signal is processed by a preamplifier, compared to a threshold V_{th}, and then digitised by a Time-to-Digital Converter (TDC), which measures the time between particle trigger and crossing threshold V_{th}. In this model, the particle arrival time t_0 is defined as the instant when the signal exceeds the threshold. Factors influencing time resolution are grouped into four categories in equation 2.2.2:

$$\sigma_t^2 = \sigma_{TimeWalk}^2 + \sigma_{LandauNoise}^2 + \sigma_{Distortion}^2 + \sigma_{Jitter}^2 + \sigma_{TDC}^2 \tag{2.2.2}$$

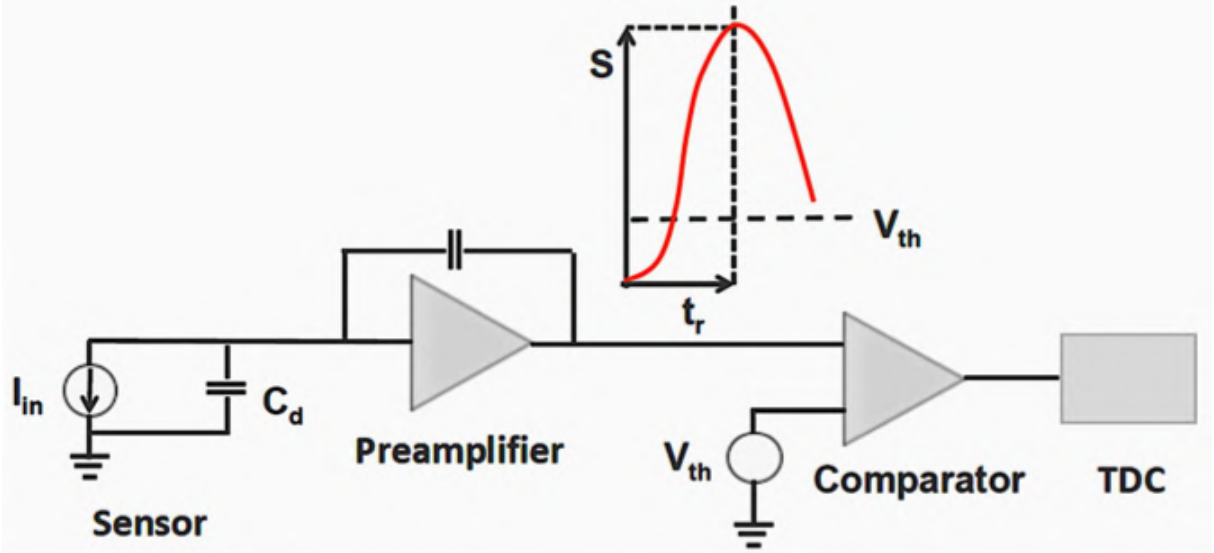

Figure 2.8: Main components of a time-tagging detector: sensor, preamplifier [65], comparator and TDC. The time is measured when the signal crosses the threshold.

We broadly group the effects influencing the time resolution of equation 2.2.2 into 4 contributions:

- Energy deposition by the particle, affecting amplitude variations ($\sigma^2_{TimeWalk}$) (appendix A.2) and signal irregularities ($\sigma^2_{LandauNoise}$).
- Signal distortion caused by non-uniform weighting fields and varying charge carrier drift velocity ($\sigma^2_{Distortion}$).
- Electronics-related factors, primarily noise and amplifier slew rate (σ^2_{Jitter}).
- Digitization effects driven by TDC uncertainties (σ^2_{TDC}).

2.2.2.1 Landau Fluctuation

The physics governing the energy deposition by an incident charged particle in silicon sets the ultimate limit to signal uniformity, due to the fact that the total number and local density of electron-hole pairs created along the path of the particle varies from event to event. This effect is the same for LGAD sensors and for PIN. These variations cause irregularities in the current signal, known as Landau noise, as well as an overall change in signal amplitude, which is the cause of the time walk effect.

Figure 2.9 shows two examples of the simulated energy deposition of a MIP in a 200 μm-thick sensor with no gain, together with the corresponding current signals generated and their components. The variations shown in the picture are significant and can greatly reduce the achievable time resolution.

2.2.2.2 Time-Walk

The term 'Time Walk' refers to the phenomenon where larger signals cross a given threshold earlier than smaller ones. Let's consider a simple scenario with a linear signal having an amplitude S and a rise time t_r. The signal crosses the threshold V_{th} with a delay t_d. Using the relationship $t_d/t_{rise} = V_{th}/S$, we can express the moment

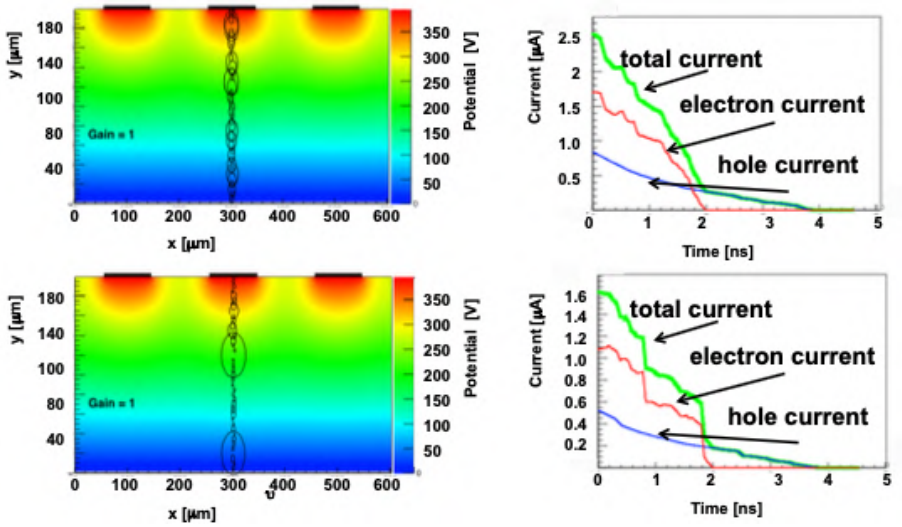

Figure 2.9: Simulation of the energy deposition by an impinging MIP in a silicon detector and the corresponding current signals.

when the particle crosses the threshold as $t_d = \frac{t_{rise} V_{th}}{S}$. The Time Walk, defined as the root mean square (rms) of t_d, is given by:

$$\sigma_{TimeWalk} = [\frac{N}{dV/dt}]_{RMS} \tag{2.2.3}$$

In equation 2.2.3, N represents the system noise, and minimizing Time Walk involves having systems with low noise and high slew rate.

2.2.2.3 Signal Distortion

In every particle detector, the induced current signal's shape can be calculated using the Ramo-Shockley's theorem, expressed in equation 2.2.4:

$$i(t) = -q\vec{v}\vec{E_w} \tag{2.2.4}$$

This equation contains the main parameters to consider in the designing sensors for accurate timing:

- Uniform drift velocity: maintaining a constant drift velocity throughout the sensor volume is crucial. This can be achieved by ensuring a sufficiently high electric field everywhere in the sensor's active volume so that carriers always move with saturated drift velocity (need for a field of about 30 kV/cm). Cooling the sensor has two effects: it lowers the field needed for saturated velocity and increases the saturated velocity. Variations in signal shape based on hit position compromise overall time resolution due to non-uniform drift velocity (refer to figure 2.10).
- Weighting Field: represents the capacitive coupling of a charge to the read-out electrode, should remain constant along the electrode pitch. If the coupling is dependent on the position of the particle along the implant pitch, the shape of the signal would vary, with an effect on the time resolution. Two cases are shown in figure 2.10: wide strip geometry, where the strip width is similar to the strip pitch, results in a relatively constant weighting field along the pitch. In contrast, the weighting field is concentrated only below the strip implant for narrow strips with a width much smaller than the pitch.

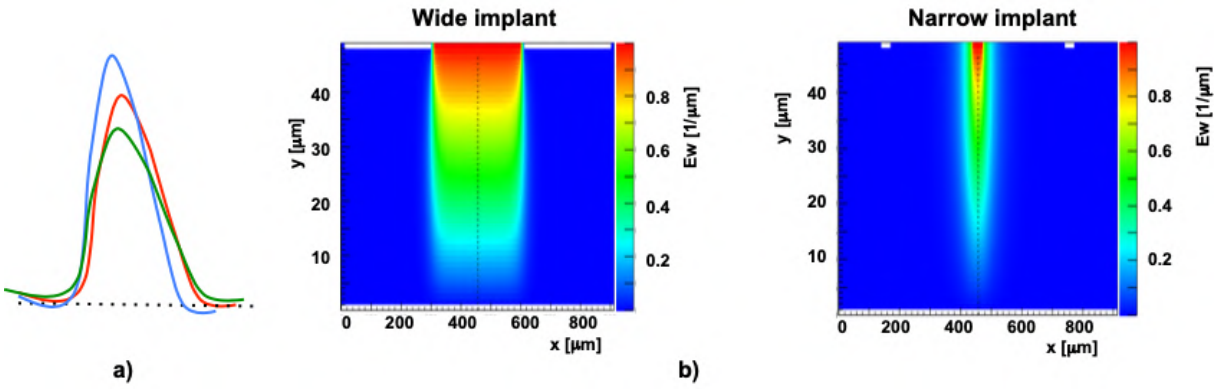

Figure 2.10: (a) Effect of velocity variation on the signal shape (b) Weighting field for two configurations: (left) wide implants, (right) narrow implants.

In summary, achieving good time resolution requires a sensor geometry close to a parallel plate capacitor, with uniform electric and weighting fields. This entails implants having a width similar to the pitch, and the pitch being larger than the sensor thickness.

In addition, in systems where the weighting field varies across the volume of the sensor, there is an additional source of time uncertainty: before the particle signal becomes visible, the charge carriers must drift from the point of impact to the region of high weighting field. This effect is illustrated in figure 2.11.

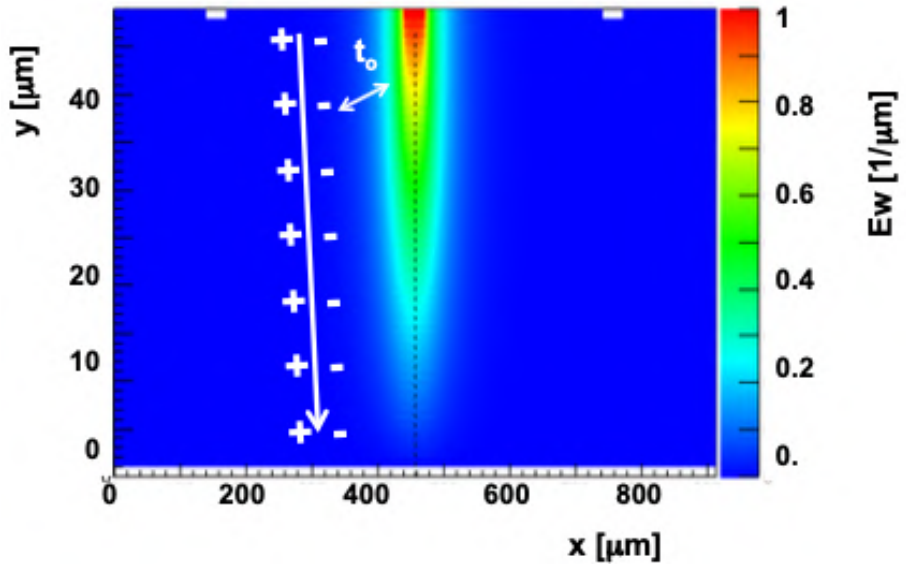

Figure 2.11: Non-uniform weighting field causes an additional source of time uncertainties due to the drift time from the impact point to the region of high weighting field.

In silicon, electrons with a saturated velocity can move approximately 1 μm in 10 ps [65]. Therefore, this effect can easily become the dominant source of time uncertainties.

2.2.2.4 Jitter

This term represents time uncertainty resulting from comparator firing earlier or later because electrical noise. It is directly proportional to the system noise N and inversely proportional to the slope of the signal around the comparator threshold, see equation:

$$\sigma_{jitter} = \frac{t_{rise}}{S/N} \tag{2.2.5}$$

This equation represents the core of electronic design optimization, which involves competing effects. Wide bandwidth is required for large slew rates, but this also increases noise. Conversely, low noise requires smaller slew rates.

2.2.2.5 TDC

A time-to-digital converter (TDC) is commonly used to record timing information for readout. This involves digitising the time of the leading edge of the discriminator signal and placing it in a time bin of width ΔT, which is determined by the TDC's least significant bit.The contribution of this process to the timing uncertainty is $\Delta T/\sqrt{12}$. It is crucial to minimize the error introduced by the TDC to ensure it has a minimal impact on the overall resolution, regardless of the sensor characteristics. Although there are alternative methods available to mitigate TDC effects, such as template methods, pulse shape fitting, or digitizing the entire pulse shape in a sampling digitizer, these may not be practical in systems with a large number of channels [65].

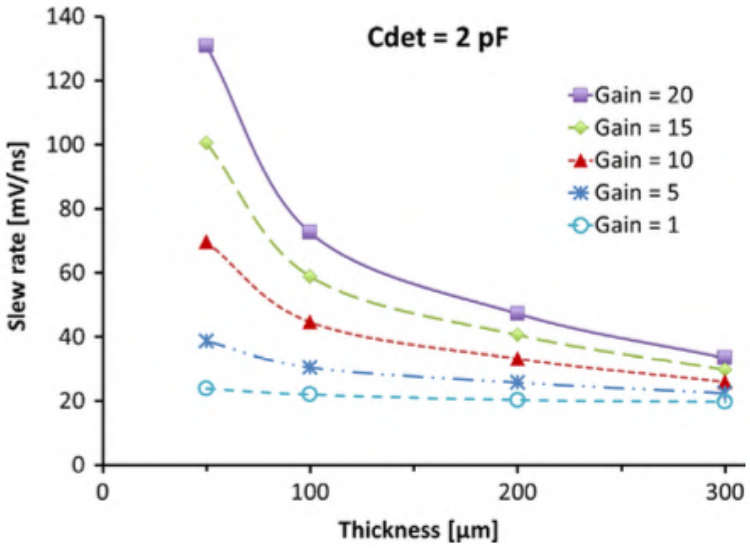

Figure 2.12: Simulations of the slew-rate dV/dt as measured by a 50 Ω Broadband amplifier as a function of sensor thickness and various gain values. They indicate the good time resolution achievable with thin LGAD with gain. At 50 μm thickness, a gain of 10 results in a three times improvement in the time resolution when compared to a no-gain sensor.

In the light of the above, the time resolution can be re-written in the following way:

$$\sigma_t^2 = [\frac{V_{th}}{dV/dt}]^2_{RMS} + [\frac{N}{dV/dt}]^2 + [\frac{TDC_{bin}}{\sqrt{12}}]^2 + \sigma^2_{LandauNoise} + \sigma^2_{Distortion} \tag{2.2.6}$$

where TDC_{bin} is the size of a TDC bin, while dV/dt is the slew rate of the signal. This means that in order to obtain an improved time resolution both large and fast signals are needed. Using WF2 [72], it can be shown that time resolution improves with both higher gain and thin detectors (figure 2.12), since both increase the slew rate. An additional advantage is expected from sensors with reduced capacitance. These allow a higher slew rate for a fixed input impedance of the amplifier.

2.2.3 Optimization of LGAD sensor

A simulation is reported in figure 2.13 showing the current, and its components, for a 50 μm-thick detector [73]. The initial electrons (red), drifting toward the n electrode, go through the gain layer and generate additional e/h pairs. The gain electrons (violet) are readily absorbed by the cathode while the gain holes (light blue) drift toward the anode and they generate a large current.

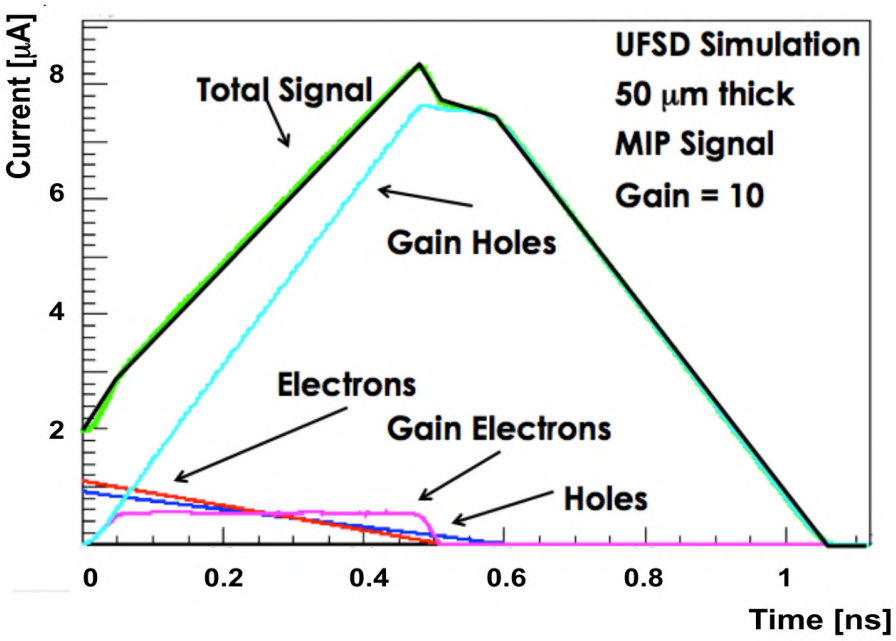

Figure 2.13: LGAD simulated current signal for a 50 μm-thick detector.

The gain dramatically increases the signal amplitude, producing a much higher slew rate. The value of the current generated by a gain G can be estimated using equation 2.2.1 which leads to the following expression for the slew rate:

$$\frac{di_G}{dt} \propto \frac{dV}{dt} = \frac{G}{d} \tag{2.2.7}$$

The increase in slew rate due to the gain mechanism is proportional to the ratio of the gain value to the sensor thickness, therefore thin detectors with high gain provide the best time resolution. Specifically, the maximum signal amplitude is controlled only by the gain value, while the signal rise time only by the sensor thickness, figure 2.14.

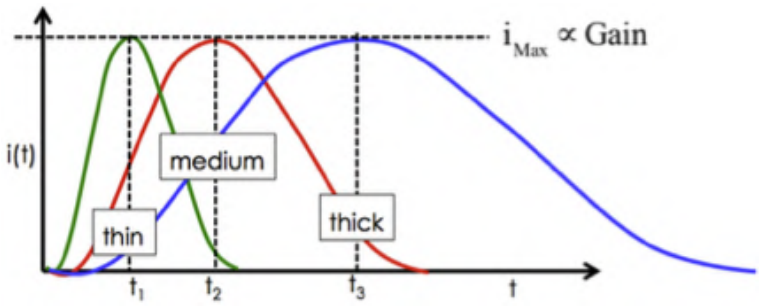

Figure 2.14: In LGAD, the maximum signal amplitude depends only on the gain value, while the signal rise time depends only on the sensor thickness: sensors of 3 different thicknesses (thin, medium, thick) with the same gain will have signals with the same amplitude but with different rise time.

2.2.3.1 Gain layer position

Good timing requires very uniform field and gain, which may conflict with the goal of a fine electrode segmentation. The relative position of the gain layer and the segmented readout electrodes depends on the silicon bulk and strip type, as shown in figure 2.15.

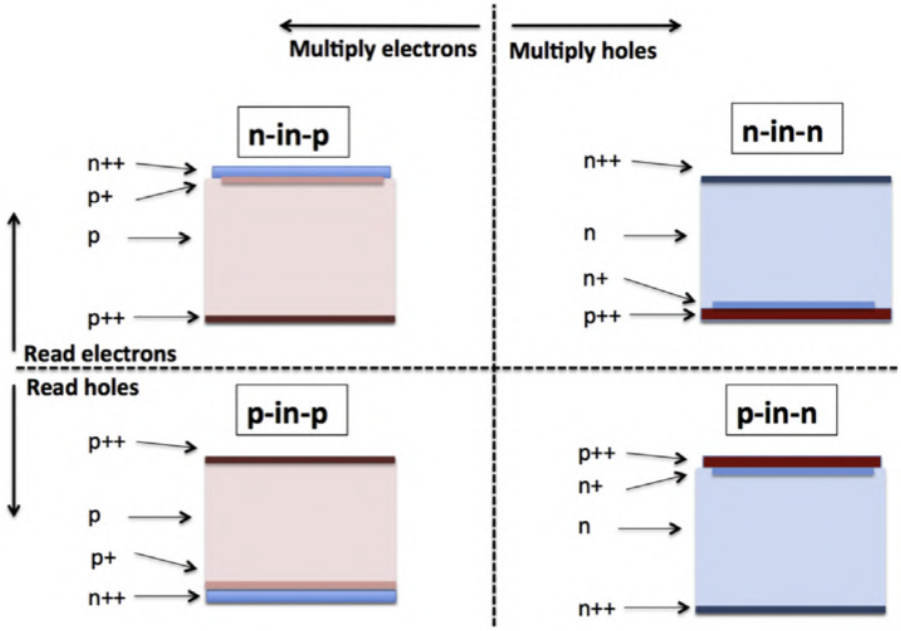

Figure 2.15: 4 possible configurations of the gain layer. In n-bulk sensors the multiplication is initiated by holes, while in p-bulk sensors by electrons.

For n-in-p detectors, the gain layer is below the read-out electrodes, whereas for p-in-p it's on the opposite side. Similarly, for p-in-n sensors the gain layer is on the electrodes and for n-in-n sensors it's on the opposite side. The use of n-bulk sensors poses challenges due to the multiplication mechanism being initiated by drifting holes, making it difficult to control and prone to evolving into Geiger mode. Therefore, this option is not further pursued.

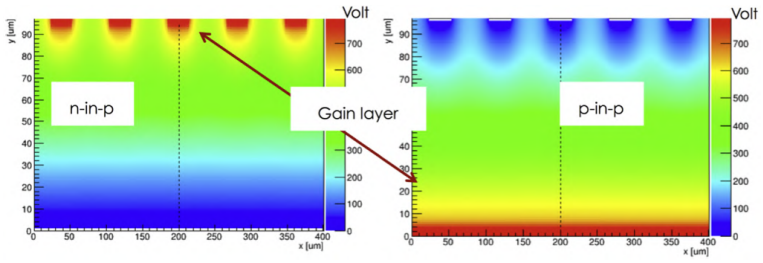

Figure 2.16: Potential field of two possible configurations of the LGAD. Left: n-in-p configuration with the gain layer under the segmented electrodes. Right: p-in-p configuration with the gain layer in the deep side. The secondary y-axis shows the value of the potential.

Figure 2.16 shows the potential fields for n-in-p and p-in-p geometries in highly segmented readouts. When deciding between n-in-p and p-in-p designs, the effect of the weighting field on the signal shape is crucial. In segmented detectors, the weighting field ensures that only charges close to the readout electrode contribute significantly to the signal. The choice between n-in-p and p-in-p sensors depends on the application: n-in-p sensors are suitable for large electrodes, while thin p-in-p sensors are preferable for applications requiring highly segmented read-out electrodes.

2.2.3.2 Effect of Landau fluctuations

The ultimate challenge in achieving signal uniformity comes from the inherent physics of energy deposition in silicon. When an ionising particle passes through the sensor (see figure 2.17), the resulting charge distribution varies from event to event. This variation not only leads to an overall change in signal magnitude, causing the time walk effect, but also introduces irregularities in the current signal. These variations are substantial and can significantly affect the achievable time resolution.

There are two strategies to mitigate this effect:

- Integrating the output current: this involves integrating the output current over durations longer than the typical spike length, smoothing out variations in the signal.
- Using thin sensors: thin sensors are recommended because their steeper signal response is more resilient to fluctuations, offering improved immunity to the challenges posed by varying charge distributions.

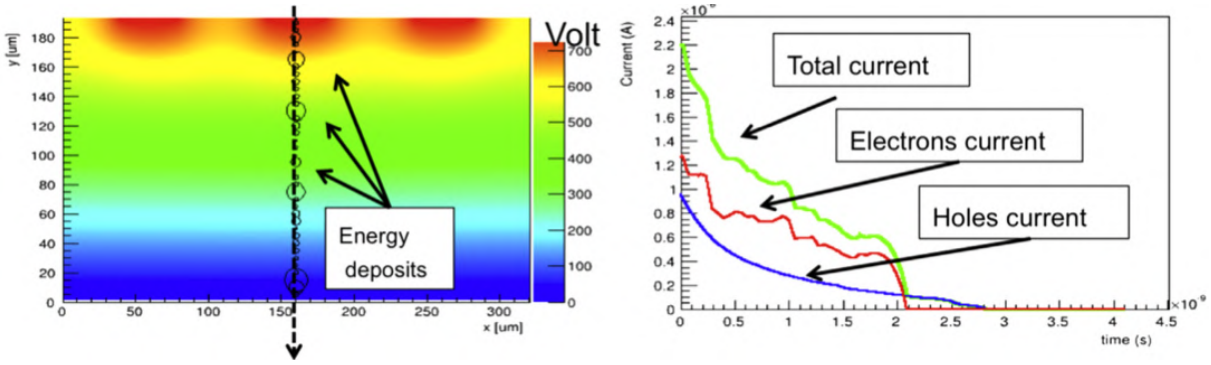

Figure 2.17: Left: Simulation of the energy deposition from a minimum ionising particle in a standard n-in-p sensor: the non-uniform charge clusters produce irregular signals. Right: The current signal associated with the clusters shown on the left.

Chapter 3

Experimental study and characterization of LGAD sensors

In this chapter, I will discuss the results obtained during my thesis work carried out within the ALICE TOF group in Bologna, at the INFN laboratories located at Viale C. Berti Pichat 6/6-2 and Via Irnerio 46, in the Department of Physics and Astronomy of the University of Bologna, as well as at CERN, specifically at the Proton Synchrotron (PS) in the T10 area in Meyrin.

3.1 Introduction to state-of-art

Part of my thesis activity involves the time characterization of LGAD sensors using charged particles and photons, with the goal of obtaining a general perspective on the performance of these sensors.

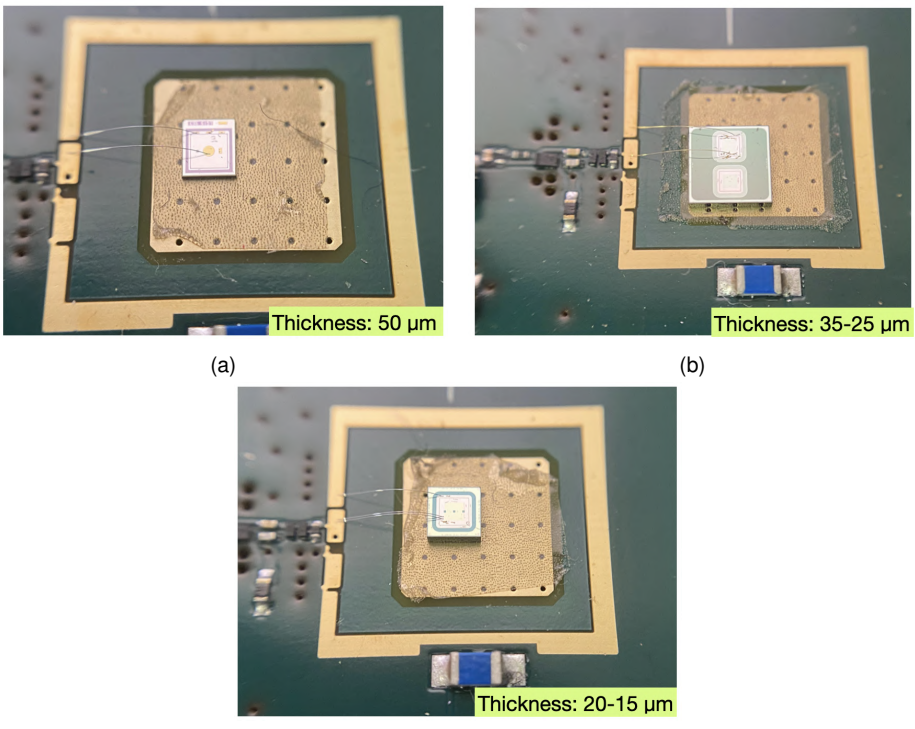

Figure 3.1: Zooms of the LGAD sensors that were studied in Bologna, specifically: (a) 50μm sensor, (b) typical design of a 35 or 25 μm sensor, typical design (c) of a 20 or 15 μm sensor.

This characterization, in accordance with the ALICE 3 Letter of Intent (LOI) [31], is part of the research and development plan to identify a technology capable of providing the 20 ps time resolution required (see table in figure 1.14), thereby demonstrating that this technology is the ideal choice for the TOF layers of the future ALICE 3 experiment. The second part of my thesis focuses on the energy characterization of these sensors, conducted both with charged particles in beam tests and with photons using an ^{55}Fe source [74]-[75].

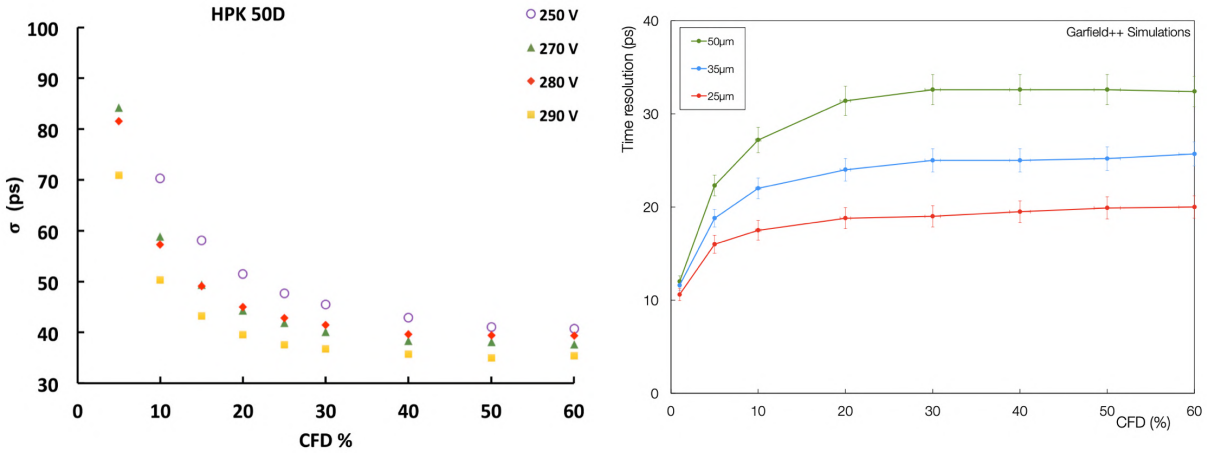

(a) (b)

Figure 3.2: (a) Test beam measurements of the time resolution of 50 μm-thick LGADs as a function of Constant Fraction Discriminator (CFD) for different voltages. (b) Garfield++ simulations of the LGAD time resolution as a function of CFD for different sensor thicknesses. Taken from LOI of ALICE 3 [31].

The idea behind this measurement is to provide insight into an aspect of these sensors that has not yet been characterized and whose impact on TOF performance still needs to be evaluated. As can be inferred from the structure of an LGAD, this sensor is ideal for timing purposes but not for other applications, given the significant amount of inactive area present and the presence of a gain layer which make the distinction among energetic peaks of ^{55}Fe source difficult.

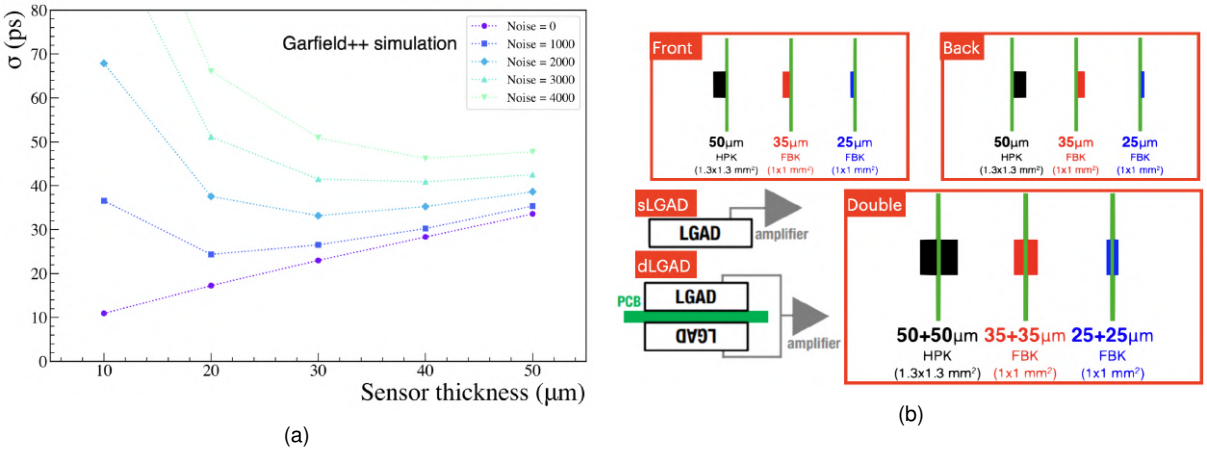

(a) (b)

Figure 3.3: (a) Simulation of LGAD time resolution as a function of thickness using Garfield++. (b) Implementation of a dLGAD module with sensors of varying thicknesses, illustrating the combined output signal from both sensors.

In Bologna, the study began with the first ultra-thin LGAD sensors, with thicknesses less than 50 μm (35-25-20-15 μm) shown in figures 3.1a-3.1c, produced by the Fondazione Bruno Kessler (FBK) [76]. According to simulations, these sensors were ex-

pected to provide better time resolution, see figure 3.2a-3.2b. This expectation is connected to the fact that the resolution is directly dependent on the electron drift time in the sensor, meaning that the thinner the sensor, the shorter the drift time, and the better the time resolution, see figure 3.3a. However, when theory was put into practice, the signal turned out to be too small, requiring highly power-consuming electronics to obtain a sufficiently large signal for analysis. Clearly, this approach is not viable for ALICE 3, which is why the ALICE TOF group in Bologna developed the innovative concept of the double-LGAD (dLGAD) [77], figure 3.3b, i.e., the implantation of two sensors on either side of a specifically designed Printed Circuit Board (PCB), so that the two signals are summed up and sent to a single common amplifier. The main advantages lie in the significant reduction in power consumption due to the use of a single amplifier, as well as the improvement in time resolution and the increase in charge at the input of the amplifier. The main drawback, however, is the increased material budget.

3.1.1 Single and double LGAD: a brief introduction

In this section, the sensors used for the measurements presented in this work will be described, along with a detailed explanation of the dLGAD concept. Table 3.1 shows the single-LGAD (sLGAD) and dLGAD sensors used in these studies. It is important to note the following: the 50 μm sensors serve as a reference for the ultra-thin sensors, which are the devices under test (DUT). While the 50 μm sensors are manufactured by Hamamatsu Photonics K.K. (HPK), Japan, the ultra-thin silicon sensors are produced by Fondazione Bruno Kessler (FBK), Trento, Italy.

Sensors	HPK50 (A-B-E)	FBK35 (10-8-7)	FBK25 (10-8)	FBK20 (15-18)	FBK15 (15-13)
Thickness (μm)	50	35	25	20	15
Area (mm^2)	1.3x1.3	1x1	1x1	1.3x1.3	1.3x1.3

Table 3.1: This table shows the names of the sensors and the definitive nomenclature used in the rest of the chapter. The first number indicates the thickness, while the second number/letter, between brackets, indicates the name of the sensors.

It is also important to specify an interesting detail: these sensors are optimised for the study of charged particles and for timing characterisation, but laboratory measurements with photon sources are essential to obtain a characterisation of the sensors before the test beam. However, as expected, photons were not observed to penetrate beyond the sensor, making the application of the dLGAD feasible only for charged particles during the test beam. This highlights the importance of preliminary laboratory characterization of the sensors in preparation for the test beam, as understanding the response of both sensors on each side of the PCB becomes crucial.

It is also important to explain how the dLGAD, figure 3.4a, is built in the laboratory. To create this module, it is necessary to understand the electrical characteristics of the sensors. In other words, two similar sensors are required to achieve improved time resolution. It should be noted that this improvement will never be as significant as $\sqrt{2}$, as might be expected, because the signals from the sensors will always differ due to the statistical nature of the signal generation process. Therefore, when constructing a dLGAD, it is necessary to select two sensors with the same thickness, a similar breakdown voltage, and, most importantly, a comparable IV characteristic. This preliminary characterization is essential to ensure that the behavior of the sensors is comparable or at least consistent. Once the sensors have been selected, they must be bonded to

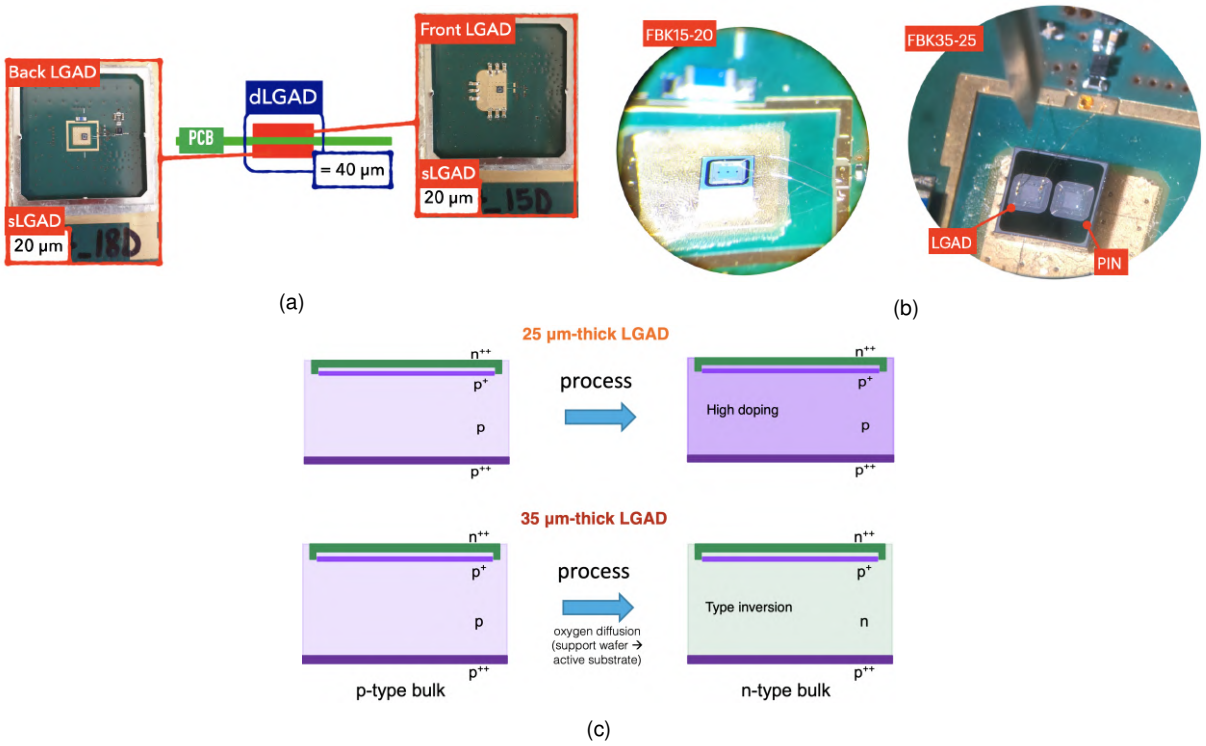

Figure 3.4: (a) This figure illustrates the two "sides" of the dLGAD, starting from the schematic presented earlier. (b) Microscope zoom of ultra-thin sensors with thicknesses below 50 μm. (c) Schematic showing the doping fabrication of FBK25 and FBK35 sensors.

the PCB, as shown in appendix B.1, using the machine illustrated in the corresponding figure. The sensors listed in the table for the dLGAD are those found to have similar characteristics and were therefore placed on the PCB accordingly.

The sensors exhibit different characteristics, as shown in figure 3.4b. Specifically, the 35-25 μm-thick prototypes are composed by two sensors: one is an LGAD (the bonded one), and the other is a PIN with the same layout of the LGAD. It is important to note that, despite the LGAD-PIN structure in the 35-25 μm sensors, only the LGAD is bonded, so the PIN is essentially inactive since it is disconnected from the circuit. Finally, figure 3.4c shows a schematic of what occurred during the silicon wafer fabrication, which led to a type inversion for 35 μm-thick sensors. While this factor should not impact the measurements, it could potentially affect performance under beam exposure, despite the high radiation hardness of these silicon sensors. Instead, a 25 μm-thick sensors have higher doping, which increases the internal gain of the sensors. This can be both an advantage, as it compensates for the reduced thickness, and a disadvantage, as it increases the noise of the devices.

3.2 IV characterization

The goal of this initial test is to measure the reverse current of the device as a function of the applied voltage across its electrodes and to extract the breakdown (BD) voltage. The measurement was conducted with the device integrated into the circuit mounted on the PCB, so the current behavior will differ from what would be observed with the bare sensor. However, the breakdown voltage value should remain consistent. The setup used is shown in figure 3.5. The sensors were affixed to the printed circuit board, after which one of the two sensors positioned on the front side was bonded and the

IV characterisation was conducted. Subsequently, the sensor was unbonded and the other sensor, positioned on the back side, was bonded, and the IV characterisation of the other side was also performed. Finally, both sides were bonded, and the IV characteristics were analyzed to study how the current is distributed across the two sensors and the PCB circuits. For further details on the connections and outputs, refer to the appendix B.1, which explains how the front-end works.

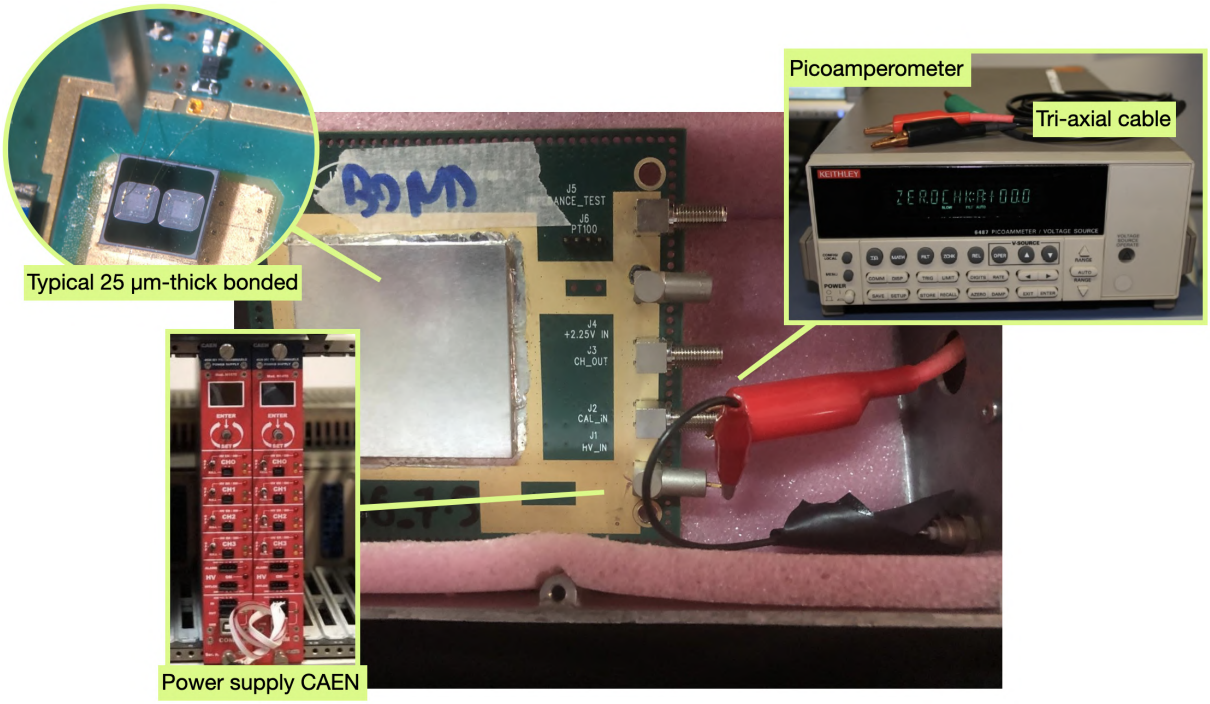

Figure 3.5: The sensor is placed inside a box that will be closed and covered to keep the sensor completely dark and shielded from any external electronic noise during data acquisition. The board is powered externally by a CAEN HV [78] power supply, and the central connector is connected to a Keithley 6487 picoammeter [79] for current measurements.

From the IV characteristics, it is possible to determine the breakdown voltage of the sensor, as previously explained. More importantly, it is also possible to highlight certain features, such as the sensor's working region (WR), which is important because these sensors operate away from the breakdown voltage.

3.2.1 IV Curve

This section presents some IV characteristics of several sensors. Figure 3.6 shows, as an example, the IV characteristics of a 20 μm sensor, highlighting the two main features of the curve: the two inflection points. The first inflection represents the gain layer depletion point (GLD), corresponding to the depletion of the doped layer, while the second inflection indicates the BD, where the current begins to rise sharply. The IV characteristic shown in the figure is influenced by the entire circuit mounted on the PCB; however, the main features remain evident. From these graphs, we can determine the working range of the sensors, which corresponds to the voltage range between the two inflections where the current is nearly constant.

The extraction of the breakdown voltage, as explained in the appendix, results in the BD values listed in table 3.2.2. Regarding the dLGAD concept, the IV characterization of a dLGAD compared to sLGAD is shown in figure 3.6. As the two sensors are in parallel, the resulting behavior is similar to one of the components. In addition to

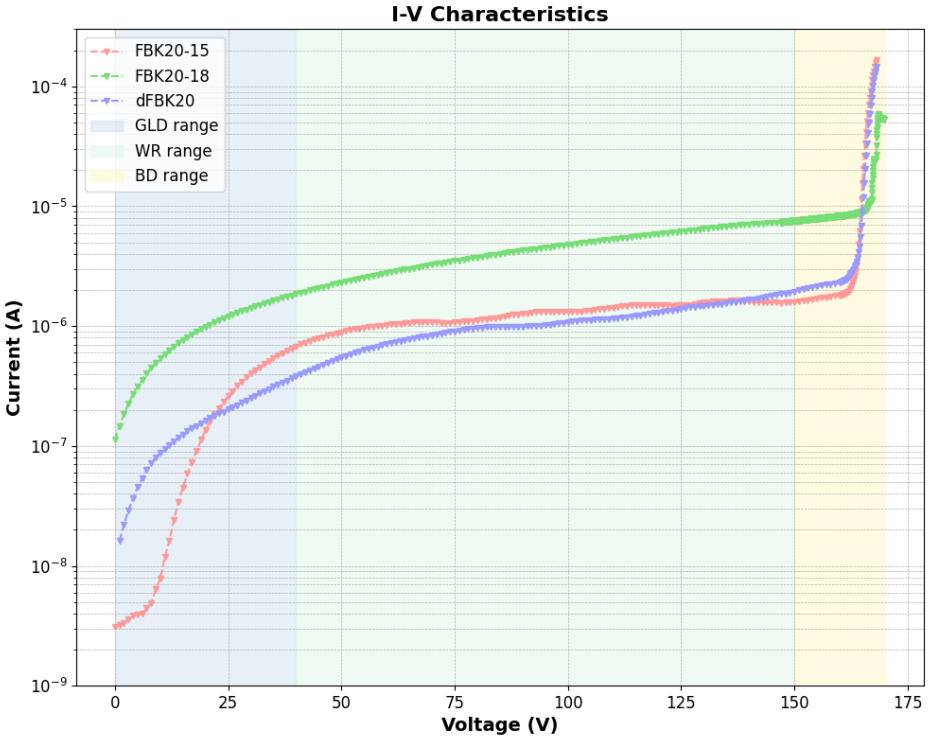

Figure 3.6: IV characteristic of the LGAD sensor from a FBK20 sensor, showing a comparison between the sLGAD and dLGAD.

determining the operating point, another main objective of these curves was to assess the uniformity between the sensors in each pair. Since they are mounted on the same board and powered with the same voltage, it is crucial that they deliver the same current and reach breakdown at the same voltage. The test was repeated for all available sensors; however, for practical reasons, these results are only shown in the appendix to keep the main text concise.

3.2.2 Extracted Breakdown Values

This section presents the extracted breakdown values (see table 3.2) from the subsequent analysis conducted according to the code. Details of the procedure are provided in the appendix. The associated uncertainty were assigned considering the applied voltage values: the last significant digit of the voltages was unity, so the uncertainty associated with the voltages is 1 V.

Sensors	BD (V)	Sensor	BD (V)	Sensor	BD (V)
HPK50-A	*(235 ±1)*	*FBK25-10*	*(124 ±1)*	*FBK15-15*	(144 ±1)
HPK50-B	(238 ±1)	FBK25-8	(132 ±1)	FBK15-13	*(149 ±1)*
dHPK50	(239 ±1)	dFBK25	(134 ±1)	dFBK15	*(152 ±1)*
FBK35-7	(267 ±1)	FBK20-15	(167 ±1)		
FBK35-10	(263 ±1)	FBK20-18	(168 ±1)		
dFBK35	(268 ±1)	dFBK20	(168 ±1)		

Table 3.2: Table showing the breakdown voltages (BD) for all sensors. To reference the thickness, please see table 3.1. Sensors are listed alternately in single and double configurations along with their respective BD values.

Note that in table 3.2, the FBK35-8 and HPK50-E sensors are not included, as

they are used only for specific measurements (for example in appendix C.2.2). This omission is for clarity, as all the sensors listed are paired within the dLGAD sensor, but they show same characteristics as others.

3.3 Study of energy resolution with iron-55 source

The studies on energy resolution were conducted at the ALICE TOF laboratory located at Via Irnerio 49. The experiment was carried out using an iron-55 (^{55}Fe) source, which predominantly emits photons with an energy of 6 keV and has a specific activity of 2.4×10^3 Bq. The experimental setup is shown in figure 3.7.

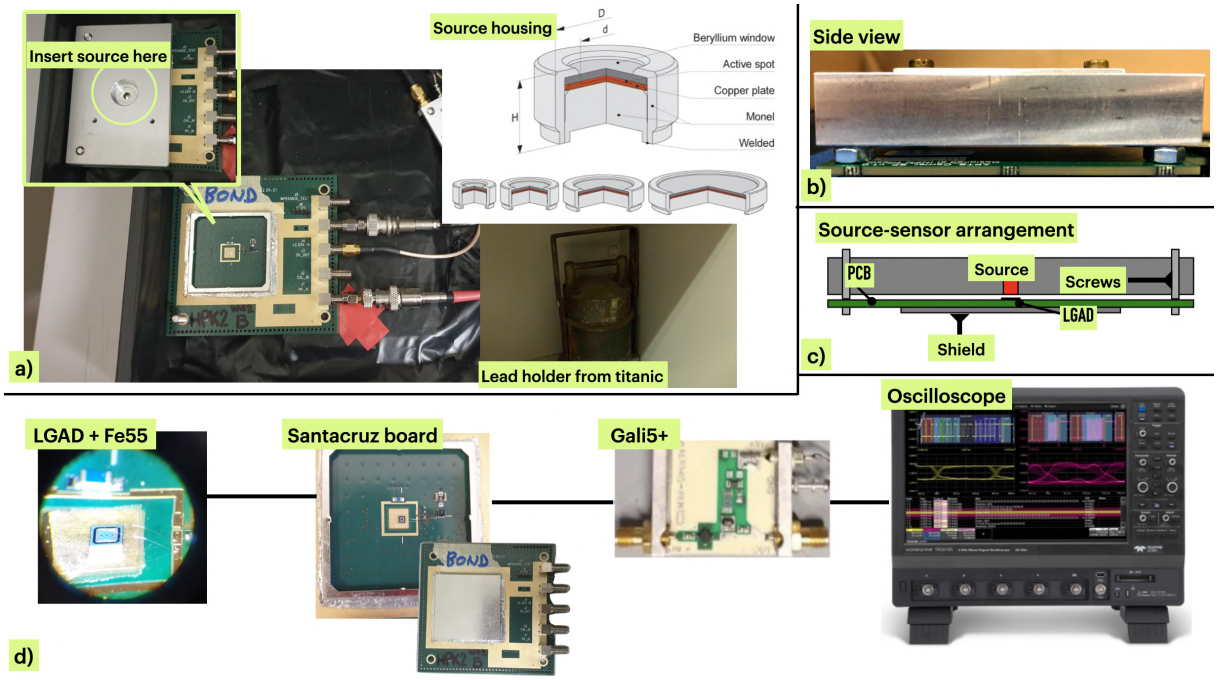

Figure 3.7: (a) Experimental setup used for the measurements, including specific details regarding the source's placement and confinement. (b) Side view of the experimental setup. (c) Schematic side view highlighting all components, including those not visible in the physical setup. (d) Connections used to send the signal to the oscilloscope.

In figure 3.7a, the experiment is shown to be conducted inside a box covered with black insulating tape. The source is placed within a 16 mm diameter hole in the source container, as shown in the figure. The source itself is cylindrical, forming the source holding structure as depicted. This source holding structure is inserted into a rectangular container that limits the source's activity and emission. Specifically, there is a 5 mm aperture at the bottom, which collimates the emitted photons towards the sensor below, suppressing most of the emission in other directions. When not in use, the source is stored in a lead holder, as illustrated in the figure.

Figures 3.7b-c provide a side view of the relative positioning of the sensor and the source. Lastly, figure 3.7d shows the measurement setup: the signal generated by the sensor is converted into a voltage by the Santacruz transimpedance amplifier and then sent to the Gali5+ amplifier [80], which further amplifies the signal before sending it to the oscilloscope. It is important to note that the Santacruz amplifier requires a supply voltage of 2.25V, while the Gali5+ amplifier operates at 12.5V, provided by a programmable RHODE & SCHWARZ HMP4040 power supply with four channels. The

oscilloscope used is a Teledyne LeCroy WaveSurfer High Definition [81] digital oscilloscope with 1 GHz bandwidth and a sampling rate of 5 GS/s. Although not shown in the figure, the high voltage for the sensor is supplied by a CAEN power supply module [78].

A typical signal observed on the oscilloscope is shown in the following figure 3.8, where an HPK50-B sensor is used as an example. The main issue with this setup is the noise; the random nature of the source's emission makes it impossible to use a trigger, so it is challenging to discern the signal from the noise. Therefore, a fixed threshold will be applied to the sensor for all runs performed.

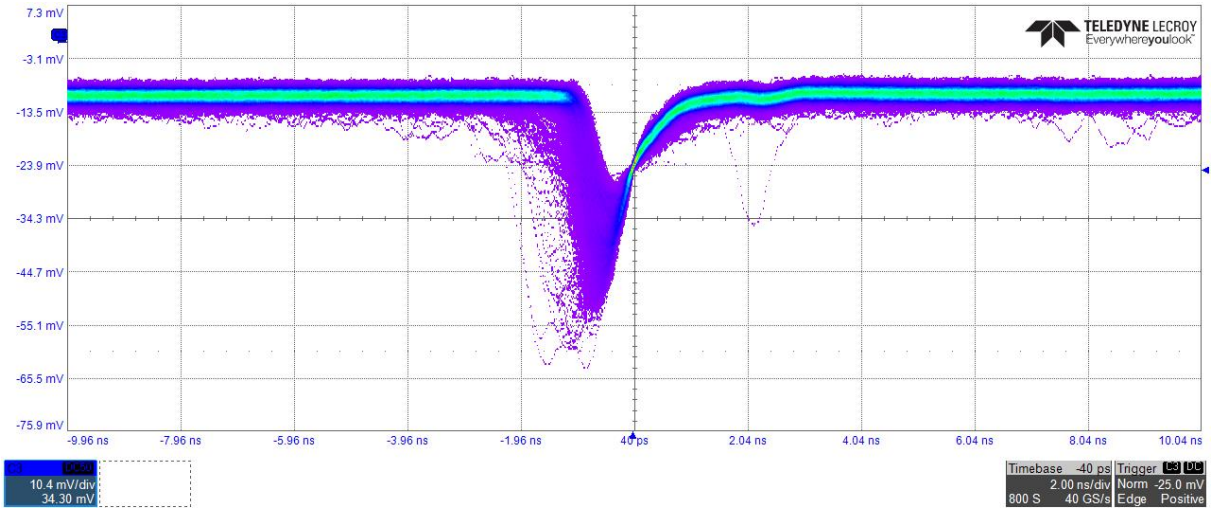

Figure 3.8: Typical negative signal observed on the oscilloscope from an LGAD HPK50-B used as a reference and test sensor. The signal was identified within a 20 ns window, as shown.

It should be noted that this fixed threshold was determined by considering the average of the maximum amplitudes obtained from a sensor acquisition without the source. Additionally, the IV characterization carried out in the previous section is crucial, as these sensors operate below the breakdown voltage. Therefore, it is necessary to identify an operating region (green area in figure 3.6). However, it is also essential to create an electric field strong enough to ensure a signal distinguishable from noise, which is easier in thicker sensors but more challenging in thinner sensors like the 20-15 μm ones, where the signal is around 15 mV considering all amplification. Working near the BD region introduces significant electronic noise, which spoils the performances of the sensor. In some cases, tests were conducted very close to this region to observe the behavior of energy resolution, but the best results were obtained within the operating range where the current remained roughly constant.

3.3.1 Introduction to experimental variables

In this section, the figures of merit concerning the energy resolution study with a source will be explained. The primary objectives and main focus are as follows: energy resolution as the primary target and main study, gain for comparing sensors of different thicknesses based on the deposited charge, and the number of electron-hole pairs as an alternative reference metric instead of gain. In addition, the signal-to-noise ratio will be taken into account. The associated uncertainties are the result of the semi-dispersion from the resolution values calculated from two acquisitions under the same experimental conditions; the value obtained is 5%.

3.3.1.1 Peak Resolution

Starting from the signal observed in figure 3.8, the analysis will involve inverting the signal by multiplying it by -1 to make it positive to allow the main procedures for all the types of sensors connected any number of amplification stages. Due to the noise affecting the setup, a significant amount of statistical data is necessary; therefore, it is considered reasonable to analyze around 250,000 waveforms. At this point, it will be necessary to select the signal region, taking into account the baseline. The maximum amplitude value will then be calculated for each waveform within the signal's time window. The baseline is determined by observing the distribution of maximum amplitudes in the time window preceding the signal. In our case, the signal's time window was between -1 ns and 1.4 ns, with a total signal window ranging from -11.6 ns to 9.4 ns, so the noise was calculated from -11.6 ns to -1 ns. Another interesting detail is that, contrary to what was described in C.1, the analysis revealed that the LGAD is capable of detecting a single distinct peak, as shown in figure 3.9. This makes it inappropriate to discuss energy resolution; instead, we should only refer to the resolution of the observed peak, given the ambiguity.

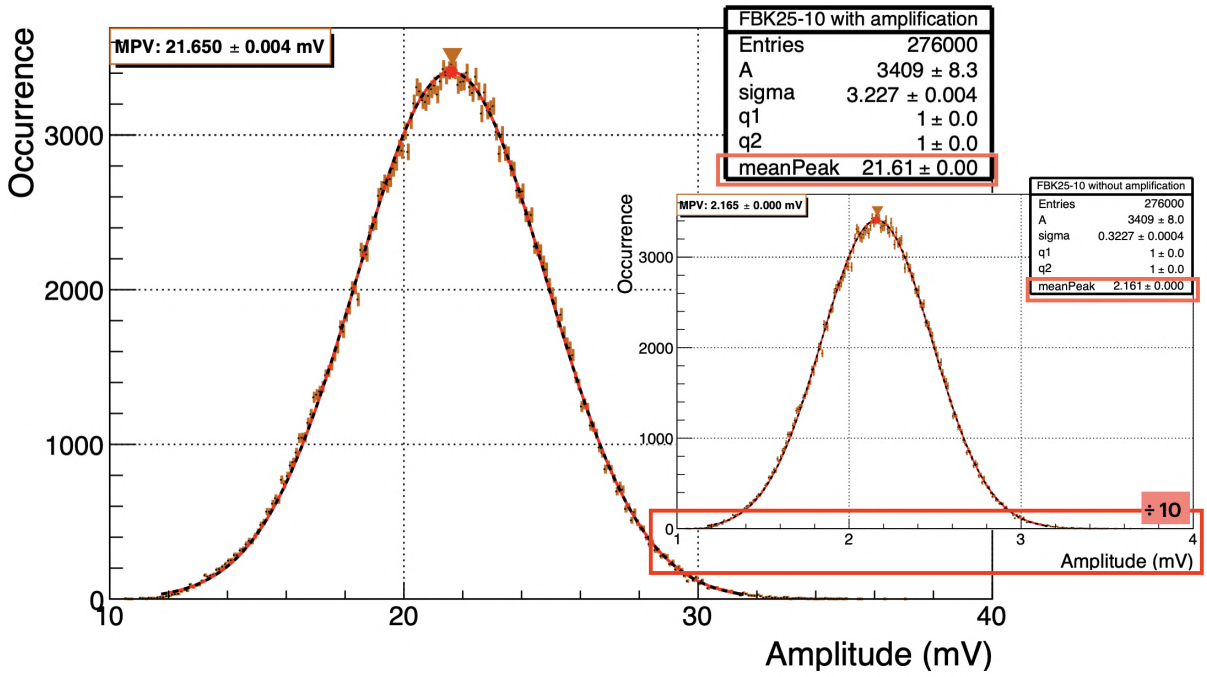

Figure 3.9: Example of the amplitude distribution plot for the FBK25-10 sensor at 80V, with a q-Gaussian fit applied, with and without the amplification factor.

The histogram shown in figure 3.9 is essential for determining the peak resolution, as it directly relates to the resolution of the peak associated with the photon from the source. The primary curve in the larger plot represents the results obtained after signal amplification. In contrast, the second curve illustrates the results after compensating for the amplification effect, specifically by removing the amplifier's contribution (with a gain factor of 10, as indicated in the label) from the Gali5+. It is important to note that the peak resolution itself does not improve by simply removing the amplification factor, as the amplification is a linear multiplication of the signal. Nevertheless, the analysis was performed without considering the amplification.

The principle behind the amplifier's gain is straightforward: the output signal from the module is multiplied by a specific factor, which is determined using the relationship shown in equation 3.3.1:

$$A_{Gain} = \frac{V_{out}}{V_{in}} = 10^{\frac{G_{DB}}{20}} \tag{3.3.1}$$

Here, $\frac{V_{out}}{V_{in}}$ represents the ratio between the output voltage (V_{out}) and the input voltage (V_{in}) to the amplifier, with the input voltage being the unknown variable of interest. The value of G_{DB} is the gain in decibels as specified by the amplifier's datasheet. Finally, A_{Gain} represents the desired amplification factor. The systematic uncertainty associated with the amplification will be not considered as other sources of noise since all measurements are done with same experimental conditions.

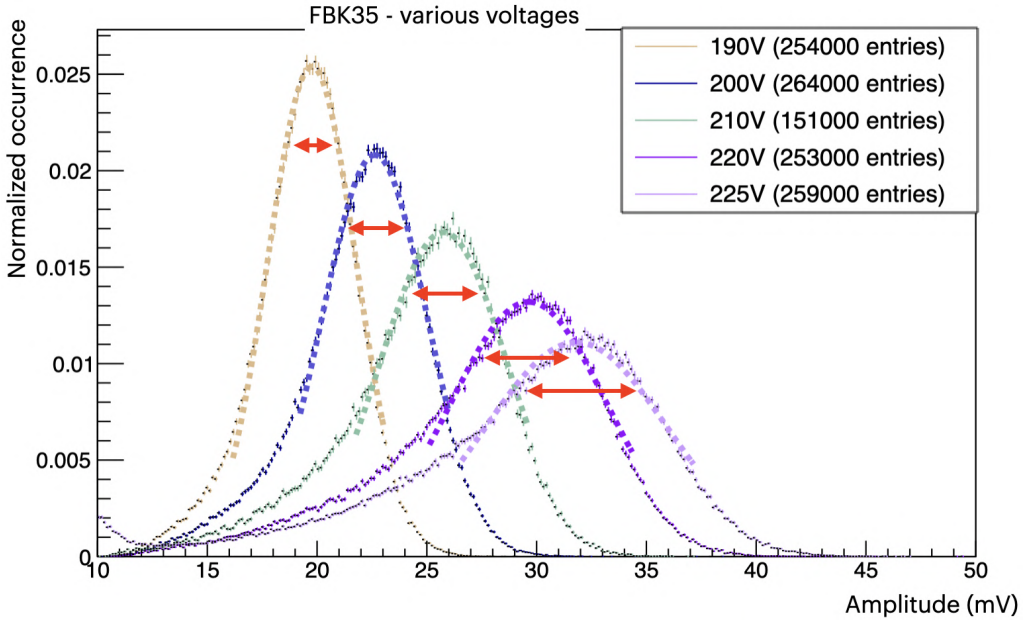

Figure 3.10: Amplitude distribution for the FBK35-7 at various voltages, with each curve fitted using a simple Gaussian. This plot is intended for illustrative purposes only.

Figure 3.10 shows an illustrative comparison of the amplitude distribution at various voltages for an FBK35-7 sensor, with each curve fitted using a Gaussian function. The observation indicates that the distribution broadens concurrently with the peak shift, suggesting that resolution degrades as the voltage increases. This deterioration could be attributed to the statistical nature of the process and the difficulty of the sensor in detecting photons at low gain.

It is evident, as also noted in figure 3.9, that the distribution significantly deviates from a Landau curve. This deviation is reasonable considering that the sensor is capable of stopping the particle (electron produced by photon interaction) attempting to pass through it, with the tail of the distribution attributed to particles escaping, as will be discussed in subsequent sections. In fact, we measured the skewness for each sensor and for each voltage, and it is consistent with the above, although a slightly increasing value was noted with decreasing thickness. The reason why the skewness increases with decreasing thickness could be related more to a reduction in the signal combined with an increase in the experimental noise factor than to a physical case where particles are able to escape from the sensor.

Therefore, it was proposed that fitting with a q-Gaussian (see equation 3.3.2), which accounts for the tails, might be more appropriate. Moreover, the amplitude distribution exhibits a left-side tail (see again figure 3.10), which must be accounted for. That left-side asymmetry can be explained by the fact that a threshold is pre-selected during

the acquisition. In thicker sensors, such as the 50-35 μm ones, the signals are significantly larger than this threshold. This results in a "plateau" to the left of the histogram peak, leading to a pronounced left-side asymmetry that a simple Gaussian fit cannot adequately capture. However, by using a q-Gaussian:

$$f(x) = \begin{cases} A\left[1-(1-q_1)\left(\frac{1}{3-q_1}\right)\frac{(x-meanPeak)^2}{\sigma^2}\right]^{\frac{1}{1-q_1}}, & \text{if } x \leq meanPeak, \\ A\left[1-(1-q_2)\left(\frac{1}{3-q_2}\right)\frac{(x-meanPeak)^2}{\sigma^2}\right]^{\frac{1}{1-q_2}}, & \text{if } x > meanPeak. \end{cases} \tag{3.3.2}$$

and removing part of the plateau before fitting, it is possible to better account for and represent the data. In equation 3.3.2, $meanPeak$ represents the mean value of the distribution, while $q_{1/2}$ denote the asymmetry of the tail on the left and right sides, respectively. Typically, $q_{1/2}$ values range from 1 to 2. The parameter A is the normalization amplitude, serving as the multiplicative constant, and σ represents the resolution of the fit, corresponding to the standard deviation. The peak resolution σ_{peak} can be extracted using the following expression:

$$R = \frac{\sigma}{meanPeak} \cdot 100 \tag{3.3.3}$$

In equation 3.3.3, R represents the resolution of the peak, expressed as a percentage.

3.3.1.2 Charge

The gain, being the internal charge multiplication factor within the sensor, is a crucial tool for comparing sensors of different thicknesses and it also helps to understand the impact of the gain layer on the energy resolution calculation. In this context, it is necessary to revert to the potential without the gain factor from the amplifier, as well as from the SantaCruz transimpedance board. The first step involves calculating the charge deposited within the sensor using the following formula 3.3.4. Since we have a discrete dataset of points, a discrete integral is required to compute the charge.

$$Q(fC) = \sum \frac{(S(mV) - B(mV)) * \delta_T(ps)}{A_{Gain} * R_{board}(\Omega)} * 1000 \tag{3.3.4}$$

In equation 3.3.4, the final factor of 1000 converts the result into femtocoulombs (fC). Here, S represents the signal amplitude, at each point of the waveform inside the chosens signal window, while B refers to the most probable value of the backgound noise histogram found on the first part of each waveform, considering part before the signal window, where only the noise is present. The parameter A_{Gain} is the gain of the amplifier (see 3.3.1), used as in the previous section, and R_{board} is 470Ω, representing the resistance encountered by the current from the sensor's output on the PCB. The formula 3.3.4 provides a charge histogram, as shown in figure 3.11. Once the histogram is obtained, a fit is performed, similar to the previous method, using a q-Gaussian function.

Figure 3.11 shows the fit performed. Unlike previous cases, it also displays the Most Probable Value (MPV) by fitting the signal with a q-gaussian. Conceptually, using the MPV value instead of the mean value would be more accurate, as charge deposition is subject to Landau fluctuations. However, given that the considered energy regime results in minimal Landau effects since photons are completely absorbed by sensor (skewness $\simeq 0.042 \pm 0.002$), the choice between $meanCharge$ and MPV is not

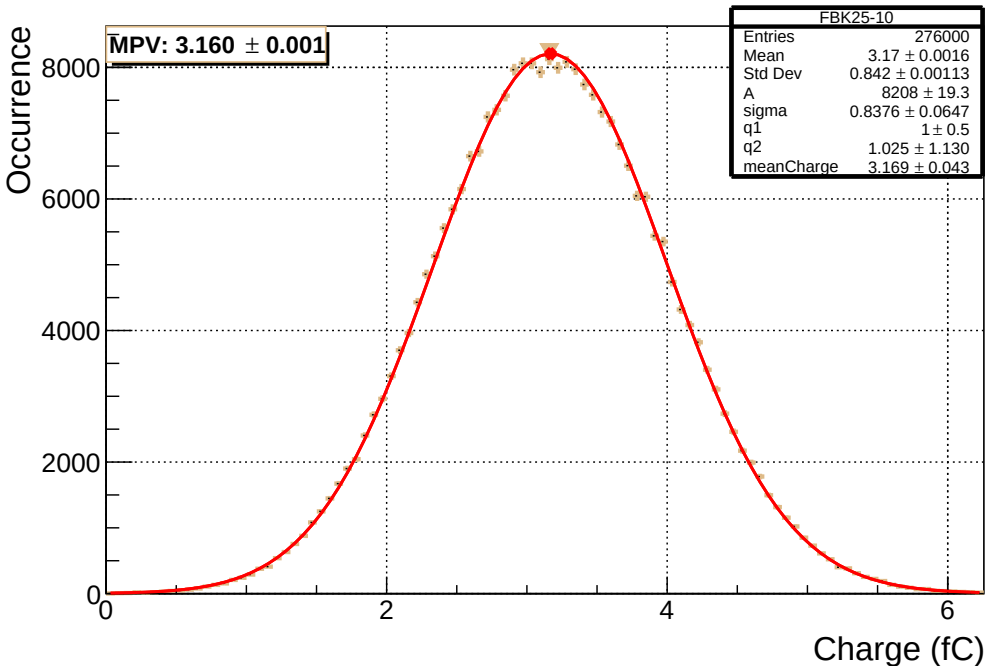

Figure 3.11: Example of a charge plot. For this example, the FBK25-10 sensor was used, analogous to the previous section. The brown arrow indicates the MPV bin, while the red dot represents the mean by fit.

significant. The mean value was extracted and called in the followig text MPV, while the associated uncertainty is extracted using semi-dispersion method from different runs at same conditions. Given the complex physics describing the process, it is not possible to extract the gain of the sensors in light of the fact that it is impossible to determine, given the statistical nature of the process, how much charge the particles produced in turn by the photon passing through the sensor can generate, as done with beam data (in section 3.4.1.2). For this reason, the deposited charge and not the gain will be used to compare the results.

3.3.1.3 Number of electron-hole pairs

The number of electron-hole pairs is another way to recalculate the charge (equation 3.3.5). This can also be used as a comparison metric to understand the energy resolution and its impact. It can be extracted as:

$$N_{e-h} = \frac{Q}{(q \cdot 2)} \tag{3.3.5}$$

where Q is the deposited charge and q the elementary charge. Similarly to previous analyses, it is possible to create a histogram and perform a fit to extract the mean or the most probable value for each sensor.

3.3.1.4 Signal-to-noise ratio (S/N)

The final variable of interest is the signal-to-noise ratio (S/N), which is crucial because it represents how much larger the signal is than the noise. It is a tool for understanding how much larger the signal is compared to the noise and is calculated using the formula

shown in equation 3.3.6. Here, rms_B refers to the root mean square of the background noise.

$$S/N = \frac{S(mV) - B(mV)}{rms_B(mV)} \tag{3.3.6}$$

As with previous analyses, a histogram of the signal-to-noise ratio is generated, as illustrated in figure 3.12. Instead, the most probable value (MPV) is extracted and used for subsequent analysis. It should be noted that in this instance, the results are not divided by amplification factors, as was done for the maximum amplitude. Instead, the results are taken directly, considering amplification. This approach accounts for all sources of electronic noise that may add to the signal and noise.

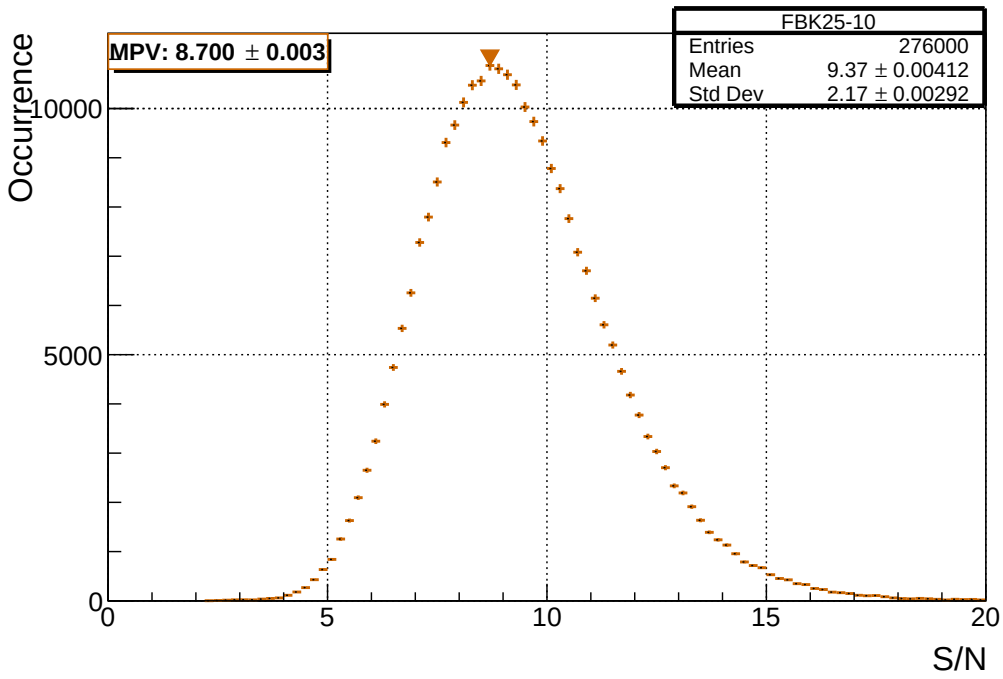

Figure 3.12: Histogram of the calculated S/N for FBK25-10 as shown in the formula 3.3.6. The brown arrow indicates the MPV again.

3.3.2 Analysis with various thicknesses

This section presents the initial results obtained using the setup described in 3.7 to test the resolution of silicon sensors with varying thicknesses, ranging from 50 to 15 μm. For the purposes of this discussion, only the results from the sensors HPK50-B, FBK35-7, FBK25-10, FBK20-13, and FBK15-18 will be considered. For simplicity, the second part of each sensor's name will be omitted, and it will be assumed that the reference is to the specified sensor. Subsequently, a comparison between the various sensors will be shown, focusing on gain and other relevant parameters. The results obtained, along with the key parameters, are presented in table 3.3 below.

In general, the resolution is shown in figure 3.13. It is important to note that this graph only shows the obtained resolution and serves as a visual tool, not for direct comparison. Since the working region, identified in the previous section, was not always fully exploitable especially for thin sensors such as those with 20 and 15 μm of thickness, a distinguishable signal from the noise could only be achieved at high voltages, often close to the BD range. In this region, there is generally more noise due

to the randomness in multiplication, which plays a more significant role in sensors with a gain layer, such as LGADs (remembering that the photon is completely absorbed). As can be seen, thicker sensors, like those with 35 and 50 μm, generally exhibit better resolution. However, it should also be noted that for these two sensors, it is possible to obtain a larger signal at lower voltages, though this is not shown in this section but was verified experimentally.

Sensors	Voltage (V)	Charge (fC)	R (%)	Sensors	Voltage (V)	Charge (fC)	R (%)
HPK50	190	(5.9 ±0.3)	**9.4**	**FBK25**	80	(3.0 ±0.2)	**14.7**
	200	(6.8 ±0.3)	**10.7**		90	(3.5 ±0.2)	**15.9**
	205	(7.2 ±0.4)	**11.7**		95	(3.9 ±0.2)	**16.6**
	210	(8.0 ±0.4)	**13.2**		100	(4.0 ±0.2)	**17.7**
	220	(9.0 ±0.5)	**16.4**		105	(4.3 ±0.2)	**19.5**
	225	(9.4 ±0.5)	**18.5**		110	(5.3 ±0.3)	**22.4**
FBK35	190	(2.1 ±0.1)	**10.2**	**FBK20**	120	(3.1 ±0.2)	**13.0**
	200	(2.5 ±0.1)	**10.7**		130	(3.4 ±0.2)	**14.6**
	210	(2.8 ±0.1)	**11.6**		140	(3.9 ±0.2)	**16.4**
	220	(3.2 ±0.2)	**12.5**		150	(4.4 ±0.2)	**21.9**
	225	(3.5 ±0.2)	**13.1**	**FBK15**	120	(2.2 ±0.1)	**14.7**
	230	(4.0 ±0.2)	**14.3**		130	(2.5 ±0.1)	**15.1**
					135	(2.7 ±0.1)	**19.0**
					140	(3.2 ±0.2)	**22.7**

Table 3.3: Results obtained for various sensors, including gain and energy resolution at different voltages. The uncertainties associated with values reported in table are 5% of the value.

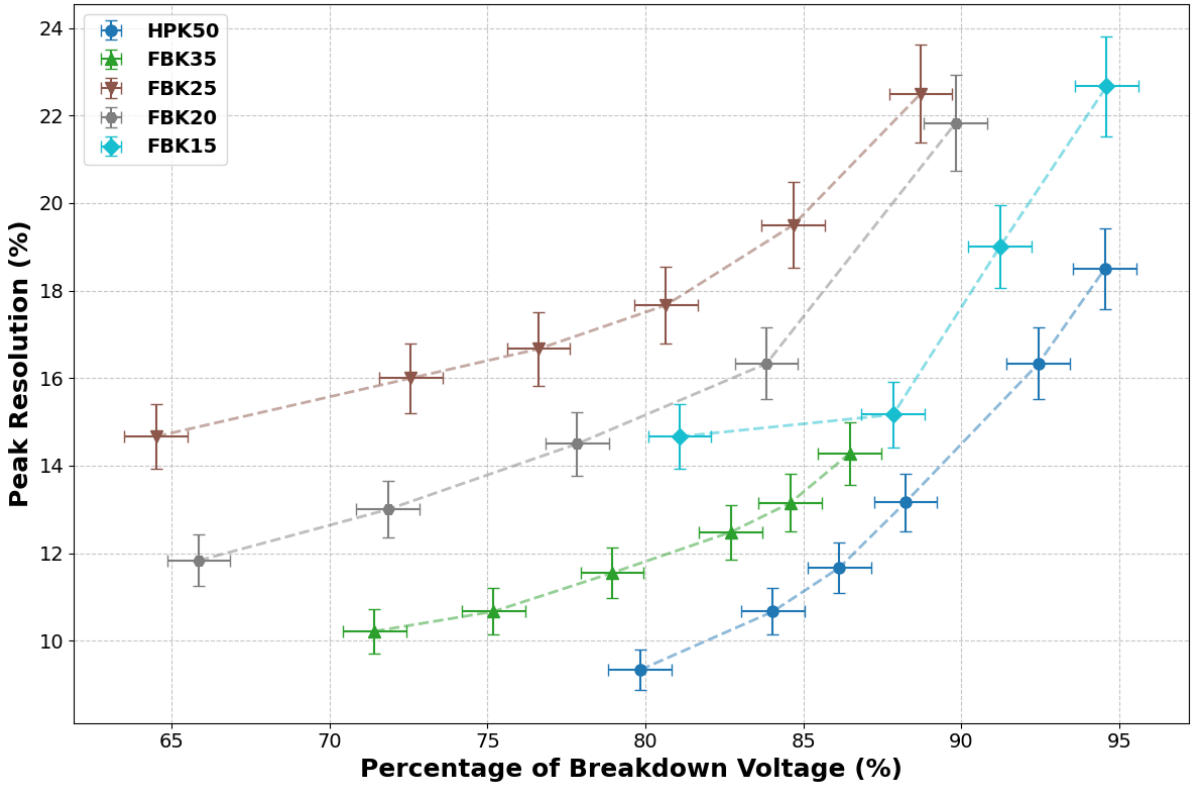

Figure 3.13: Plot showing results from several sensors as a function of various percentage voltages relative to their BD values.

On the other hand, thinner sensors, such as those with 25, 20 and 15 μm of thickness, generally show poorer resolution. Specifically, for the 15 μm sensor, it becomes evident that it is not feasible to operate in a region far from the BD point, thus affecting the measurements. In this context, it is important to note that resolution depends not only on thickness but also on gain in these sensors, consequently on the number of e-h pairs created as shown in figure 3.14. High gain increases noise due to the randomness in multiplication, but it also enables higher signal levels within the possible limits. For these sensors, it was much more challenging to operate in a low-gain region within the WR region, precisely due to the reduced thickness and low gain at low voltages, which makes the signal less distinguishable from the noise.

It can be observed that despite the reduced thickness of the 15 and 20 μm, as illustrated in figure 3.14, the number of pairs is almost comparable, indicating a significant gain from these sensors. This is supported by the data in table 3.3, which suggests that the high gain should balance the reduced thickness of these sensors.

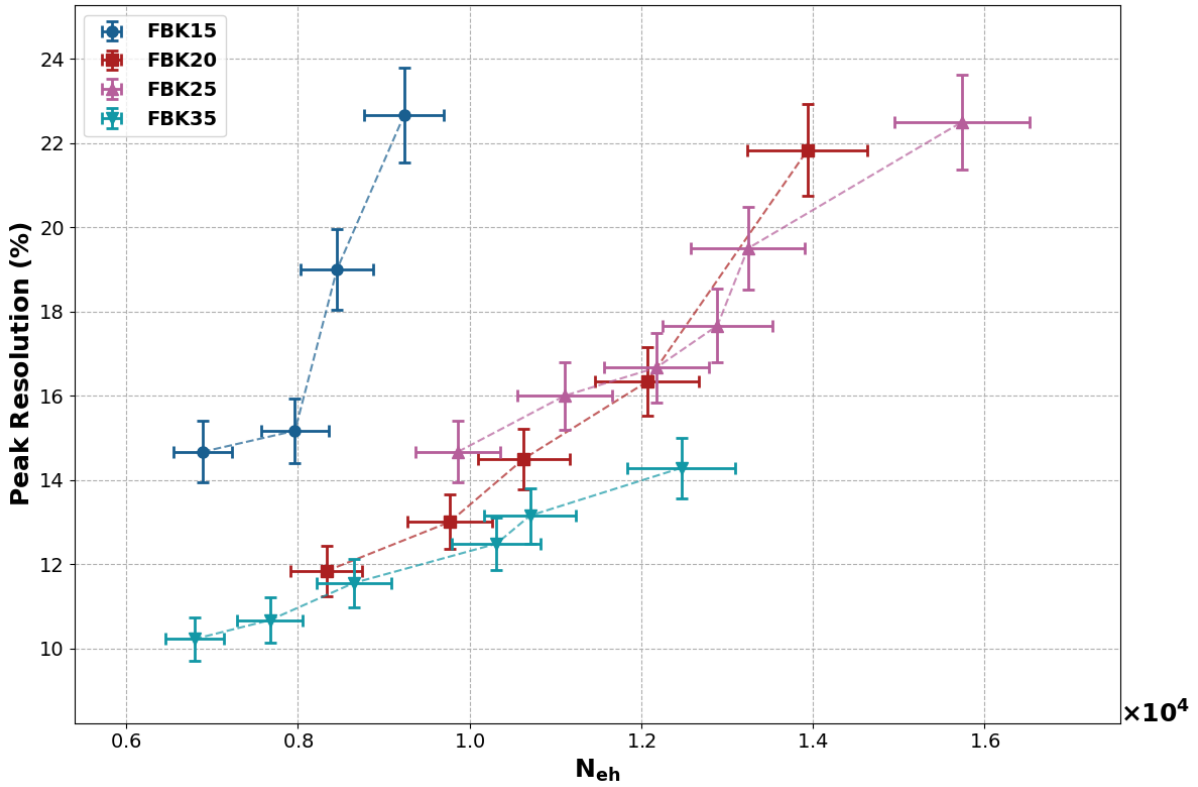

Figure 3.14: Peak resolution as a function of the number of electron-hole pairs created for the various sensors. As HPK50 exhibited a markedly higher number of pairs, it has been excluded from the plot for the sake of clarity.

Additionally, a run with/without a source was conducted to ascertain how electronic noise varies as a function of thickness. This is illustrated in table 3.4. As can be observed, the thin sensors exhibit a higher average RMS than the 35 and 50 μm sensors. Such electronic noise affected the measurements.

With regard to the acquisition of the results illustrated in table 3.4, the outcomes attained with the source are derived based on the baseline preceding the signal. The associated calculation is presented in paragraph 3.4.1.3. In the case of source-less acquisition, the RMS was extracted from the waveforms obtained in the absence of a signal. It is also notable that the presence of a source results in an increase in noise levels. Furthermore, it is important to highlight that the FBK20 signal is characterised by high levels of noise, making it unsuitable for measurement purposes.

Sensors	HPK50	FBK35	FBK25	FBK20	FBK15
RMS (mV)	(1.1 ±0.1)	(1.4 ±0.1)	(1.6 ±0.1)	(3.3 ±0.2)	(1.9 ±0.1)
RMS (mV)	(1.00 ±0.1)	(1.2 ±0.1)	(1.4 ±0.1)	(2.4 ±0.1)	(1.3 ±0.1)

Table 3.4: Average RMS obtained with (first row) and without (second row) source analysis for sensors of different thicknesses. For simplicity, the associated uncertainty has been rounded to the first decimal place.

Therefore, the subsequent analysis will be divided as follows: sensors with thicknesses of 35 and 25 μm will be discussed in a dedicated section 3.3.2.1, while those with 20 and 15 μm will be addressed in the appendix C.2.1. The reason for this separation is not primarily related to thickness but rather to the unreliability of measurements obtained with thinner sensor. The 50 μm sensor due to its greater thickness showed a much larger amount of deposited charge and number of pairs created, which is why it cannot be used to compare the results obtained with the other sensors. This is shown in the table 3.5 where the number of pairs created, and S/N, as a function of certain applied voltages is given. The deposited charge can also be derived using the relationship given in equation 3.3.5. The best resolution with this sensor was also obtained because it has a much higher S/N value than the other sensors.

In addition, on this type of sensor and on a 35 μm-thick sensor, we did a potential scan to identify the best region to make these measurements (see section in appendix C.6 where we reproduced the results obtained with an FBK35 as an example). What we found is that the optimum working point for both sensors is around 50-60% of the BD value (for both sensors).

HPK50				
Voltage (V)	(190 ±1)	(200 ±1)	(210 ±1)	(220 ±1)
N_{eh}	18265	20665	24931	27864
S/N	25	29	36	43

Table 3.5: Results of N_{eh} and S/N for some bias applied. The uncertainty to be associated with the result is 5% in accordance with what was discussed above.

3.3.2.1 Comparison between 35-25 sensors

As shown in figure 3.13, the thicker sensors exhibit better resolutions. However, to accurately compare the results, it is essential to ensure that the conditions are consistent, meaning that the comparisons should be made at the same charge deposited or number of pairs created levels, as shown in figure 3.15. where the applied voltages are indicated as labels as well.

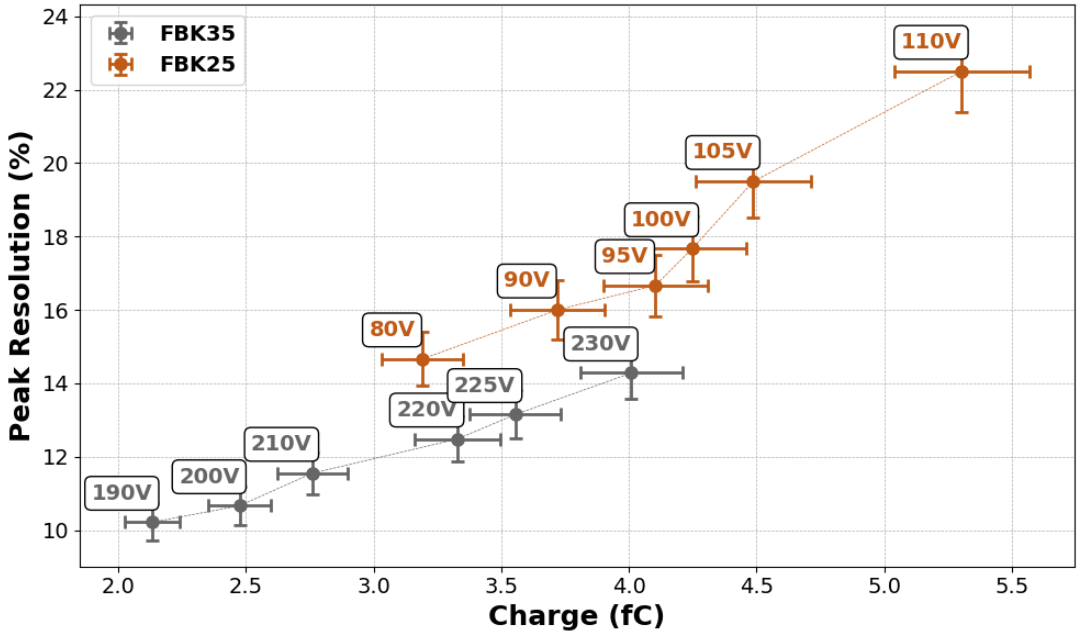

Figure 3.15: Peak resolution of sensors with thicknesses of 35 and 25 μm at various charge deposited.

The resolution at the peak, reported in figure 3.15, worsens as the charge deposited increases for both devices. An increase in resolution indicates a deterioration in the accuracy of peak measurement. This behaviour can be attributed to noise that increases proportionally with charge or to a rise in the dispersion of collected particles produced by photons. The discrepancy between the two curves is related to the fact that at the same charge FBK35 is already in the vicinity of the BD, while FBK25 on the contrary is in the WR region. In any case, the deviation between the two curves at the points where they are comparable is around 2%. However, this is not the only way to make a comparison; other variables can also be used to better explain the discrepancies.

At the same potentials and charge as in figure 3.15, additional results are shown in figures 3.16 and 3.17. In figure 3.16, it is evident that the resolution degrades as the number of generated electron-hole pairs increases.

In particular, a comparison of sensors revealed that the HPK50 provides better results, largely due to the higher number of electron-hole pairs generated (see Appendix C.2), which increases in line with the deposited charge, as is the case with all sensors. Conversely, the poorer results observed with FBK25 and FBK35 are primarily explained by the lower number of electron-hole pairs observed. Although FBK35 and FBK25 have a similar number of pairs, the higher charge deposited of FBK25 compensates for the difference in thickness, probably related to an intrinsic higher gain.

When comparing sensors at the same charge the discrepancy observed in figure 3.15 must be explained by something else. Therefore, we turn to the S/N ratio as a comparison metric, shown in figure 3.17, where it is evident that the S/N ratio is drastically worse, up to 50% less for the thinnest sensor with the same deposited charge.

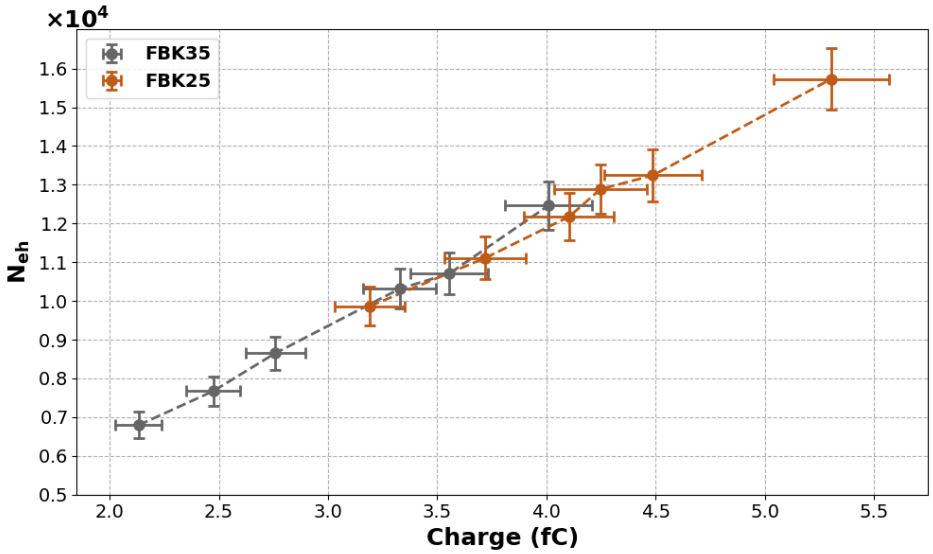

Figure 3.16: Plot of N_{eh} as a function of charge at the same potentials as in figure 3.15.

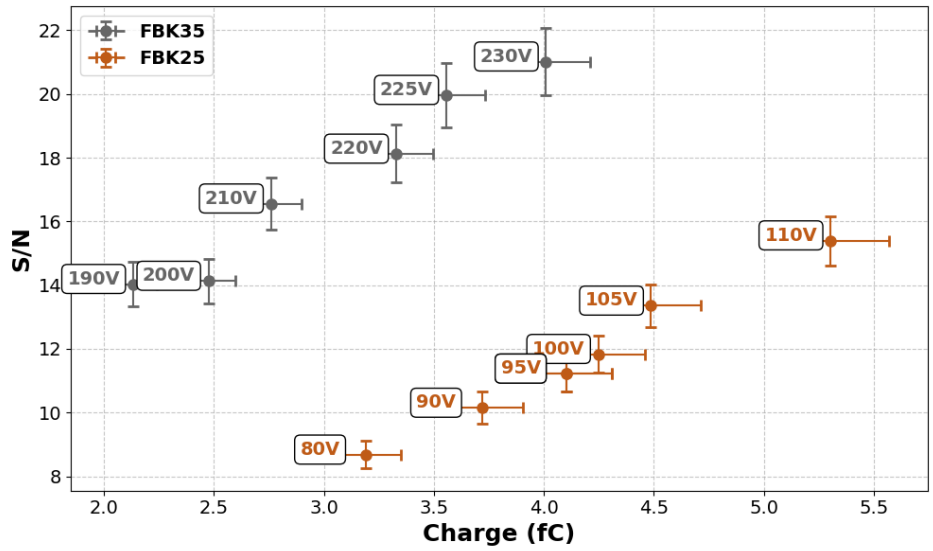

Figure 3.17: Plot of S/N as a function of charge at the same potentials as in figure 3.15.

The difference between the 35 and 25 μm sensors lies in the noise, which deteriorates the result. This noise is likely caused by the combination of reduced thickness and the probability of the photon converting into an electron, and consequently the statistical distribution of electron signal deposition, which is particularly important in thinner sensors.

3.4 Study with charged particles at beam facilities

In the following section, the results obtained with charged particles using a 10 GeV/c beam at the Proton Synchrotron (PS) [82] at CERN's beam facilities will be analyzed (figure 3.18).

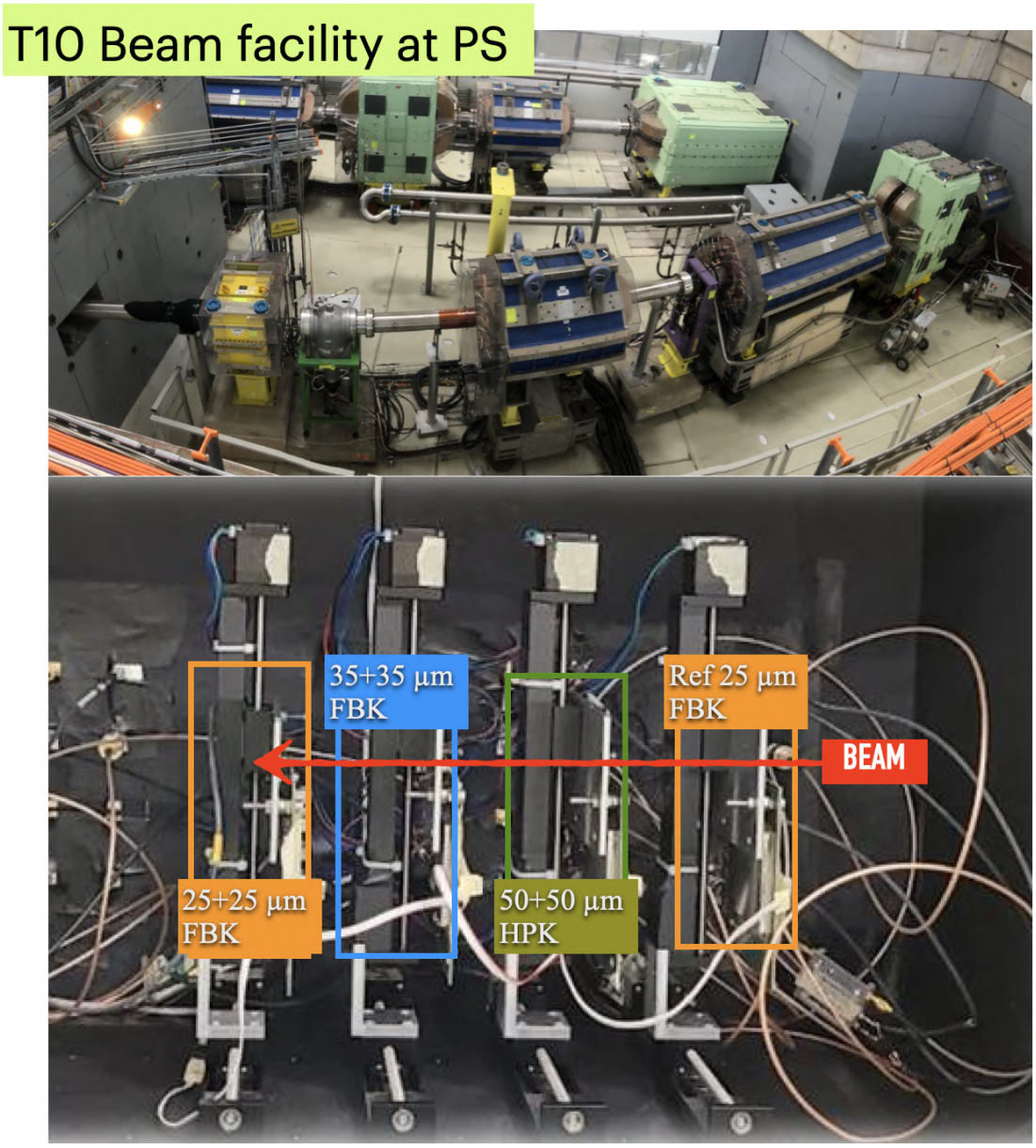

Figure 3.18: Top: An image of the PS magnets guiding the beam onto the target. Bottom: A diagram of the experimental setup with 4 LGAD sensors aligned for data acquisition, considering different thicknesses.

Of the sensors listed in the 3.2, 15 μm and 20 μm sensors will be analysed, with a particular focus on comparing the performance of single LGADs (sLGAD) against their double-layer counterparts (dLGAD). The experimental apparatus is shown in figure 3.18 where the sensors aligned on the beam line are shown: the first sensor acts as a time reference and trigger that signals events passing through the sensor. The system was made of four LGADs: the two devices under test (15-20 μm) and the other two LGAD detectors with a thickness of 35 μm set at 230 V. The whole setup was enclosed in a dark box at room temperature. The trigger was defined as the coincidence of the two 35 μm LGADs in the system. At each trigger, all four waveforms were stored using

a Lecroy Wave-Runner 9404M-MS digital oscilloscope. For the final offline analysis, the oscilloscope bandwidth was downscaled to 1 GHz. In general, we anticipate that these sensors will exhibit better performance with charged particles, and here, we will conduct a study on their time resolution, which is a crucial aspect of the ALICE 3 R&D. This will be complemented by an analysis of the peak energy resolution. In a subsequent section, comparisons with the performance under photon irradiation will be discussed. Overall, we expect better performance given the low gain of these sensors and a larger signal given by a charged particle.

3.4.1 Introduction to experimental variable

In this section, the figures of merit concerning the energy resolution study at beam facilities, are presented, while omitting those already explained 3.3.1 (e.g. S/N ratio). However, compared to the previous study with the source, it will instead be shown and explained how the time resolution is calculated in 3.4.1.4. Lastly, The associated uncertainties are the result of semi-dispersion from the resolution values calculated from three acquisitions under the same experimental conditions; the value obtained is 10%.

3.4.1.1 Peak resolution

As explained in section 3.3.1.1, the goal is to determine the peak resolution using the signal generated by a charged particle in the LGAD.

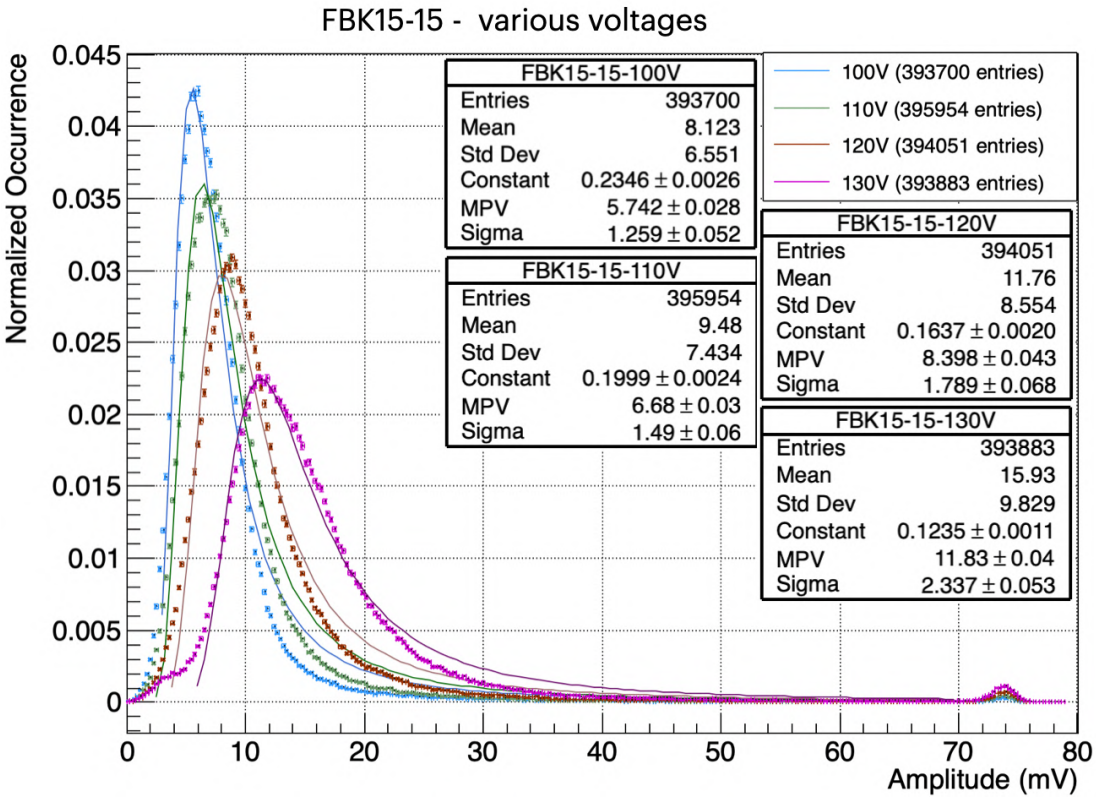

Figure 3.19: Amplitude distribution for the FBK15-15 at various voltages, with each curve fitted using a Landau. This plot is intended for illustrative purposes only.

However, despite having only one available energy, we will continue to refer to peak resolution for consistency. As one might expect, the signal shape will differ from what

is shown in figure 3.9, since the passage of a MIP (used in beam tests) is described by a Landau distribution, due to the fact that the particle escapes and is not stopped by the material. What we expect, as shown in figure 3.19 considering a FBK15-15, is a Landau distribution of signals that tends to increase in amplitude. However, unlike what occurs with the photon source, the distribution does not "broaden" as much, which is likely related to the different physical conditions.

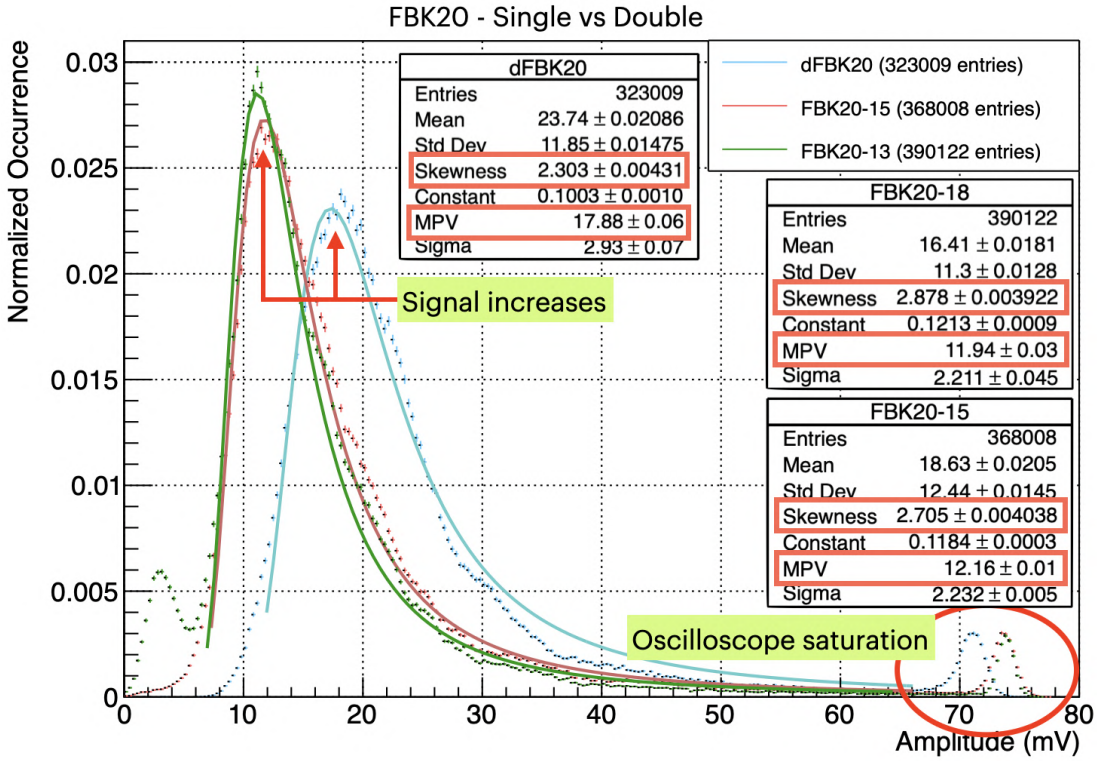

Figure 3.20: Amplitude distribution at 110 V for FBK20 showing the double LGAD vs single LGAD comparison. The distributions are fitted with a Landau function. This plot is intended for signal comparison purposes only.

In figure 3.20, the signal amplitude distributions for FBK20-15 and FBK20-18 are compared with their corresponding double LGAD (dFBK20) at 110V. We observe an improvement in the signal by approximately 33%, which agrees with the fact that the volume over which the charge is deposited is doubled. The second peak at very high amplitudes in both figures 3.19 and 3.20 indicates saturation of the signal at the oscilloscope. Another parameter to emphasise is skewness: it decreases by 18% when switching from single sensors to dLGAD (as explained in the D.2 section).

A more striking example of the skewness at low applied voltages from a Landau fit for FBK15-15 is shown in figure 3.21. The fit is performed with ROOT using the formula in the equation 3.4.1 where Landau$(x;\text{MPV},\sigma)$ is the non-normalised Landau distribution, with MPV the most probable value and σ the width of the distribution.

$$f(x;\text{MPV},\sigma) = \text{costant} \cdot \text{Landau}(x;\text{MPV},\sigma) \tag{3.4.1}$$

It seems to suggest that, the skewness is more evident as the sensor thickness decreases because energy deposition becomes less uniform and the particles are not stopped within the sensor's sensitive volume. Moreover, unlike the studies with the photon source (3.3.1.1), it is more appropriate to consider the most probable value (MPV) rather than the mean.

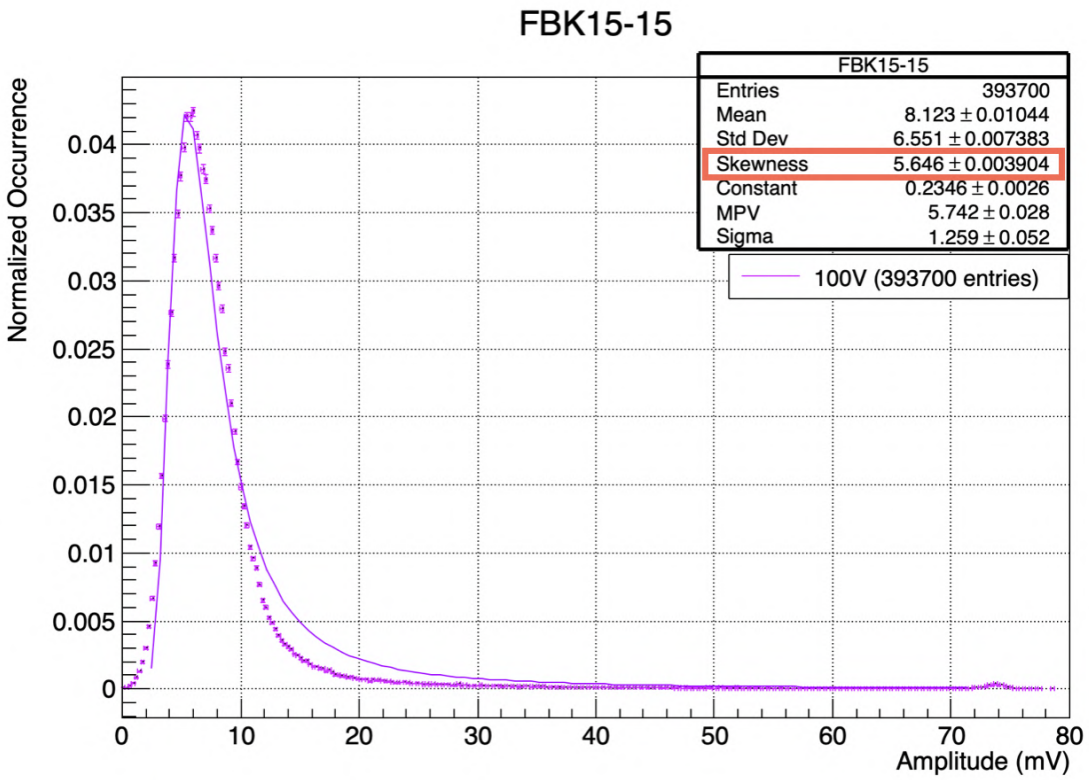

Figure 3.21: Amplitude distribution of FBK15-15 fitted with a Landau function. The label includes additional parameters considered.

3.4.1.2 Gain

The gain calculation is based on the charge calculation shown in 3.3.1.2 and considers applying a further step that helps us to understand how many charges are produced in the process, with the use, in this case, of a Landau fitting. This is done using the following equation 3.4.2, based on the assumption that the charge deposited by a particle on a sensor of the same thickness, without the gain layer (i.e., a PIN diode), is known:

$$G = \frac{Q}{Q_{PIN}} \tag{3.4.2}$$

In equation 3.4.2, Q_{PIN} represents the charge of a PIN diode. The charge of the PIN can be approximated using the formula $Q = nqd$, where n is the number of electron-hole pairs generated per micrometer (approximately 73/μm), q is the charge of an electron, and d is the sensor thickness. For this analysis, PIN charge values were extrapolated from a more complex model that accounts for various construction parameters of the sensors.

Sensors	PIN50	PIN35	PIN25	PIN20	PIN15
Charge (fC)	0.48	0.30	0.18	0.16	0.11
Sensors	**PIN100**	**PIN70**	**PIN50**	**PIN40**	**PIN30**
Charge (fC)	1.05	0.70	0.36	0.26	0.15

Table 3.6: Charge for PIN sensors with the thicknesses considered during the analysis. The first row serves as a reference for single LGAD, while the second row for the double LGAD. They are considered as constants so no uncertainty is reported.

Table 3.6 shows the results obtained from this estimation. The sensor is indicated as PIN-thickness, so PIN50 refers to a PIN diode with a thickness of 50 μm, for example, instead PIN100 is a PIN of thickness 100 μm considered to obtain the theoretical charge used to calculate the gain of as a reference for dHPK100 sensor.

Finally, regarding correlated variables such as N_{eh}, this value is calculated as before, but again fitted with a Landau distribution, in agreement with the observed data.

3.4.1.3 Root Mean Square

The root mean square (RMS) of the signal is a very important parameter for comparing the electronic noise affecting the sensor during measurements. The equation 3.4.3 shows the formula used to fill the RMS histogram:

$$RMS = \sqrt{\frac{A_N^2}{N_{points}} - \frac{A_N^2}{N_{points}^2}} \tag{3.4.3}$$

In equation 3.4.3, A_N represents the amplitude of the noise in the region preceding the signal, while N_{points} is the number of points considered. Once the histogram is obtained, the mode or mean of the distribution should be extracted. Ideally, noise should be distributed as a Gaussian; however, in real experimental conditions, this is rarely the case due to the presence of particles in regions outside the signal or secondary events, i.e., general noise. Therefore, the mode of the histogram is often relied upon.

3.4.1.4 Time Resolution with Constant Fraction Discrimination Method

In our setup we have 4 LGADs through which the charged particle passes. Therefore in general it will be appropriate to calculate the time of flight of the particle, which can be calculated as shown in equation 3.4.4. Considering that there are four planes, pairwise differences will be realised by considering all combinations without repetition:

$$\Delta t = t_i - t_j \text{ i = 1,2,3,4 and j} \neq \text{i} \tag{3.4.4}$$

The time resolution of LGADs is calculated using the Constant Fraction Discrimination (CFD) method, i.e. the time at which the signal exceeds a given percentage of the maximum amplitude is evaluated. The time distributions for each plane are obtained according to the equation 3.4.5, where b is the percentage, j the binning of the waveform's points saved on the oscilloscope. The percentages from 10% to 90% are contained in the array $CFDTh[b]$ and $fact = CFDTh[b]/100$; the time is calculated within the falling edge when $amp_{j+1} < amp_{max} \cdot fact$, where amp_{max} is the maximum amplitude within a waveform.

$$timeTh[b] = time_j + \frac{(time_{j+1} - time_j)}{(amp_{j+1} - amp_j)} \cdot (amp_{max} \cdot fact - amp_j) \tag{3.4.5}$$

The CFD method A.2.1 has the advantage that the calculated time does not require for timewalk correction (see 2.2.2.3), i.e. the correction that takes into account the shift in the time at which the signal crosses a fixed threshold due to the different signal's amplitudes. Furthermore, we expect that as the percentage on the threshold increases, the time resolution improves because the signals are larger and are less sensitive to amplitude fluctuations. In general, the distribution of arrival times as a function of the imposed CFD thresholds, shown in figure 3.22, tends to increase up to 50%, after

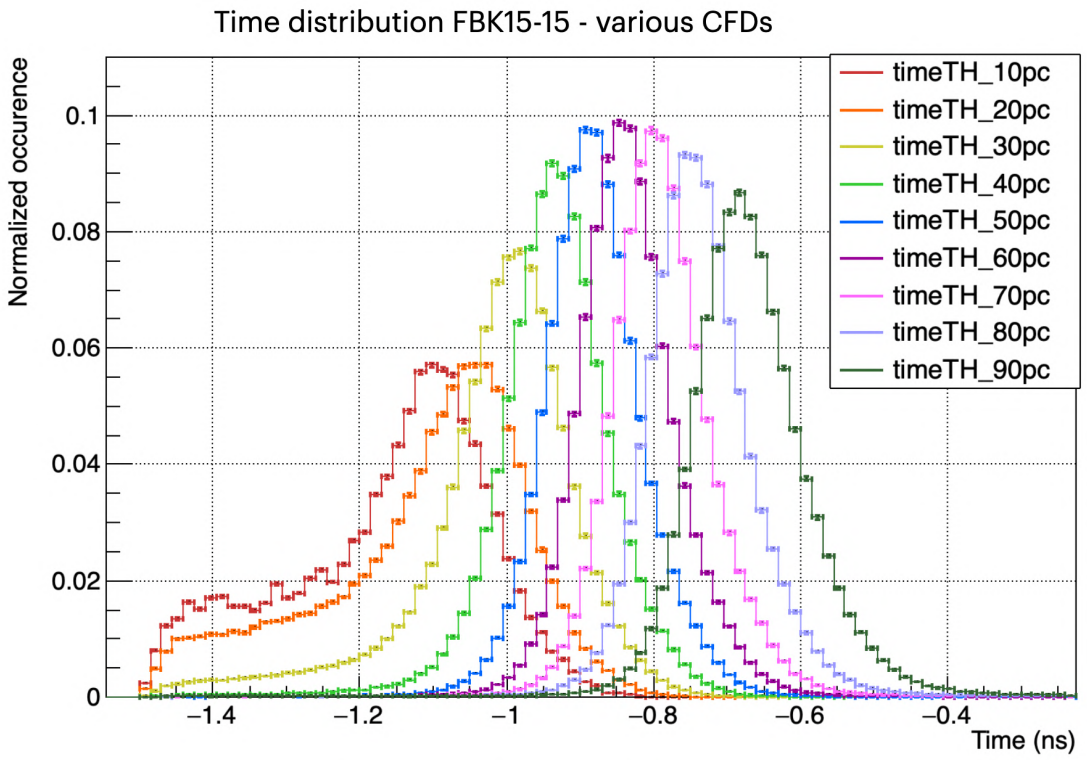

Figure 3.22: Distribution of arrival times at various CFD thresholds.

which it remains roughly constant up to 80%; in fact, often after 50%, no considerable changes in time resolution are observed.

An example of the fit procedure is shown in figure 3.23; the fit parameters are reported in the upper right box. The formula is identical to that seen in equation 3.3.2 and now reported in 3.4.6, with the difference that $p1$ now represents the resolution on time of flight σ_{ij}, $p0$ is the constant A, and $p2$ and $p3$ are those previously denoted as $q1$ and $q2$, for further details see figure 3.23.

$$f(x) = \begin{cases} p0\left[1-(1-p2)\left(\frac{1}{3-p2}\right)\frac{(x-meanPeak)^2}{p1^2}\right]^{\frac{1}{1-p2}}, & \text{if } x \leq meanPeak, \\ p0\left[1-(1-p3)\left(\frac{1}{3-p3}\right)\frac{(x-meanPeak)^2}{p1^2}\right]^{\frac{1}{1-p3}}, & \text{if } x > meanPeak. \end{cases} \tag{3.4.6}$$

Once the resolution on the time of flight σ_{ij} has been found, it is possible to to extract the time resolution of a single LGAD plane. Since we know, thanks to the operations done so far, all the possible combinations of σ_{ij}, we can now compute the time resolution of each plane, but to do so, it will be necessary to solve a system for each plane so that we can compute the time resolution of the tested sensors. So let's take as an example that we want to calculate the time resolution of plane 1 σ_1, as shown in equation 3.4.7, we will solve the system of the plane, and we will obtain 3 values, then we will average between these values, as shown in equation 3.4.8, which will give us the final result.

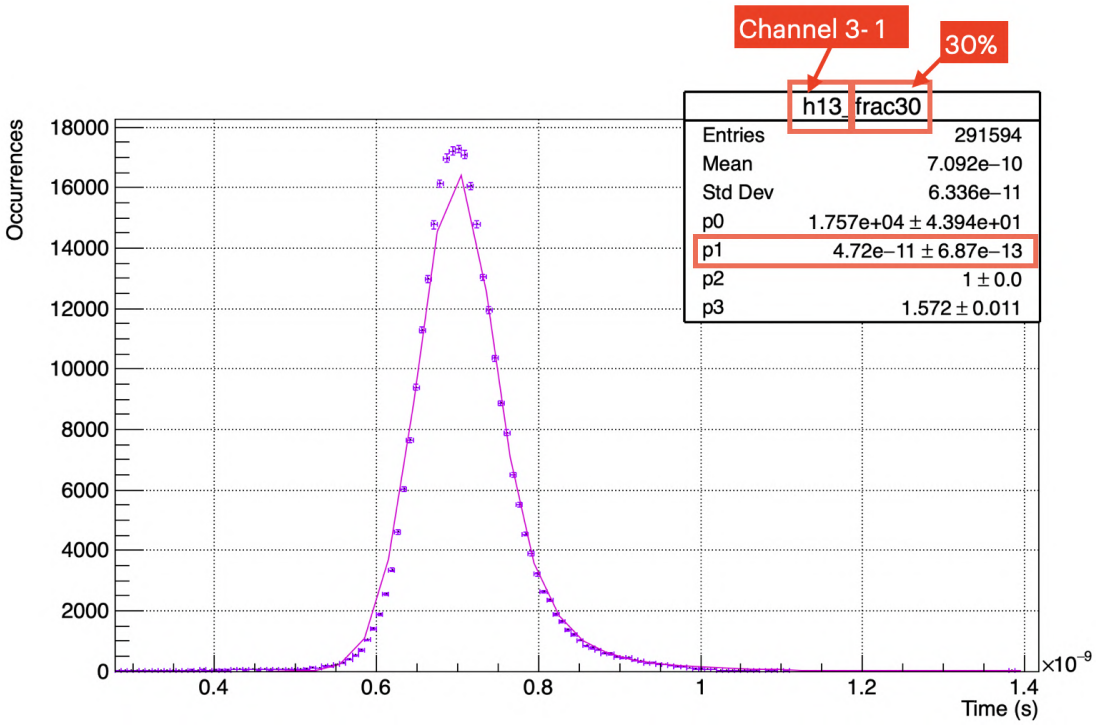

Figure 3.23: Plot of the fit to obtain in this case the resolution σ_{13} at 30% CFD for a 20 μm-thick sensor at 130 V.

$$\begin{cases} \sigma_1[1] = \sqrt{\frac{\sigma_{12}^2+\sigma_{13}^2-\sigma_{23}^2}{2}} \\ \sigma_1[2] = \sqrt{\frac{\sigma_{12}^2+\sigma_{14}^2-\sigma_{24}^2}{2}} \\ \sigma_1[3] = \sqrt{\frac{\sigma_{14}^2+\sigma_{13}^2-\sigma_{34}^2}{2}} \end{cases} \tag{3.4.7}$$

$$\sigma_1 = \frac{\sigma_1[1] + \sigma_2[2] + \sigma_3[3]}{3} \tag{3.4.8}$$

What has been said so far is only true if the time resolution of the reference sensor is not known. If the latter were known, the time resolution of the plane to be tested would be much easier to calculate because in this case it would only be necessary to determine σ_{1j} where j represents the 2-3-4 plane. Once this result has been found, it would be sufficient to subtract the reference in quadrature to obtain the resolution of the plane. Below we show the time resolution of a sensor as a function of the CFD threshold 3.24a-3.24b.

At low CFDs, time resolution values are unreliable as expected. This happens because at low CFD you have a higher jitter contribution, which is directly proportional to the noise and inversely proportional to the signal slope. Since the signal slope is lower at low CFD, jitter increases and consequently resolution worsens. At higher CFD values, the time resolution on the other hand is dominated by the Landau term, because you have the non-uniform creation of e-h pairs along the particle path. this should be seen more in the thick and less in the thin sensors. However, between these two regions, there is a zone where an improvement in time resolution can be observed, which remains stable up to about 80% of the CFD threshold. This represents the ideal CFD threshold region to apply to our sensor. This observation has general validity and is especially relevant for thicker sensors where Landau fluctuations are more pronounced.

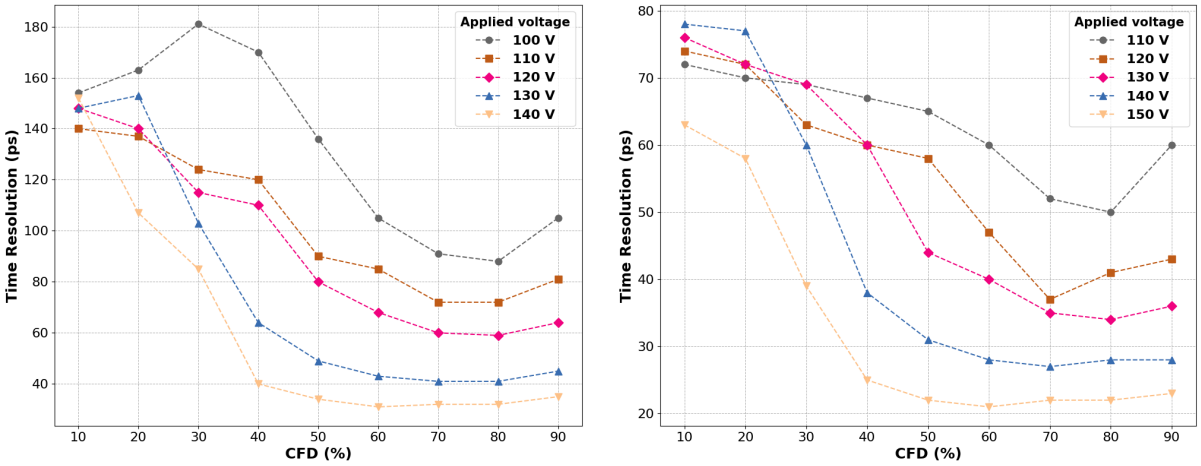

(a) (b)

Figure 3.24: (a)Time resolution of FBK15-15 as a function of CFD threshold for different voltages. (b) Time resolution of FBK20-18 as a function of CFD threshold for different voltages.

3.4.2 Preliminary analysis on dLGAD

In this paragraph, the results for a 15 μm sensor are presented, specifically comparing the two single boards and the module. This sensor is shown as a representative example of the dLGAD concept. Figures 3.25a and 3.25b illustrate that, despite the increased complexity of the circuit, the RMS value (figure 3.25a) does not change significantly in the dLGAD module. On the contrary, the module seems to provide better results compared to one of the single boards, which is very positive, especially considering the S/N ratio shown in figure 3.25b. Here, a significant improvement in the S/N ratio is observed, ranging from approximately 40% to 50% depending on the voltage. This is consistent with the fact that a greater signal is sent at the amplifier's input.

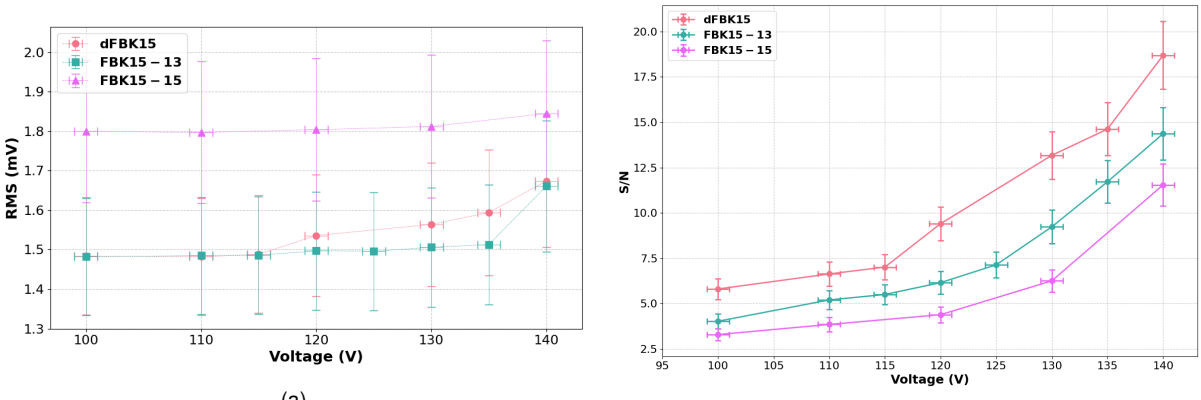

(a) (b)

Figure 3.25: (a) Plot of the average RMS for the sensors composing the double LGAD sensor, used for comparison at various voltages. (b) Plot of the MPV of the S/N for the sensors composing the double LGAD sensor, used for comparison at various voltages.

Figure 3.26 show the number of N_{eh} pairs as a function of voltage compared between the sensors comprising the dLGAD and the dLGAD itself. The number of N_{eh} pairs is another way to express the deposited charge, as it is directly related to it by equation 3.3.5. Doubling the thickness of the sensor results in a systematic increasing of approximately 45% in the number of created pairs and thus in the charge deposited.

Finally, table 3.7 lists the calculated gain factors for all sensors and compares them

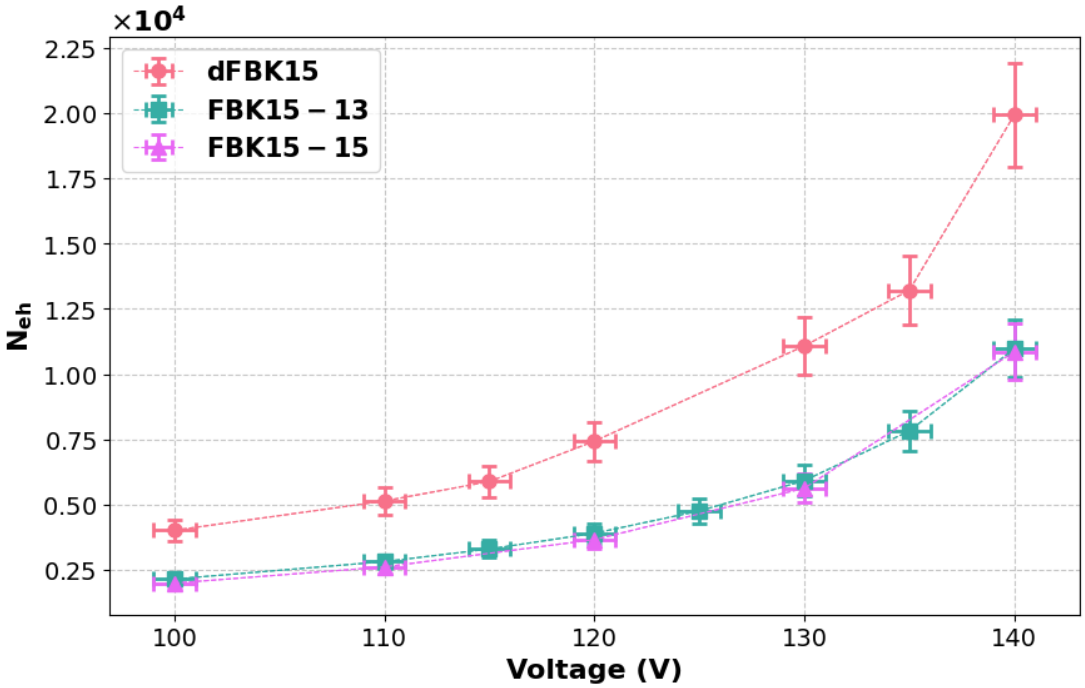

Figure 3.26: Comparison of the MPV of N_{eh} pairs among single sensors and the the double LGAD composed by them.

with the values of the individual sensors. It also includes a column showing the deposited charge for these sensors. Note that a range is reported in this case: the first value represents the measurement at the lowest voltage, while the last value corresponds to the highest voltage. Overall, these results are in line with our previous observations.

Sensors	*Voltage (V)*	*Gain*	*Charge (fC)*
FBK20-15	(110 ±1) (150 ±1)	(9 ±1) (35 ±3)	(1.4 ±0.1) (5.6 ±0.5)
FBK20-18	(110 ±1) (150 ±1)	(8 ±1) (30 ±3)	(1.3 ±0.1) (4.8 ±0.5)
dFBK20	(110 ±1) (150 ±1)	(11 ±1) (59 ±6)	(2.9 ±0.3) (15 ±1)
FBK15-15	(100 ±1) (140 ±1)	(6 ±1) (31 ±3)	(0.7 ±0.1) (3.4 ±0.3)
FBK15-13	(100 ±1) (140 ±1)	(6 ±1) (32 ±3)	(0.7 ±0.1) (3.5 ±0.1)
dFBK15	(100 ±1) (140 ±1)	(9 ±1) (43 ±4)	(0.7 ±0.1) (6.5 ±0.6)

Table 3.7: Table showing charge and gain of the sensors composing the double LGAD module, used for comparison at the first and last considered voltages.

3.4.3 Study of peak resolution

This section presents the peak resolution study, divided into two subsections. First, we will show a brief comparison between the results obtained from the double LGAD module and the individual LGAD sensors that compose it. The subsequent subsection

will explore the comparison between sensors of the two different thicknesses, focusing on double LGAD sensors (3.4.3.2). Finally, a table (3.8) will summarize the peak resolution results for sensors of various thicknesses, comparing the double LGAD concept with its individual components.

3.4.3.1 Comparison between sLGADs and dLGAD

In this subsection, plots for the 15 μm sensors that make up the dLGAD module are presented and compared with the module itself. It is important to note that, unlike with the photon source, we were able to investigate a much wider region due to the higher signal (as shown in previous figures, with the 15 μm sample used throughout). Therefore, the 15 μm sensors provide a valid sample for conducting these studies under different physical conditions. Results from other sensors, as will be shown later, are significantly better.

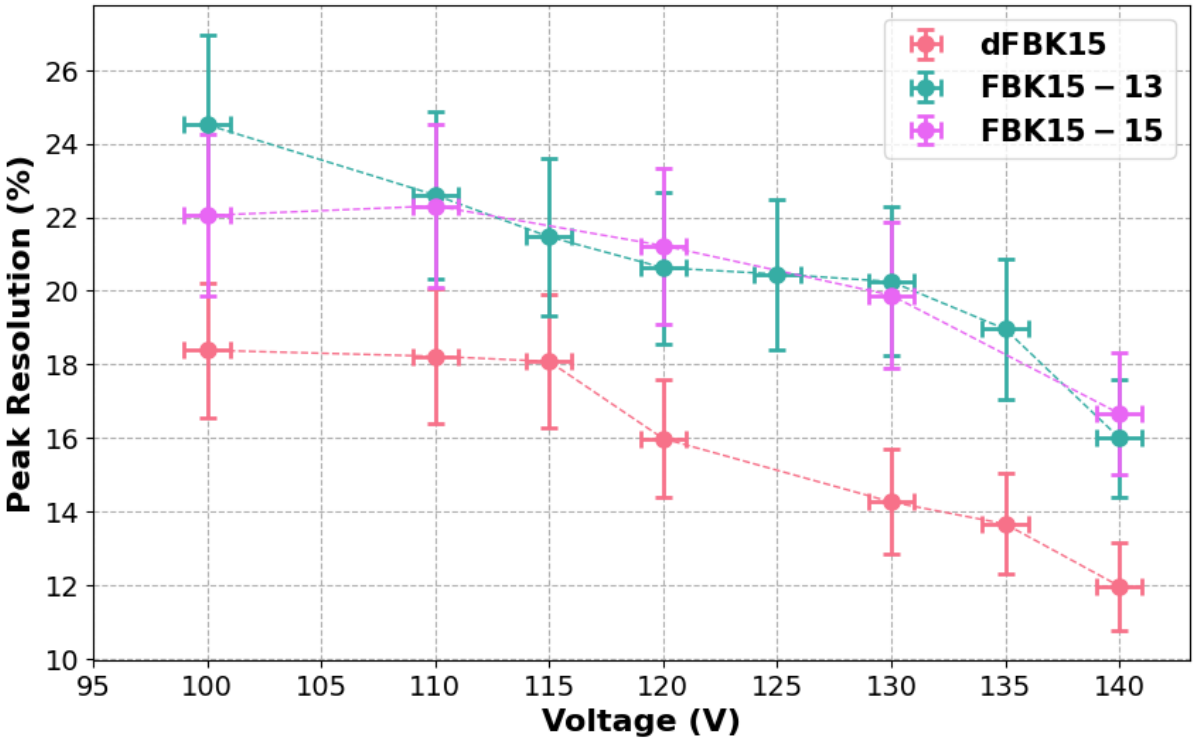

Figure 3.27: Plot of the peak resolution for the sensors composing the double LGAD sensor, used for comparison as a function of voltage.

Figure 3.27 shows that the dLGAD module exhibits an improvement in peak resolution, consistent with the expectation that the signal is of the same steep as that of a thin sensor (15 μm in this case), but with twice the amplitude, which would yield better results. These improvements range from approximately 4% to 7%, in agreement with figure 3.26, where the number of N_{eh} pairs increases significantly. While these performance improvements are modest compared to expectations, it is important to note that these sensors remain relatively small in thickness.

3.4.3.2 Comparison among dLGADs

This section provides an in-depth comparison between different dLGAD sensors and presents the results for comparative analysis. As shown in figure 3.28a, it can be

observed that passing from a double of 15+15 μm to a double of 20+20 μm, there is a marked improvement in the results in nearly a 1.5% better peak resolution. This is also consistent with an increase in the number of pairs, as illustrated in figure 3.28b, showing an average improvement of about 48% at similar gains. Furthermore, one can also look at the S/N for these two sensors, and in any case what one observes is that dFBK15 reaches a maximum of 20 (see figure 3.25b), while dFBK20 even reaches 30 (see figure D.1b).

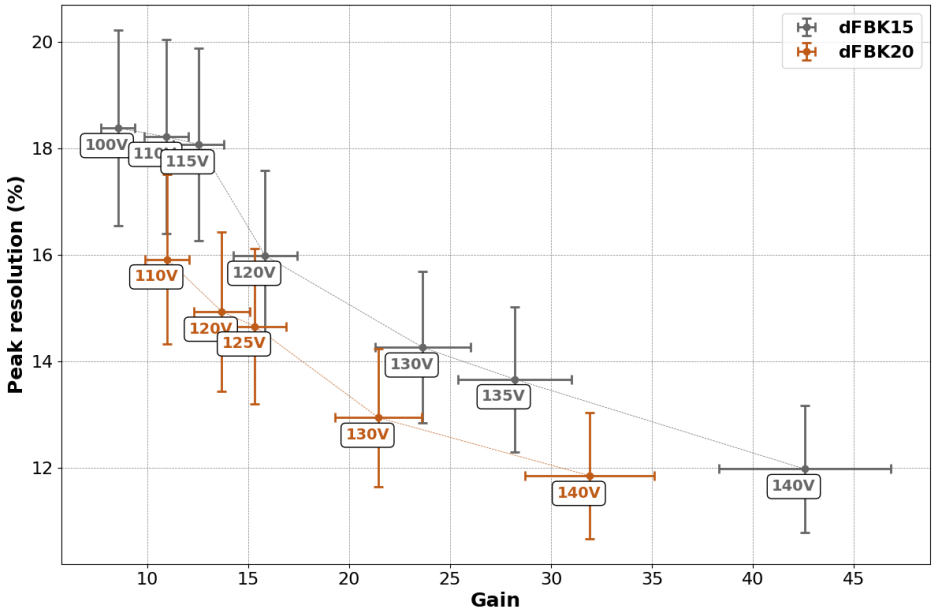

(a)

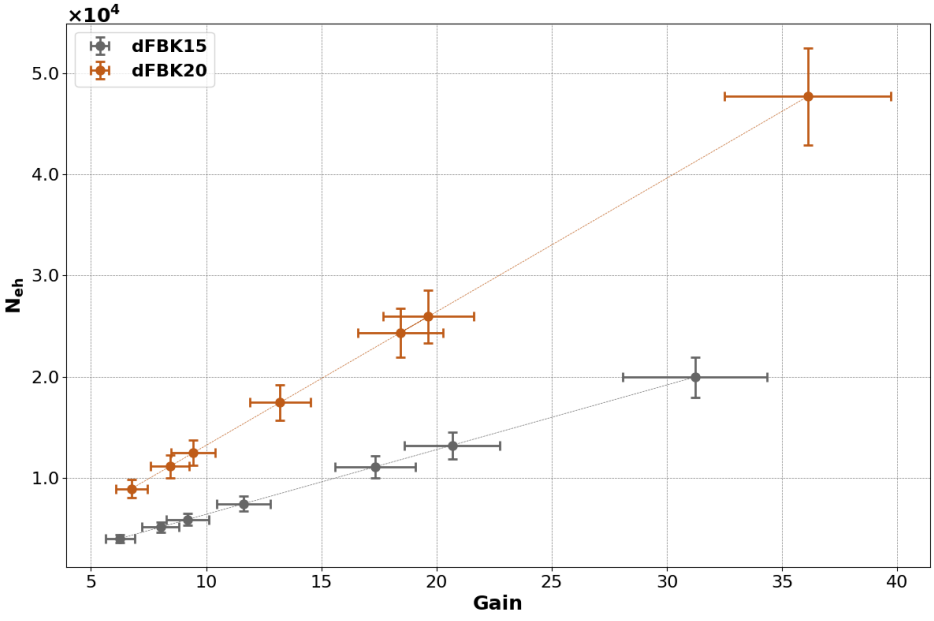

(b)

Figure 3.28: (a) Plot of peak resolution for dLGAD sensors with thicknesses of 15+15 and 20+20 μm as a function of gain. (b) Plot of N_{eh} as a function of gain for different thicknesses, 15 and 20 μm.

3.4.4 Study of time resolution

In this section, the results of the time resolutions obtained on the 15 and 20 μm sensors calculated as reported in the 3.4.1.4 section are discussed. The trend of the time resolutions was first be analysed as a function of the CFD percentage (from graphs like the one in the figure 3.29) and then, once the percentage is fixed (usually around 40-50-60%), the values obtained for the single LGADs will be compared with the respective dLGADs as the voltage changes (paragraph 3.4.4.1). It is important to emphasise that such thin sensors are not optimal for time resolution analysis due to the small signals. In fact, these sensors are characterised by a low signal to noise ratio, which is compounded by the fact that the higher gain introduces additional fluctuations in the avalanche process that lower the fluctuations in amplitudes and worsen performance. Finally, a comparison between the double sensors dFBK20 and dFBK15 is presented in paragraph 3.4.4.2.

3.4.4.1 Comparison between sLGADs and dLGAD

In general, dLGADs show better time resolutions than single sensors; the comparison is shown in figure and in figure 3.29 for the 20 μm sensor, where the double LGAD is compared with the single front and back sensors.

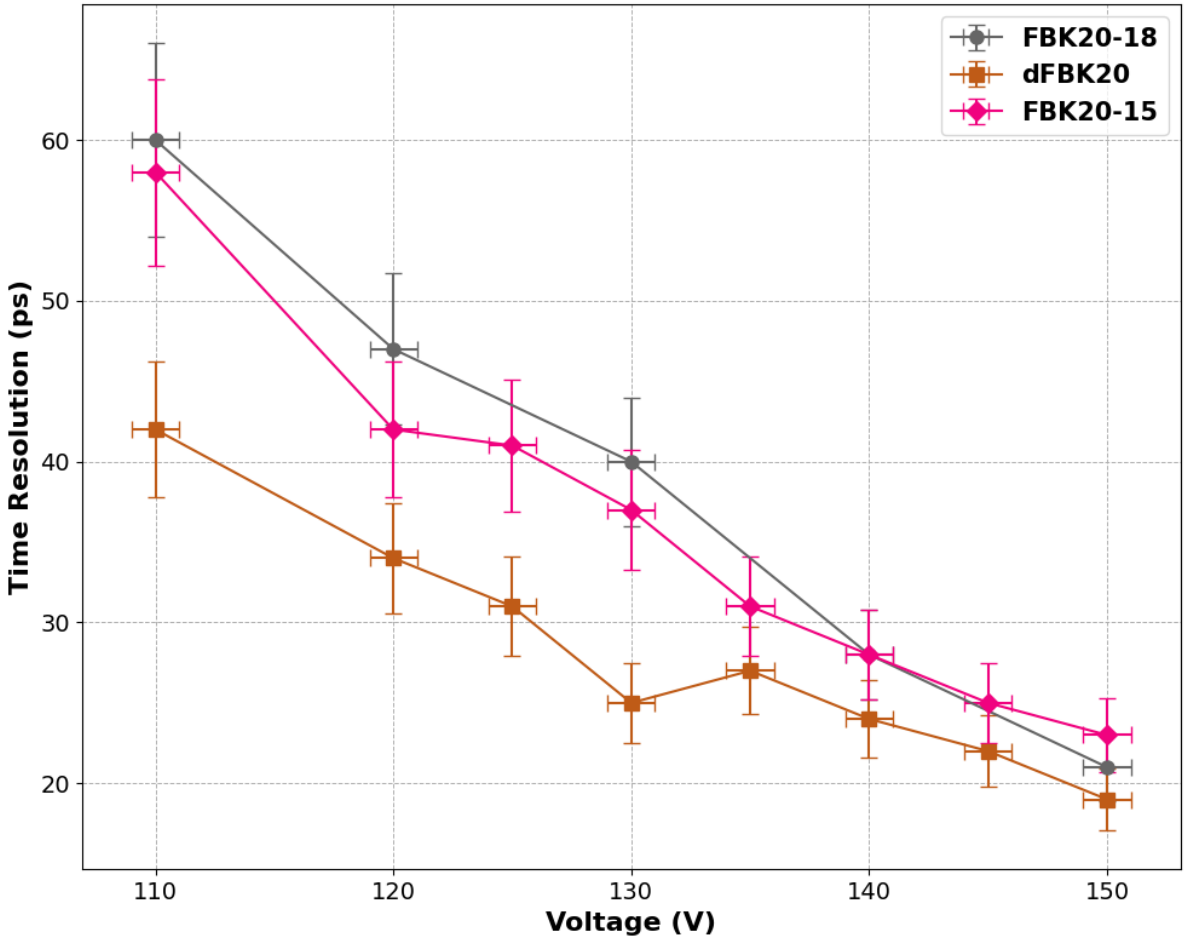

Figure 3.29: Distribution of time resolutions as a function of voltage for single 20 μm and double sensors of thickness 20+20 μm.

The improvement in time resolution is evident especially at high voltages where the time performance of the double sensor drops below 20 ps. The concept of ultra-thin

devices to achieve resolutions around 20 ps, as required by the experiment ALICE 3 works, and the double LGAD improves performance considerably by achieving results below 20 ps.

The signal improvement, however, deviates from being $\sqrt{2}$ and this is simply due to the fact that the signal is not identical and subject to fluctuations between the two sensors that make up the double. However, the concept of dLGAD in fact allows for a larger signal with a common amplification: the electronic noise therefore does not increase (see figure 3.25a), but the signal-to-noise ratio does (see figure 3.25b). This is why the improvement is particularly evident for the thicker dLGAD, as the resulting signal is broader. What can be observed in the graph 3.29 is an improvement in resolution ranging from about 30% at low voltages to about 20% at high voltages.

3.4.4.2 Comparison among dLGADs

The two dLGADs are compared by studying time resolution as a function of gain (figure 3.30) at a fixed CFD threshold of 60%: as expected, time resolution improves with increasing gain as the signal amplitude increases; this is particularly evident for the 20+20 μm sensor.

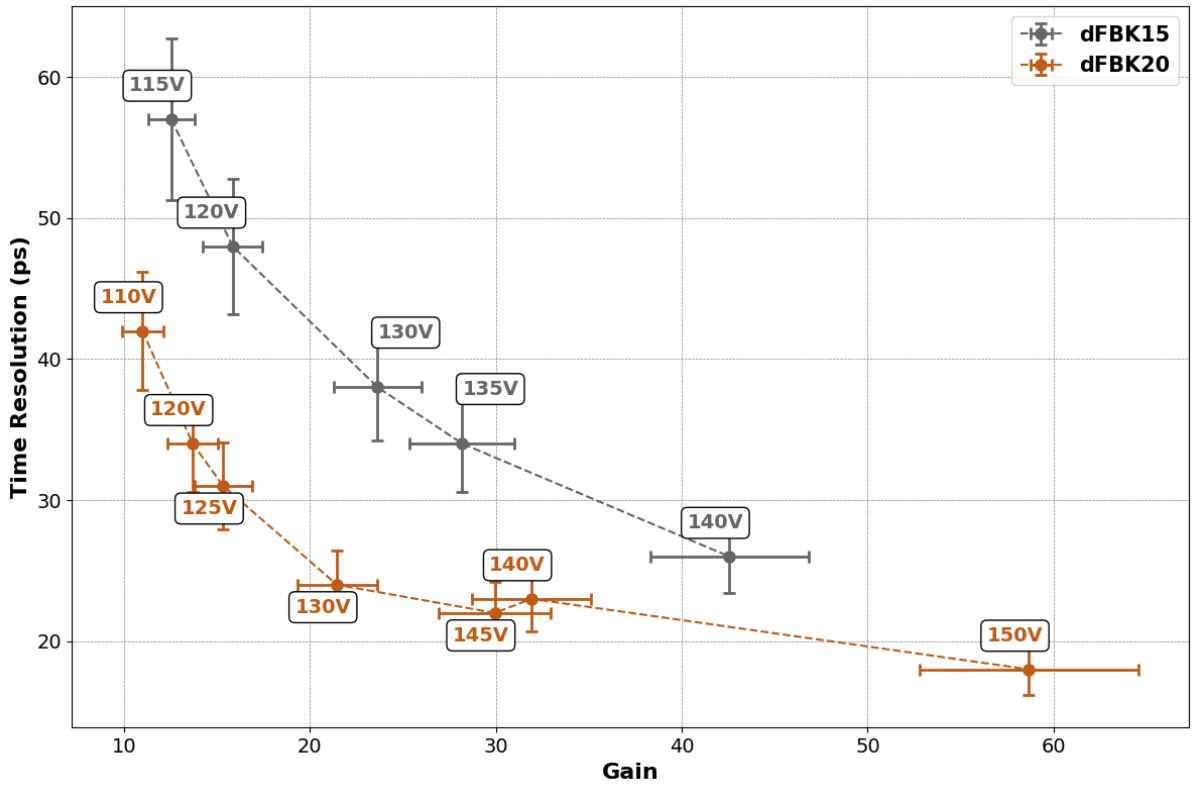

Figure 3.30: The two dLGADs composed by two 15μm and 20 μm sensors are compared in the plot, showing the trend in time resolution as a function of gain.

It is important to emphasise that the 20+20 μm sensors have higher breakdown values and can therefore be studied over an extended voltage range, thus also achieving higher gains. In general, the time resolution seems to benefit from reduced thickness and also from the double concept; there is more pairs produce by the avalanche process in dFBK20, which increases the signals and improves the resolutions (3.28b) respect to a dFBK15 sensors. The improvement in time resolution ranges from around 40 to 16% for similar gains as the applied voltage increases, so the thinner sensor still

seems to provide good results for high potentials where the electric field is stronger. However, the dFBK20 sensor manages to provide results close to 20 ps. The difference between the two sensors, however, remains compatible with what is observed in 3.28b.

3.4.5 Final Results

Table 3.8 below presents the final results obtained comparing dLGADs, including the peak resolution and time resolution for each thickness. In the previous sections, only a few results and no direct comparisons between single sensors or for the FBK20 double-single sensors were shown. For the sake of completeness, these results will be shown in the appendix, see D.1. In addition, time resolution and peak resolution results for single sensors are shown in table D.1.

Sensors	Voltage	R (%)	σ(ps)	Sensors	Voltage	R (%)	σ(ps)
dFBK15	100V	18.9	(77 $\pm$8)	dFBK20	110V	15.9	(42 $\pm$4)
	110V	18.2	(64 $\pm$6)		120V	14.9	(34 $\pm$3)
	115V	18.0	(57 $\pm$6)		125V	14.7	(31 $\pm$3)
	120V	15.9	(48 $\pm$5)		130V	12.9	(25 $\pm$3)
	130V	14.3	(38 $\pm$4)		140V	11.8	(24 $\pm$2)
	135V	13.6	(34 $\pm$3)		145V	12.2	(22 $\pm$2)
	140V	11.9	(26 $\pm$3)		150V	9.7	(19 $\pm$2)

Table 3.8: Table showing peak resolution results for each voltage, comparing the individual dLGAD sensors. The uncertainty on R is not reported but is considered 10% of the ratio σ/MPV not in percentages.

Finally, for the sake of completeness, the S/N and N_{eh} values for dFBK20 and dFBK15 obtained for various voltages are also given in table 3.9.

Sensor	Voltage (V)	N_{eh}	S/N	Sensor	Voltage (V)	N_{eh}	S/N
dFBK15	100	4006	6	dFBK20	110	8931	12
	110	5130	7		120	11126	15
	120	7426	9		130	17431	17
	130	11082	13		140	25932	25
	140	19951	19		150	47673	32

Table 3.9: Results of N_{eh} and S/N for the bias applied in dFBK15 and dFBK20. The uncertainty to be associated with the result is 10% in accordance with what was discussed above.

Conclusion

In this thesis work, Low-Gain Avalanche Diodes (LGADs) sensors were analyzed and characterized for the Time-of-Flight (TOF) system of the future ALICE 3 experiment. Specifically, the TOF layer is expected to be based on ultra-thin silicon devices with a time resolution better than 20 ps. The study of these sensors includes the characterization of ultra-thin prototypes with thicknesses of 35, 25, 20, and 15 μm produced by FBK.

The presence of a highly doped layer, called gain layer, beneath the collection electrode, enables charge multiplication and the extremely thin structure allows for a good gain without reaching the breakdown point, i.e., the point beyond which the reverse current increases rapidly. This configuration prevents the multiplication of holes, which have low mobility, ensuring that the signal is only due to electron avalanche. The fast movement of the charge makes these devices highly suitable for timing applications. Additionally, due to the reduced gain, they do not require a quenching resistor, which improves the fall time and reduces the sensors dead time after the passage of particles.

Recent studies have also explored the development of double LGADs, where two sensors are implanted on either side of a specially designed Printed Circuit Board (PCB), allowing the two signals to be summed and sent to a single common amplifier. This innovative design leverages the better time resolution of thin LGADs while increasing the charge delivered to the input electronics.

The thesis work includes a study of both energy and time resolution with photons in the laboratory and with charged particles at CERN's T10 beam facility. In particular, we examined the response of these sensors to the passage of photons emitted by an ^{55}Fe source, which emits in the X-ray range (5.9 keV - 6.5 keV). By using the charge deposited by electrons produced by photon interactions as a reference metric, we compared the sensors' response. As expected, a single peak was observed, corresponding to the photon interaction. This allowed us to extract the peak resolution, as it was not possible to distinguish the two expected energy peaks.

We compared sensors of various thicknesses at the same deposited charge level, and it was found that these ultra-thin sensors are not suitable for such small signals, as their performance was worse than the reference sensor (50 μm). Notably, the 20 μm and 15 μm sensors showed particularly noisy and unreliable signals, often mixed with noise. On the other hand, the 35 μm and 25 μm sensors confirmed the expected decrease in performance as the signal-to-noise ratio (S/N) gets lower with the deposited particle signal.

We then conducted similar studies using charged particles with 15 μm and 20 μm sensors, obtaining different results regarding the peak resolution. Unlike the study with the ^{55}Fe source, in this case, we observed an improvement in resolution as the voltage increased. This is related to the physical process by which a charged particle (in this case, a MIP) generates a larger signal (73 e-h/μm) compared to a photon, resulting in larger signal amplitudes overall. In this case, it was possible to calculate the gain and use it as a comparison metric between the two sensors. Moreover, we successfully

exploited the double LGAD concept in this study, recording even better performance thanks to its structure.

Finally, we also performed timing resolution studies with these ultra-thin prototypes, confirming their excellent timing performance, compared to the 30 ps achieved by standard 50 μm-thick LGADs. In this case, also time resolution below the target 20 ps were measured. Notably, the timing resolution appears to benefit from the double LGAD concept, as observed in previous studies with 35+35 μm and 25+25 μm sensors.

Appendix A

Timing: more on technique and correction

A.1 Time-of-flight

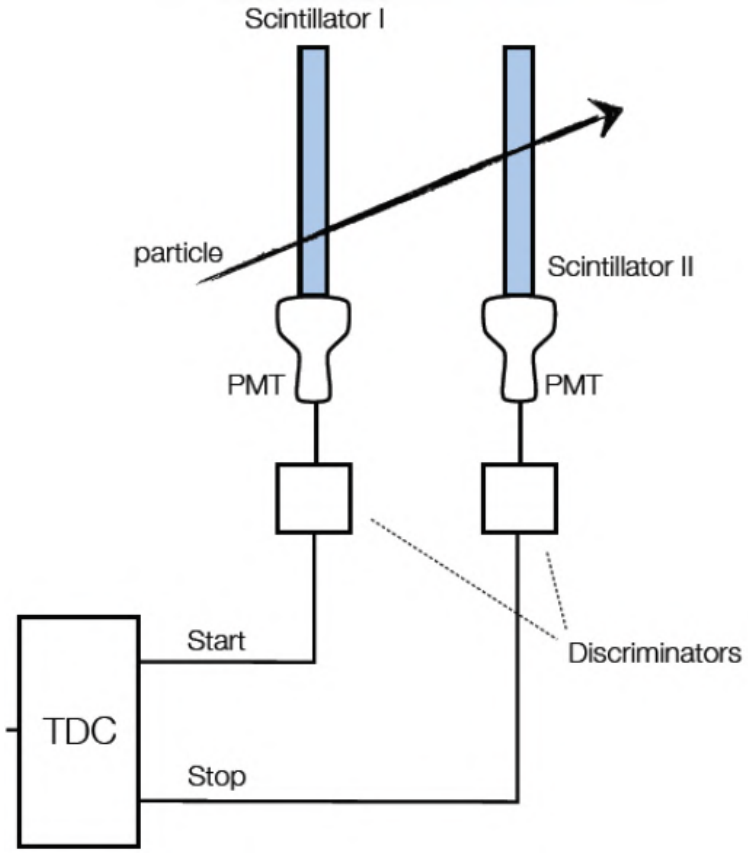

Figure A.1: Working principle of TOF, it is based on a system scintillator photomultiplier tubes (PMTs) coupled with a discriminator and followed by a TDC.

The Time-of-Flight (TOF) technique is a powerful method used in particle physics experiments to determine the velocity of particles by measuring the time difference between signals detected at two points along their path. This time difference, denoted as Δt, is directly related to the spatial distance between the detectors (L) and the ratio of the velocity of the particle to the speed of light (c), represented by the symbol β. The

relationship is encapsulated in equation A.1.1:

$$\Delta t = t_{stop} - t_{start} = \frac{L}{c\beta} \tag{A.1.1}$$

In figure A.1, we illustrate the fundamental working principle of TOF. It relies on a setup comprising scintillator materials coupled with photomultiplier tubes (PMTs), followed by a discriminator and a Time-to-Digital Converter (TDC) to precisely measure the time difference between signals.

Now, to differentiate between particles of different masses but the same momentum using TOF, we employ equation A.1.2, under the assumption of relativistic particle behavior:

$$\Delta t = \frac{Lc}{2p^2}(m_1^2 - m_2^2) \tag{A.1.2}$$

Here, m_1 and m_2 represent the masses of the two particles being compared, and p denotes their momentum. Notably, the separation in time between particles decreases markedly as momentum increases, as depicted in figure A.2. This underscores the importance of considering the interplay between momentum, mass, and time resolution (expressed in picoseconds) in achieving effective particle discrimination.

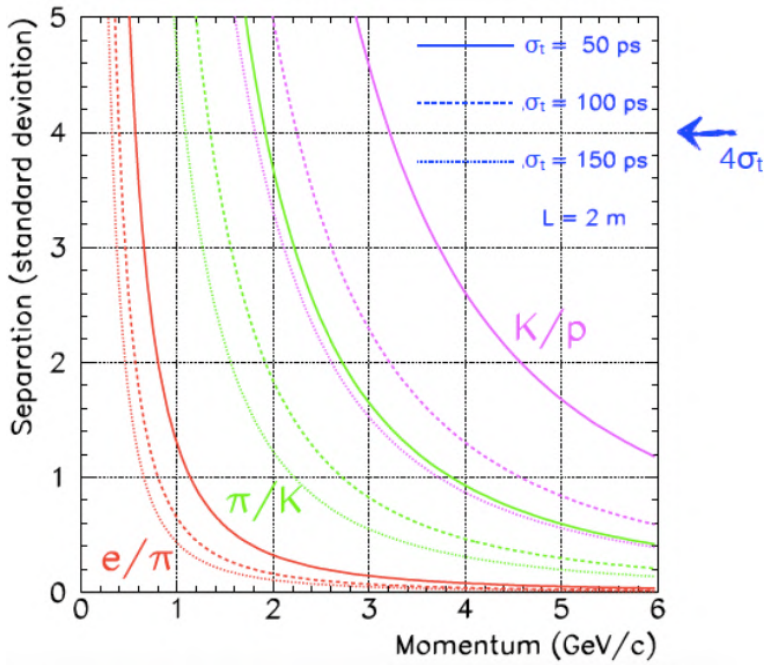

Figure A.2: Discrimination among particles as a function of momentum for several time resolution (50,100,150 ps).

By leveraging TOF measurements alongside other particle identification techniques, researchers can disentangle complex mixtures of particles, contributing significantly to our understanding of fundamental particle properties and the dynamics of particle interactions in high-energy physics experiments.

A.2 TimeWalk correction

The variability of the energy deposition by impinging particles creates two distinct effects: amplitude fluctuations, and shape irregularities.

The post-preamplifier discriminator is set to prevent false triggers by using a threshold approximately 4-5 times higher than the noise level. This introduces sensitivity to Landau amplitude variations as varying pulse amplitudes cross the threshold at different times, with large pulses being detected earlier than small ones. To correct this issue, two common solutions are Constant Fraction Discrimination (CFD) and Time-over-Threshold (ToT), as illustrated in figure A.3. Multiple Samplings (MS) is a third option that offers higher performance. However, it requires full signal digitization, which limits its use to systems with fewer pixels due to computing power demands.

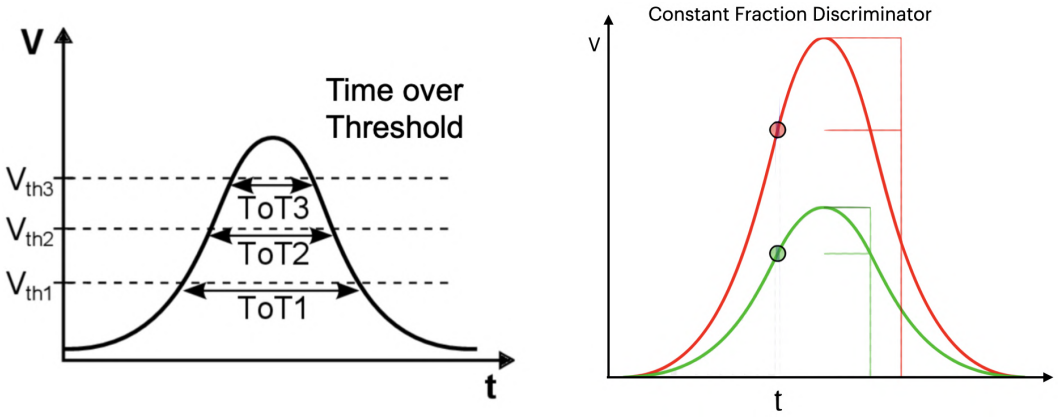

Figure A.3: Representation of the two methods to correct time-walk effect (right) Constant Fraction and (left) Time over Threshold.

A.2.1 Constant Fraction Discriminator (CFD)

is a method used to determine particle arrival time (t_1) based on when the pulse reaches a specific fraction of the maximum amplitude V_{Max}. This method focuses on the rising part of the pulse and provides quick information without the need for extra corrections.

The main objective is to measure the time (t_1) at which the pulse reaches a specific fraction ($f = \frac{V(t)}{V_{Max}}$) of its maximum height. This method eliminates the dependence on the actual height of the pulse and instead focuses on when it reaches a certain proportion of its maximum height.

A.2.2 Time-over-Threshold (ToT)

ToT involves assessing the particle's arrival time (t_{ToT}) using two time points: the initial time point (t_1) and a later time point (t_2). The correction applied is based on the duration of time the preamplifier signal remains above the predetermined threshold, calculated as (t_2-t_1). To refine the timing information, the ToT value is then used to adjust t_1 using a formula optimized for the specific electronics of the system. To implement this strategy, additional logic such as an FPGA is incorporated. The correction is computed after measuring and recording both t_1 and (t_2-t_1). Unlike Constant Fraction Discrimination (CFD), the Time-over-Threshold technique requires accurate measurement of both the rising and falling edges of the signal.

The effectiveness of CFD and ToT varies depending on the type of amplifier used, specifically the Charge Sensitive Amplifier (CSA) and Broad-Band Amplifiers (BBA). CSA allows for both techniques due to its ability to shape the input signal differently,

while CFD is more sensitive with BBA due to the almost constant output signal width, making ToT application challenging.

CFD is particularly effective in terms of pulse scaling accuracy, making it suitable for Ultra-Fast sensors with well-defined peak times. Combining methods to measure sensor time quickly, followed by careful correction and validation, is attractive. However, it necessitates additional circuitry. This is particularly true for CFD, which requires an arming discriminator to ensure a sufficiently large pulse, adding to the complexity.

A.3 Excess noise factor

The excess noise factor (F) resulting from the multiplication mechanism in a gain layer. Each unit charge entering the amplification layer generates, on average, a number of charges equal to the amplification (G). However, individual charges can introduce additional noise, referred to as the excess noise factor. This noise, expressed as F, affects the signal-to-noise ratio (SNR) after multiplication. Figure A.4 shows the simulated excess noise factor for LGAD detectors.

The excess noise factor (F) is often defined in terms of the gain (G) and the ratio (k = α/β), where α and β are the hole and electron ionisation rates respectively. The formula is:

$$F \simeq G^x = Gk + (2 - \frac{1}{G})(1 - k) \tag{A.3.1}$$

In equation A.3.1 x is referred to be the excess noise index. A key insight from equation A.3.1 is that achieving low noise gain requires low gain coupled with a minimal hole ionisation rate. The electric field should only promote electron multiplication.

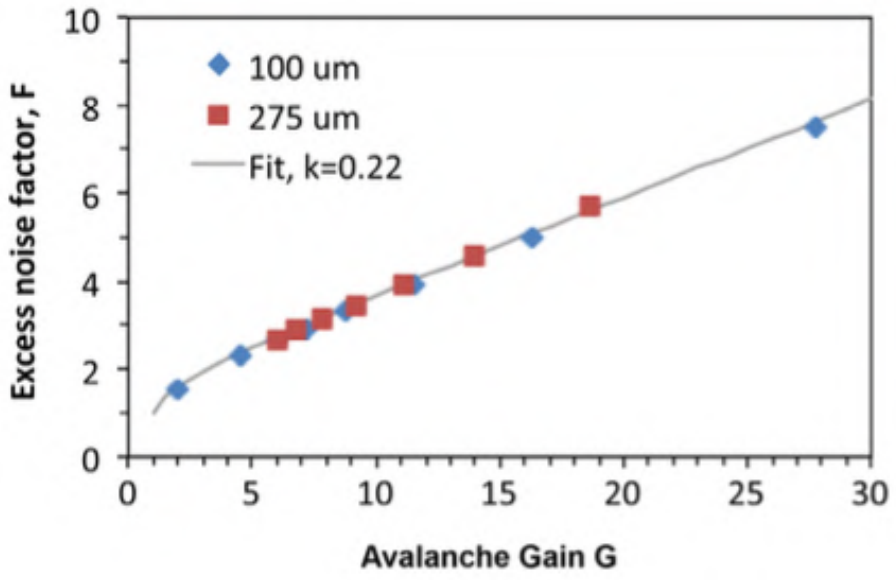

Figure A.4: Excess noise factor as a function of gain.

Appendix B

Details about characterization of LGAD sensors

B.1 Introduction to FBK LGADs and Sensors

The sensors produced by FBK are shown in figure B.1, where their bonding process is depicted. We have two types of sensors: the FBK25-35 sensors which are constructed with an LGAD-PIN structure, where one pad is an LGAD and the other is a PIN. Referring to figure B.1, the LGAD (left pad) and PIN (right pad) each have an area of 1x1 mm^2. Both are surrounded by a Bias Ring and four concentric Guard Rings (GR) relative to the Bias Strip (BS). In the zoom of FBK20/15, the sensor structure is clearly visible, consisting of a central pad, the outermost GR, and three windows on the metal surface. Here the area is 1.3 x 1.3 mm^2.

The bare LGAD sensor (see photo B.1) needs to be bonded to the board first. For this purpose, a specialized bonding machine can be used, as shown in figure B.1. Finally, at the bottom left, a zoom of the reference sensor, HPK50, is shown. The purpose of the bonding process is to connect an Au/Ag wire to the capacitor from the active area of the LGAD, while connecting the GR to the Ground.

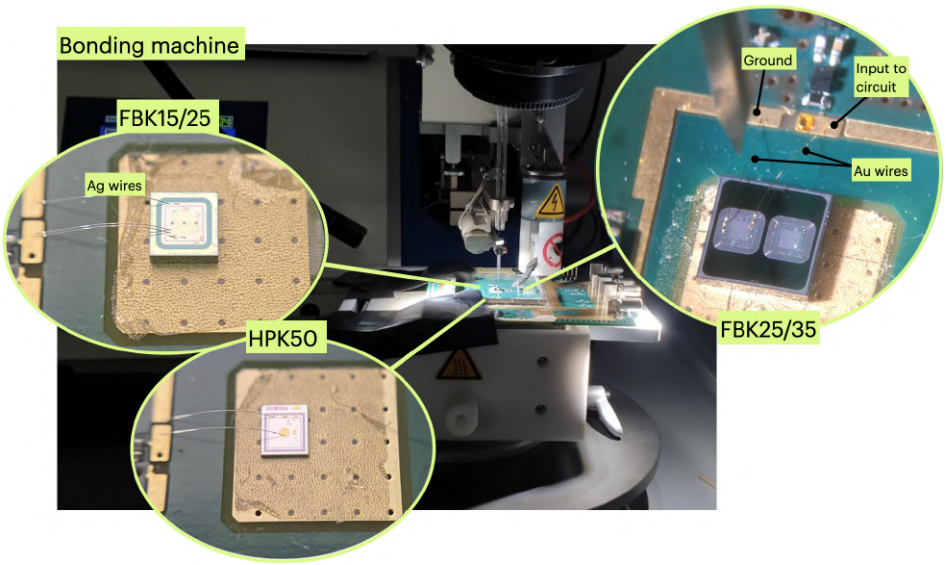

Figure B.1: Photo of the bonding machine and a microscope zoom showing the bonding with Au wires.

The amplifier is a Darlington configuration with emitter degeneration. This configuration uses two transistors connected in cascade, where the second transistor amplifies

the signal already amplified by the first. Each transistor has an emitter resistor, which provides emitter degeneration, helping to stabilize and linearize the amplification.

You can also think of the circuit as a cascade of two stages with emitter degeneration. Each stage has a resistor connected to the emitter, which introduces feedback that reduces the overall gain but improves stability and linearity.

The forward stage (the main amplifying stage) is subject to feedback. This feedback is created using a voltage divider between two resistors: one connected between the collector and the base of the transistor, and another between the base and ground. This feedback helps control and stabilize the gain, as well as reduce distortion.

The voltage gain of the amplifier is approximately determined by the ratio between the feedback resistor (collector-base) and the input resistor to ground (emitter-ground). In simpler terms, the gain of the circuit depends on the relationship between these two resistances.

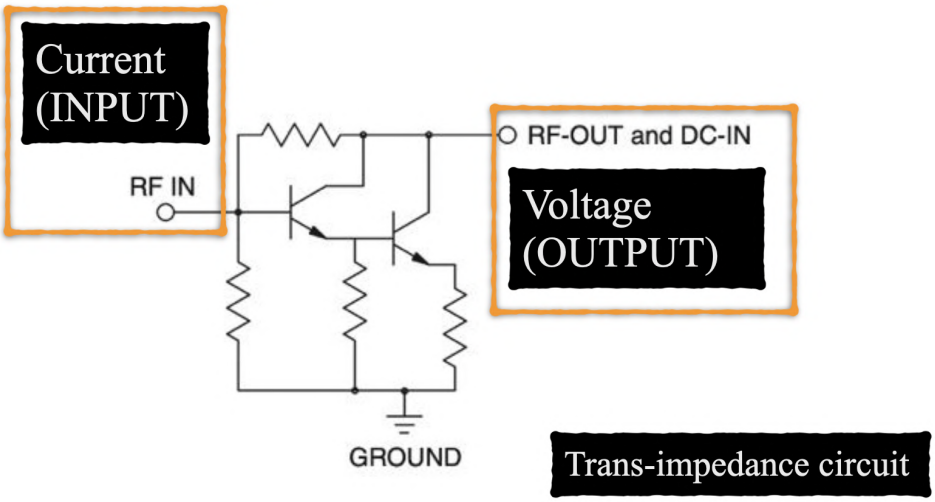

Figure B.2: Circuit mounted on the PCB for the LGAD transimpedance amplifier.

The sensor is mounted on this PCB which acts as a transimpedance amplifier with a resistance of 470Ω. As shown in figure B.3, three channels are primarily used. Considering that the sensor provides a "front" view, the first channel is used to power the circuit on the PCB, the fifth channel is for powering the LGAD sensor, and the third channel is the output taken from the measurements and sent to the amplifier.

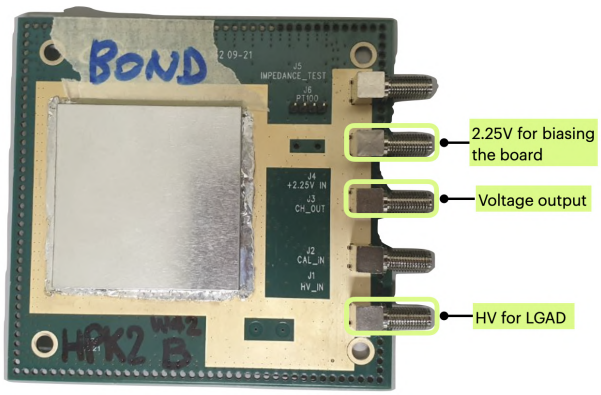

Figure B.3: PCB of an LGAD HPK50 with highlighted channels used for measurements.

When performing the IV characterization, unlike the time and energy resolution measurements, we will not use the fifth channel to power the sensor. Instead, the

2.25V power supply will not be used for the PCB, so the output (the third channel) will deliver a current that will be measured with the ammeter (see figure 3.5).

B.2 Breakdown Voltage Extraction Methods

As mentioned, one of the objectives of the measurement is to extract the breakdown voltage value from the IV characteristics of the samples. In this case, the breakdown voltage for each sensor was obtained graphically through three different methods, implemented using ROOT:

- **Logarithmic Derivative (LD)**;
- **Inverse Logarithmic Derivative (ILD)**;
- **Line Intersection Method**.

The logarithmic derivative involves calculating the algebraic derivative of the logarithm of the current, and is defined as follows:

$$LD = \frac{d\ln|I|}{dV}$$

The inverse logarithmic derivative (ILD) is simply the inverse function of LD:

$$ILD = \frac{dV}{d\ln|I|}$$

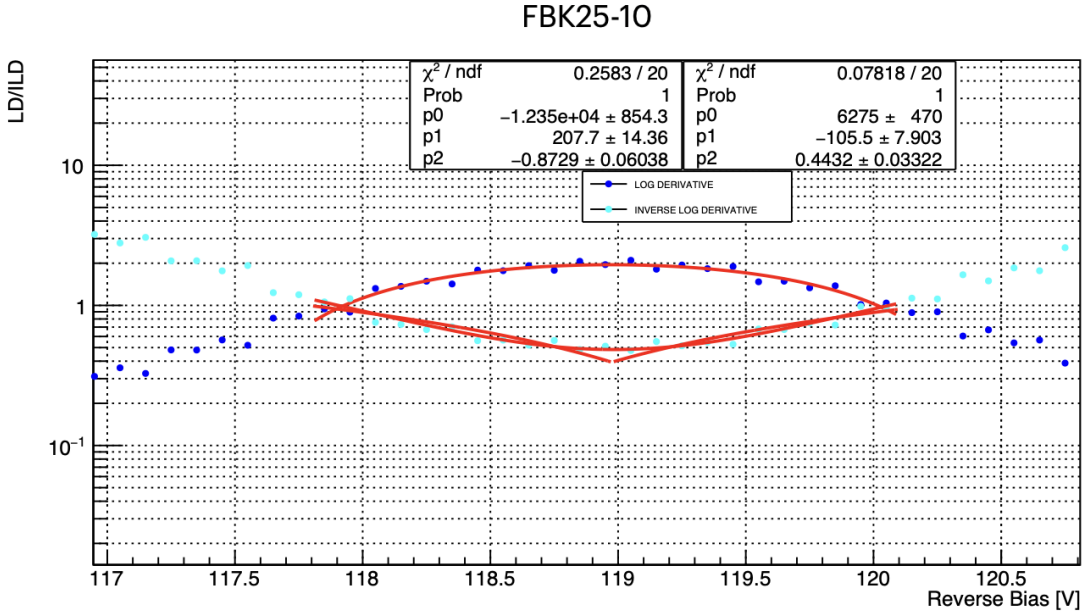

Figure B.4: This image shows the graph for the FBK25-10 sample. Two parameters are used: the number of points for the fit (N*) and the number of points for averaging (M). For each fit, a range was chosen around the breakdown voltage, which is independent for each sample. In some plots, averaging between nearby points was also performed to reduce high-frequency noise and achieve a better fit.

Finally, the line intersection method involves calculating the derivative point by point from the experimental data. In general, all three methods involve pointwise derivatives, so we expect LD to show a positive slope (linear in V) up to the breakdown voltage, where the curve will level off as this point represents a maximum of the derivative; thereafter, a negative slope is expected. By inverting the function, ILD will exhibit a

behavior that is exactly the mirror image: the slope will be negative up to the breakdown voltage (which represents the minimum point), and then become positive afterward. With the line intersection method, we expect a positive slope before the breakdown and a negative slope after the critical point. Ideally, the two lines will intersect at the sought point. A linear and parabolic fit is performed in a range around the breakdown voltage using parameters for the number of averaged points and the interval around the sought point. After obtaining results from the three methods, the average is calculated to obtain an experimental breakdown voltage value, which is associated with an uncertainty [4] An example of this procedure is shown in figure B.4.

[4] Calculated as $\epsilon = \frac{V_{max} - V_{min}}{2}$, where V_{max} is the highest breakdown voltage obtained from the three methods, and V_{min} is the lowest.

Appendix C

Details about study with iron-55 source

C.1 Decay of ^{55}Fe via Electron Capture

The isotope ^{55}Fe decays [83] primarily through the process of electron capture (EC) with half life of $T_{1/2}$ = 2.747 y, which can be described by the following reaction:

$$^{55}\text{Fe} + e^- \rightarrow ^{55}\text{Mn} + \nu_e \tag{C.1.1}$$

During this process, an electron from the K-shell is captured by the nucleus, leading to the conversion of a proton into a neutron and the emission of an electronic neutrino (ν_e). The decay product is ^{55}Mn, which is stable.

C.1.1 Energy of Emitted X-rays

After the electron capture, the vacancy in the K-shell is filled by an electron from a higher energy level, typically from the L-shell or M-shell. The transition of an electron from the L-shell to the K-shell results in the emission of characteristic K_α X-rays with an energy of approximately $\simeq$5.9 keV.

C.1.2 Auger Electrons

In some cases, instead of emitting X-rays, the energy released during the electron transition is transferred to another electron in the atom, which is then ejected. This ejected electron is known as an Auger electron. The energy of the Auger electrons emitted from ^{55}Fe decay is typically in the range of $\simeq$5 keV to $\simeq$6 keV.

C.1.3 Physics case:

As previously explained, the decay products include electrons and photons. Figure C.1 shows the products of 100 decays along with their energies and normalized rates.

An electron with an energy of 5-6 keV has a range of of about 2.9 g/cm^3 in air, which corresponds to 2.4 mm. Nevertheless, given that the source is situated at a distance of 3.3 mm from the detector, it is improbable that these electrons will reach the detector. The probability of the emission of a 126-keV photon is exceedingly low, rendering its contribution inconsistent.

	Energy (keV)	Emissions per 100 disint.
Auger electrons	0.47 - 0.67	140.2 (8)
	4.95 - 6.53	60.1 (5)
X-rays	0.56 - 0.72	0.524 (21)
	5.888	8.45 (14)
	5.899	16.57 (27)
	6.490	3.40 (7)
	6.535	
γ	125.959	1.3 (1) $\times 10^{-7}$

Figure C.1: ^{55}Fe emissions. Numbers in parentheses are the errors on the last digit(s) of the preceding value.

The attenuation coefficients in air for X-rays with energies of 1.0, 5.9, and 6.5 keV are 3600, 23.7, and 17.7 g/cm^3, respectively. It can therefore be concluded that X-rays within the specified energy ranges are capable of reaching the sensor. Nevertheless, the flux of photons with energies below 1 keV is deemed to be insignificant.

This leaves us with soft X-rays with energies of 5.9 and 6.5 keV. In this energy range, photoelectric absorption is the dominant process due to its significantly higher cross-section compared to scattering. As a result, an electron ejected via the photoelectric effect generates electron-hole (e-h) pairs along its path, with a range of up to 1 μm assuming an electron energy of approximately 6 keV. Given the presence of the gain layer, it is unlikely that the two peaks will be resolved distinctly.

C.2 Other results with source

In order not to weigh down the reading, this section comments on other results obtained from the source that do not fit into the main body of the text.

C.2.1 Comparison between 20-15 sensors

In general, the 20 and 15 μm sensors proved to be highly problematic due to the difficulty in discriminating the signal, which is already small due to the photon's passage, from the noise, as shown in figures C.2a and C.2b. Additionally, the high noise level due to the proximity to the breakdown voltage (BD) often limited the operational range, making it much narrower compared to the other sensors. As a result, it was not possible to observe a reliable signal region, especially for the FBK15 sensor.

In this section, we will nonetheless consider these sensors, even though the results are not entirely reliable, and report the findings obtained. Obviously, these sensors exhibit high gain values to compensate for the reduced thickness (looking to charged deposited), but this is still insufficient to obtain a large signal with photons, making them difficult to compare with other sensors, as shown in figures C.2a-C.2d. The charge values are reported in table 3.3. Additionally, as shown in table 3.4, from the acquisitions without a source, it can be observed that these sensors exhibit a higher average RMS noise (see also C.2d). As shown in Section 3.3.2.1, a graph in figure C.3 now illustrates the peak resolution at similar charge deposited levels between the two sensors.

The FBK20 sensor shows fairly decent results, being very similar in characteristics to the FBK25 sensor, but with, probably, a much higher gain which translates in higher charge and, most importantly, being able to extract some points in the working

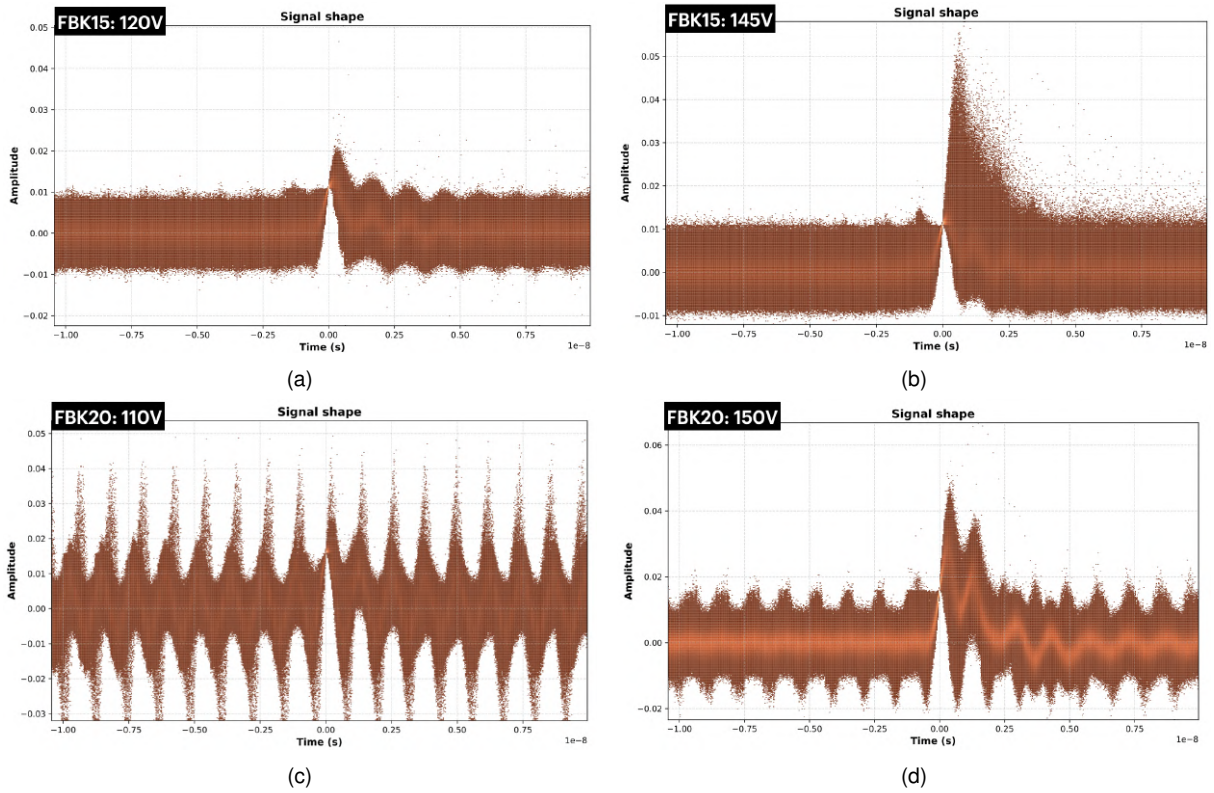

Figure C.2: (a) FBK15 with an applied bias of 120V: note how the signal appears as a peak barely distinguishable from the noise. (b) FBK15 with an applied bias of 145V: note how the signal appears reasonably large but very noisy, due to the proximity to the BD point. (c) FBK20 with an applied bias of 110V: note how signal is too noisy, in fact the electronic noise affects our mesurements. (d) FBK20 with an applied bias of 150V: The signal here, on the other hand, is well defined and manages to overcome the noise, but it remains a somewhat noisy device, note also the electronic feedback after the first peak.

region (WK) away from the BD range. This, overall, makes it show significantly better results than either the FBK25 or FBK15 sensors. However, as can be seen in the figures, C.2c-C.2d has a baseline that fluctuates a lot and especially when turning up the voltage, it can be seen that the problem of electronic noise feedback is present and still affects the measurements, making this device very noisy compared to the others. For example, the resolution on the 110V point extracted for the FBK20 sensor was extracted, with difficulty, from the sporadic events that managed to exceed the contribution of the baseline, however it is not really reliable given the low statistics. In contrast, the 150V point, which is clearly distinguishable from the baseline, is often confused by the electronic noise return peak, making the measurement, once again, unreliable. Thus we are only apparently able to explore a wide WR for the FBK20 (contrary to what is shown in 3.13), which like FBK15 actually narrows the working range to a very small one. So overall, the FBK25 sensor, although providing drastically worse results, is more reliable. On the other hand, the FBK15 sensor is undeniably unsuitable for studies, given its reduced thickness and the impossibility of using it in an adequate WK, given the very small signal.

Figures C.4a and C.4b provide further comparisons, reiterating that the sensor with the worst performance is the FBK15. It is interesting to note that with a 5 μm difference in thickness at similar charge deposited levels, the discrepancy is nearly 1000 electron-hole pairs, and the FBK15 sensor cannot even surpass 10^4 pairs, even near the BD. To further confirm this, the FBK15 also exhibits a worse S/N ratio, as expected. By examining figure 3.16, at a charge deposited of about 4.5-5.5 fC (where all 4 sensors are present), the FBK15 and FBK35 sensors are almost comparable in terms of pairs,

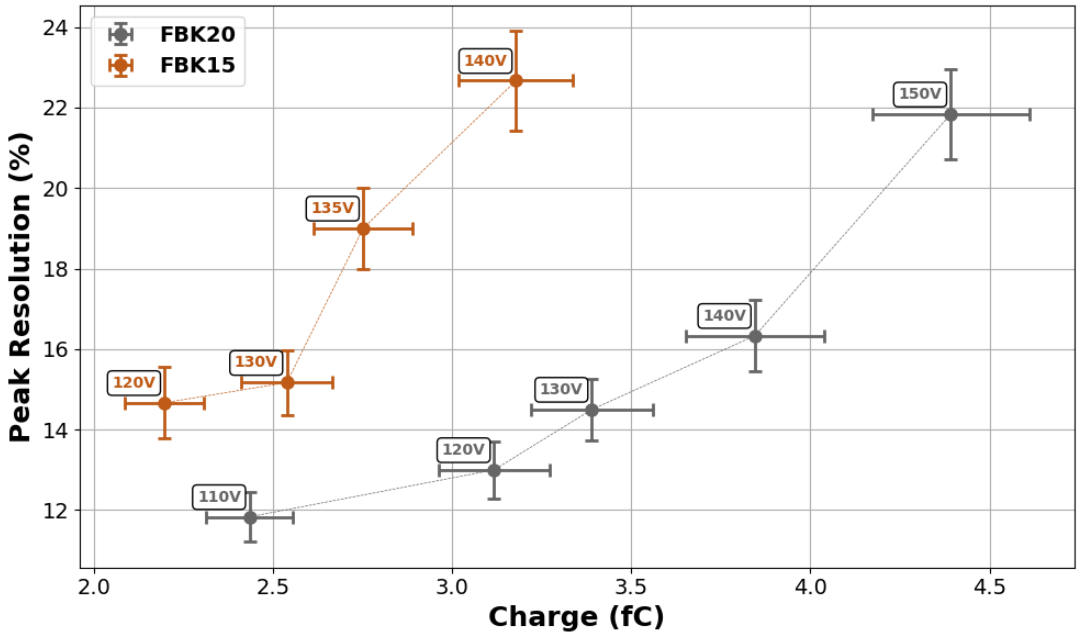

Figure C.3: Energy resolution at similar charge deposited levels between different sensors of 20 and 15 μm thickness.

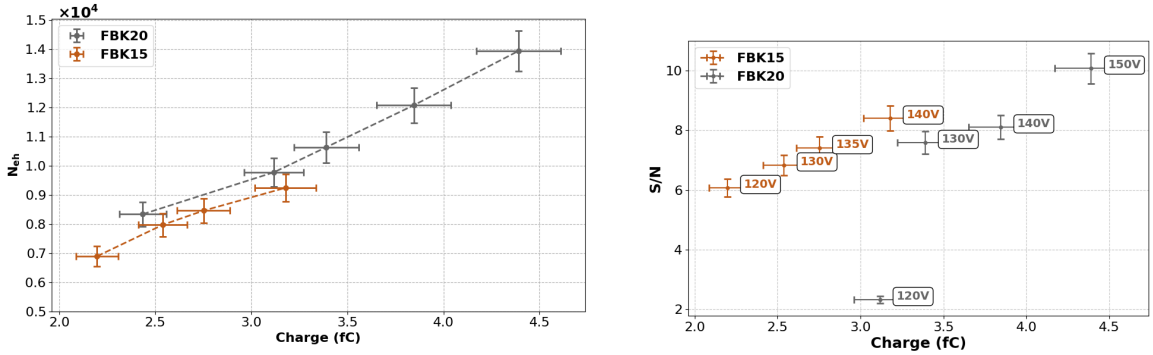

(a) (b)

Figure C.4: (a) Plot of electron-hole pairs as a function of various charge. (b) Plot of S/N as a function of charge for comparison purposes.

suggesting precisely a lower gain from the thicker sensor, whereas the FBK25 sensor appears to produce 3000 more e-h pairs than the other sensors, suggesting a drastically higher gain than the other sensors as well, and perhaps underlying the worse resolution, but at the same time the larger signal compared to the smaller sensors.

C.2.2 Scan in voltage of FBK35

This section shows the scan of a 35 μm sensor, and basically explains how far we were able to go, this study was conducted with a FBK35-8 sensor with a BD value of 253.7 ± 0.6 V. Now, the aim of the measurement is to try to understand what we observe as the voltage decreases, starting from around the potential of BD. As shown in figure C.5 the trend is as expected precisely because at the beginning, i.e. at 47% (120V) of the potential of BD, in full WR, the signal is very small and therefore the fit is difficult precisely because the signal mixes with the noise, while the signal then increases and the resolution improves, but moving towards the BD sub-enters the factors described previously in the appropriate section and therefore it becomes worse again.

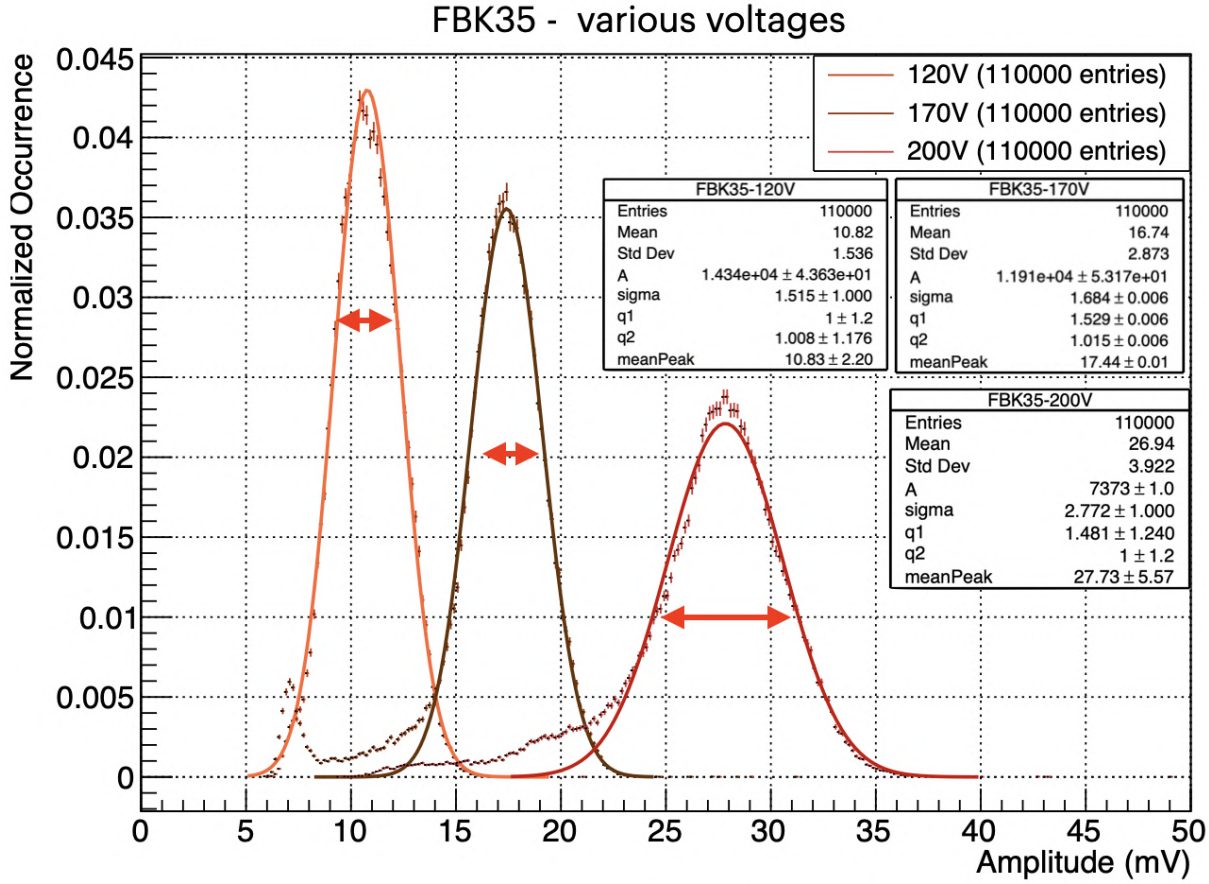

Figure C.5: Plot showing a comparison of amplitude distributions between three potentials, one in a region where I have a small signal (120V), one in the middle of the WR (170V) and one at the beginning of the BD range (200V).

So what we expect, and actually find, is a kind of parabola with a valley of stability. In fact, from a subsequent analysis of the resolution on the peak, we finally find a stable working region between 160 and 200 V, as shown in figure C.6. In figure C.6 we have reported the resolution on the peak as a function of charge deposited for the different voltages tested during the acquisition. In general, what can be said is that the points obtained after about 220V are not very reliable because the noise spoiled the measurement a lot. As we can see, in the stability region, it is shown how we manage to get below a resolution on the 10% on peak. Such a test with FBK prototype sensors was not possible with other sensors because we would never have been able to go that far down in the working region, in fact for the FBK25-20-15 we have already explored the minimum working region.

Not shown in this section, we repeated the scan also with a 50 μm sensor and

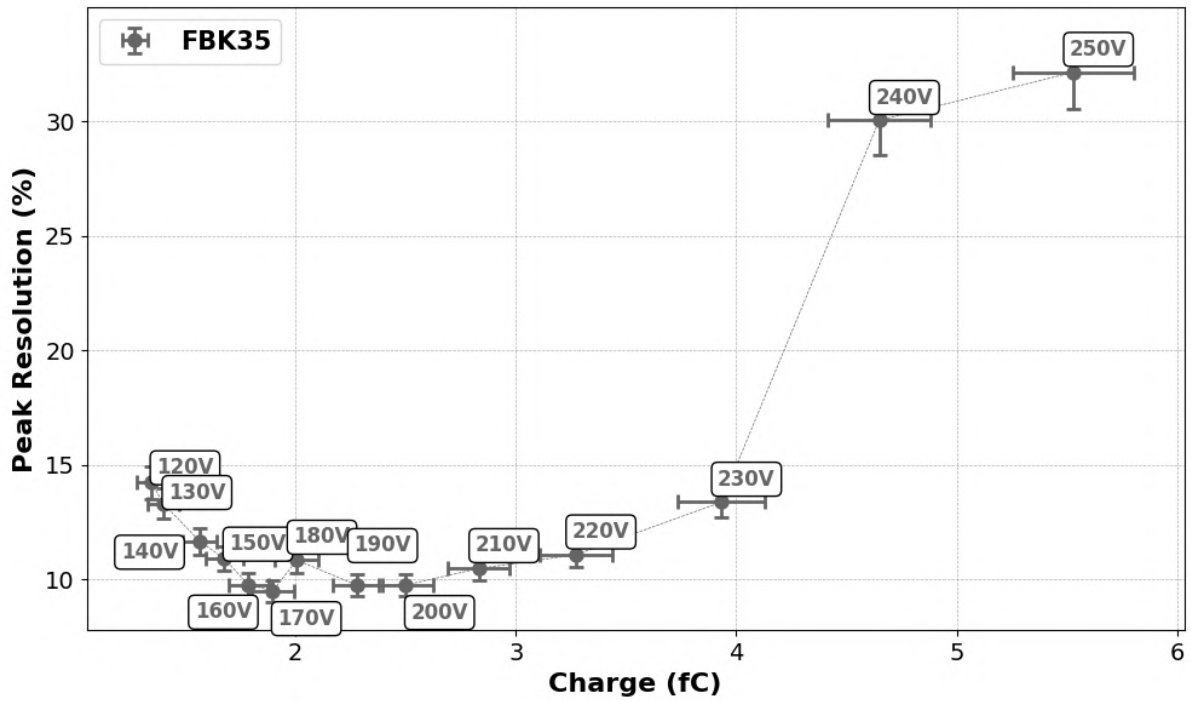

Figure C.6: Peak resolution as a function of gain; the applied voltage for each point is reported in the labels.

observed similar results, with the difference being that this time we were able to achieve about 35% of the BD value in the WR. So consistent with the fact that the greater the thickness, the greater the signal I get.

C.2.3 Signal at the same deposited charge: FBK35-25-20-15

In this section, the results obtained are compared considering a similar deposited charge value. The purpose of this section is illustrative, aiming to highlight the differences between sensors and, more specifically, to emphasize some key distinctions. A charge value of 4.5 fC was chosen for comparison.

It is clear that despite the high value of deposited charge, the 20 μm sensor shows a significant amount of noise, making this result, as previously mentioned, unreliable. Conversely, while the 15 μm sensor is also noisy, it is more affected by electronic feedback than baseline noise. Therefore, the results obtained from this sensor are more accurate, albeit worse, compared to the 20 μm sensor. In fact, when compared with the 25-35 μm sensors, it can be observed that the signal is smaller for the thinner sensors. The shape of signals of FBK35 and FBK25 is the one expected, as the higher amplitudes are less affected by noise; the average amplitude of signals is around 50 mV for the 25 μm sensor and 40 mV for the 35 μm one. The smaller value of amplitude at the same deposited charge for the thicker sensor is the result of a slightly lower gain, which is compensate by the higher thickness of the sensors. Finally, it is interesting to note, as previously expected, that the 25 μm sensor shows higher values of deposited charge, likely indicating that it has a higher internal gain compared to the 35 μm sensor. The observations made in this section apply in general. Lastly, in figure C.7, a plot is shown to illustrate how the amplitude distributions vary with the same deposited charge.

Finally, for the sake of comparison, what we obtain in the resolution from these data

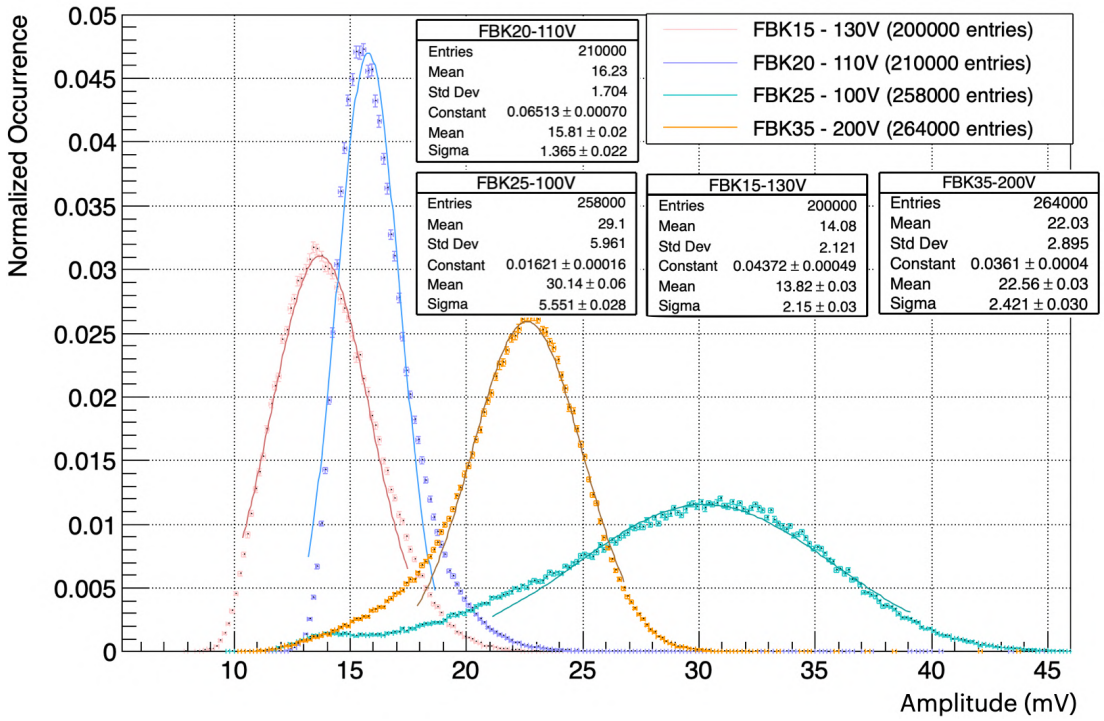

Figure C.7: Amplitude histogram for various sensors and voltages at the same deposited charge. The fit was performed using a Gaussian for illustrative purposes.

to this deposited charge are as follows, reported in descending order of thickness: 10.66%, 17.66%, 17.41%, 11.88% with an uncertainty reported at 10% of the value obtained from the $\frac{\sigma}{meanPeak}$ ratio. Hence, the discrepancy between the sensors of which we obtained a reliable measurement is around 7%, and simultaneously for the 15 μm sensor and the 25 μm sensor we found similar results between them.

Appendix D

Other results from studies with charged particles

D.1 Comparison between dFBK20 and sFBK20s

In this section, only graphs equivalent to what is shown in the section 3.4.3.1 for the 20 μm sensor will be shown (see figures D.1a-D.1d). For further explanations, please refer to the section 3.4.3.1 or the section D.3.

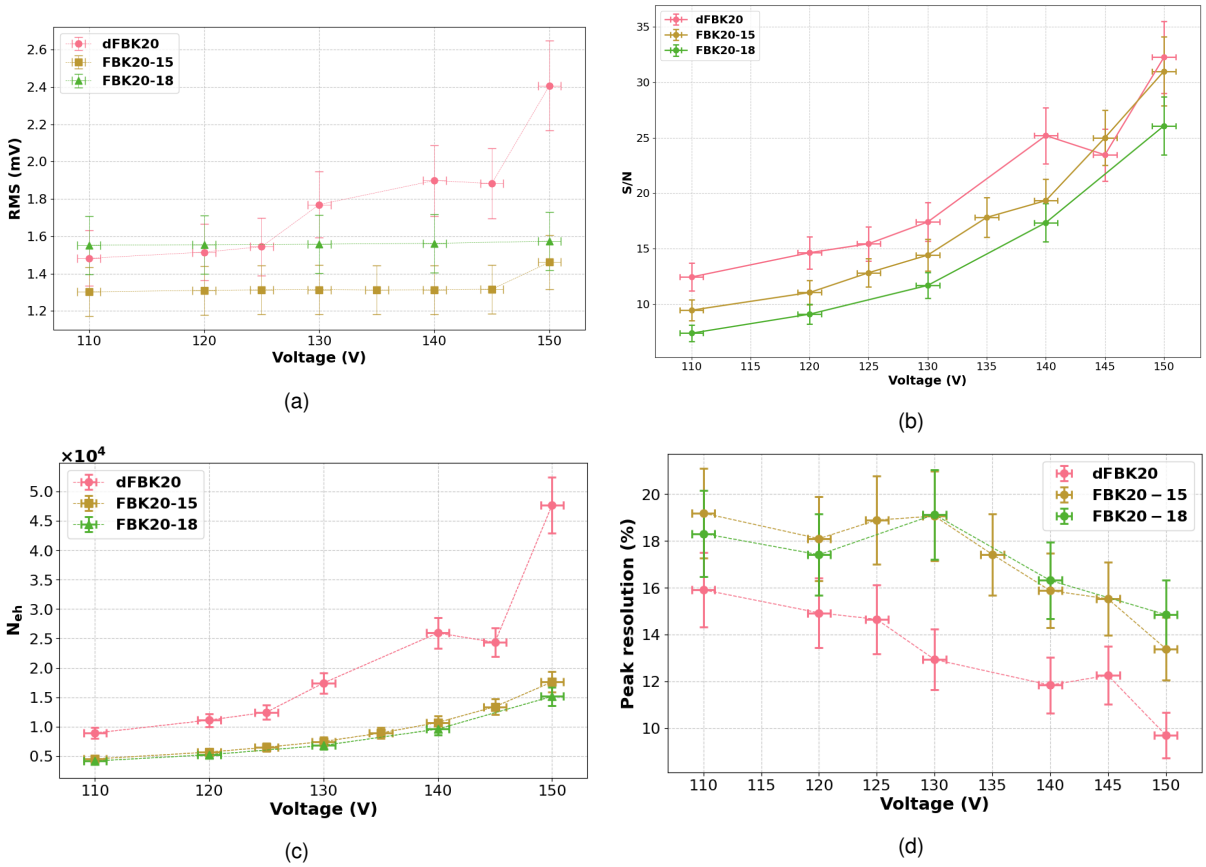

Figure D.1: (a) Plot of the average RMS for the sensors composing the double LGAD sensor, used for comparison at various voltages. (b) Plot of the MPV of the S/N for the sensors composing the double LGAD sensor, used for comparison at various voltages. (c) Plot of the MPV of N_{eh} pairs for the sensors composing the double LGAD module, used for comparison at various voltages. (d) Plot of the peak resolution for the sensors composing the double LGAD sensors, used for comparison as a function of voltage.

Please note that the trend is slightly anomalous (figures D.1a-D.1d) for the high voltage points for the dFBK20 sensor and therefore the end points were sometimes not considered for comparisons.

D.2 Skewness

This section presents the results obtained from an analysis of the skewness of charge deposition histograms.

When we talk about skewness, we refer to how data is distributed around the mean and how much this distribution deviates from perfect symmetry. A positive skewness indicates that the curve is asymmetric with a long tail extending to the right. Conversely, a negative skewness suggests that the curve has a long tail extending to the left. When skewness equals zero, it indicates that the distribution is symmetric, akin to a normal distribution.

Skewness can be calculated using the formula shown in D.2.1, where n is the number of observations, x_i are the observed values, $\bar{x}$ represents the mean, and σ is the standard deviation.

$$\text{Skew} = \frac{n}{(n-1)(n-2)} \sum \left(\frac{x_i - \bar{x}}{\sigma} \right)^3 \tag{D.2.1}$$

In the analysis that follows, skewness was computed using data from the charge deposition histogram through a root method.

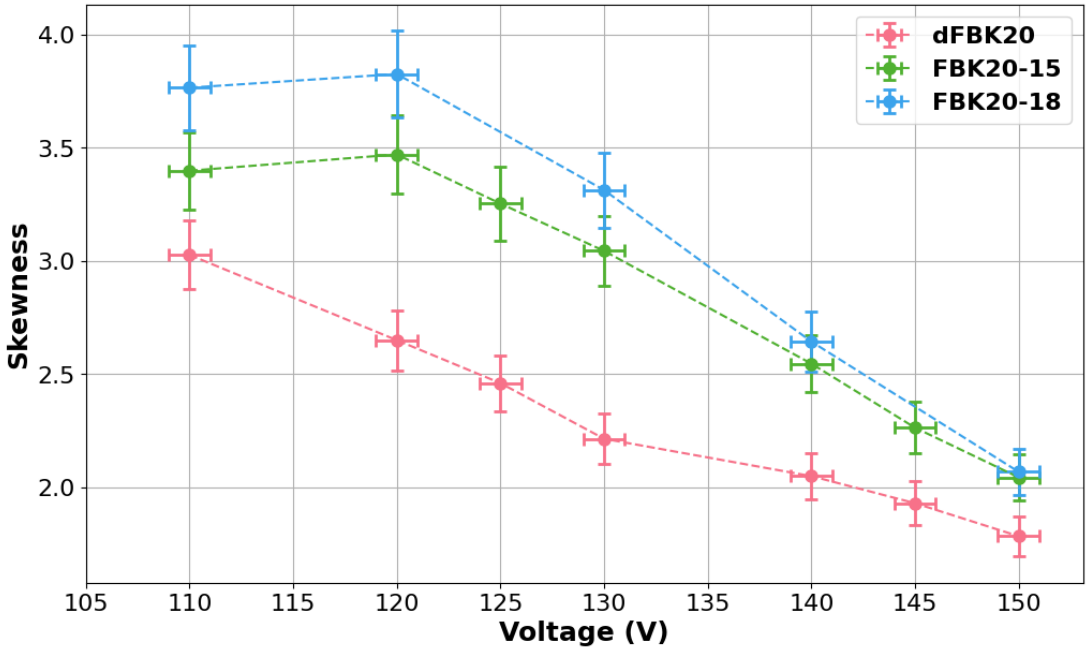

Figure D.2: Graph representing skewness as a function of voltage for an FBK20 sensor, comparing single and double configurations.

Skewness is an important parameter because a long tail (i.e., high skewness) indicates that our peak resolution measurement will generally yield poorer results. As shown in figure D.2, we observe that skewness decreases as voltage increases, and this trend aligns with the peak resolution. Additionally, a low skewness value indicates a more uniform avalanche gain distribution, with reduced fluctuations in the number of charge carriers. This is desirable for applications such as timing.

Furthermore, it is observed that increasing the sensor thickness also seems to reduce skewness, as shown in figure D.2. From a physical perspective, this could suggest that the energy deposition becomes more homogeneous as the thickness increases. Landau fluctuations in thinner sensors, however, being even smaller the signals obtained will affect the results more. This improvement in charge uniformity directly correlates with better peak resolution, as less skewness implies fewer distortions in the measured signal. For double LGADs, this is particularly beneficial, as both thickness and other design elements work together to enhance the overall timing and energy resolution of the sensor.

In fact, although not reported here, during the analysis for sensors with a thickness of 15 μm, we observed higher skewness values compared to those seen in figure D.2, particularly in the dFBK15, where the deviation was approximately 30 % higher than that observed for the corresponding FBK20.

D.3 Comparison of single FBK15s and FBK20s sensors

This section will present a comparison between the individual sensors that make up the double LGAD, aiming to highlight the differences between sensors of varying thickness in the study of charged particles as done, in section 3.4.3, however, detailed explanations will be omitted, focusing mainly on the comparison of the data. In table D.1 results achieved are reported as done in table 3.8.

One factor that has been overlooked so far is that the sensors forming the double LGAD, referred to as "Front" and "Back," will be analyzed separately in this section. The comparisons will involve all four sensors, but the results will be split in the graphs: Front sensors will be compared with other Front sensors, and similarly, Back sensors will be compared with other Back sensors. This is for readability reasons.

Sensor	*Voltage*	*R (%)*	*σ(ps)*	Sensor	Voltage	R (%)	σ(ps)
FBK15-13	100V	24.5	(95 $\pm$10)	FBK20-15	110V	19.1	(58 $\pm$6)
	110V	22.6	(84 $\pm$8)		120V	18.1	(42 $\pm$4)
	115V	21.5	(69 $\pm$7)		125V	18.9	(41 $\pm$4)
	120V	20.6	(53 $\pm$5)		130V	19.1	(37 $\pm$4)
	125V	20.5	(50 $\pm$5)		135V	17.4	(31 $\pm$3)
	130V	20.2	(45 $\pm$5)		140V	15.8	(28 $\pm$3)
	135V	18.9	(37 $\pm$4)		145V	15.5	(25 $\pm$3)
	140V	16	(31 $\pm$3)		150V	13.4	(23 $\pm$2)
FBK15-15	100V	22.1	(105 $\pm$10)	FBK20-18	110V	18.3	(60 $\pm$6)
	110V	22.3	(82 $\pm$8)		120V	17.4	(47 $\pm$5)
	120V	21.2	(67 $\pm$7)		130V	19.1	(40 $\pm$4)
	130V	19.9	(49 $\pm$5)		140V	16.3	(28 $\pm$3)
	140V	16.7	(31 $\pm$3)		150V	14.9	(21 $\pm$2)

Table D.1: Table showing peak resolution results for each voltage, comparing the single LGAD sensors. The uncertainty on R is not reported but is considered as the 10% of ratio σ/MPV not in percentages.

D.3.1 Peak resolution

Regarding the peak resolution, similar plots will be presented (see figures D.3a-D.3d) as shown in section 3.4.3.2.

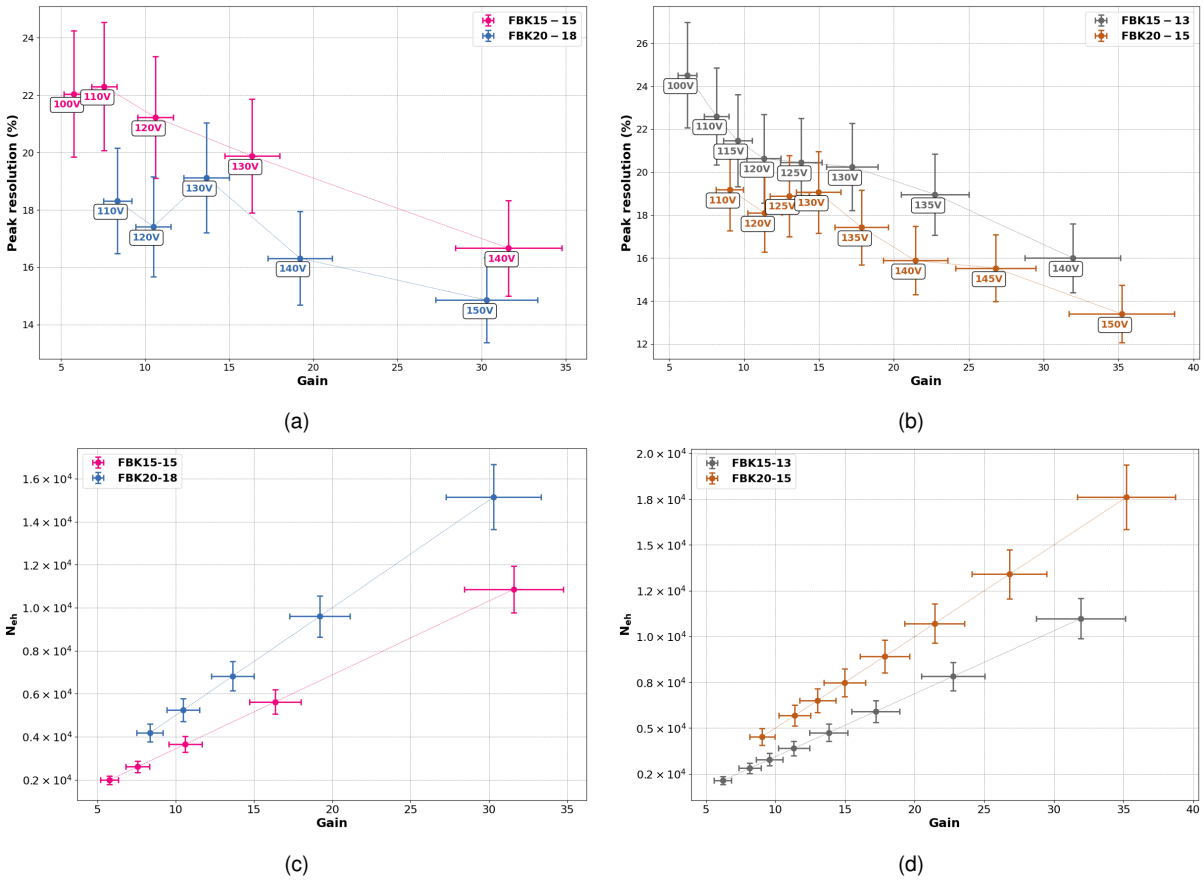

Figure D.3: In these figures a comparison among LGADs with thickness of 15 and 20 μm is reported. (a) Plot of peak resolution for back LGADs as a function of gain. (b) Plot of peak resolution for front LGADs as a function of gain. (c) Plot of N_{eh} as a function of gain for back LGADs. (d) Plot of N_{eh} as a function of gain for front LGADs.

From figures D.3a-D.3b, we observe that sensors with the same thickness exhibit similar behavior, with discrepancies between the curves remaining below 0.5%, as expected. On the other hand, the discrepancies between sensors of different thicknesses range from 2% to 4% on average, with occasional outliers around 5%. In general, thicker sensors tend to perform better, as anticipated. Regarding the results reported in figures D.3c-D.3d, we observe that the difference in N_{eh} values between sensors of different thicknesses spans from about 2000 (at low gains) to 6000 (at high gains). Interestingly, despite the increasing discrepancy in the number of electron-hole pairs generated as the gain rises, the discrepancy in energy resolution decreases with increasing gain. This is probably explained by the fact that, combined with a reduced thickness, at low gains the process is more sensitive to variations in sensor properties, such as doping concentration and electric field distribution, resulting in greater discrepancies in energy resolution between sensors of different thicknesses. However, as gain increases, the amplification process becomes more uniform throughout the device, reducing the relative impact of these variations.

Finally, in analogy to what was shown in D.4, a comparison of the amplitude distributions is reported, but this time with the same chosen gain, i.e., 15 in figure D.4. In this case, it is interesting to note that the MPV obtained from a sensor with a thickness

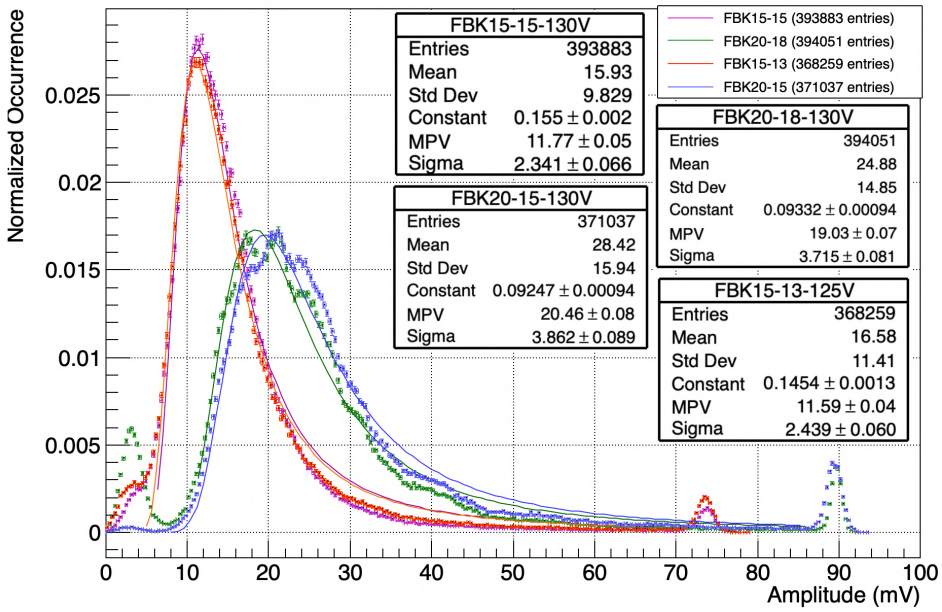

Figure D.4: Amplitude histograms of FBK15-15 (130 V), FBK15-13 (125 V), FBK20-15 (130 V), FBK-20-18 (130 V) sensors fit with a Landau distribution.

of 20 μm is twice as high as that obtained from a sensor with a thickness of 5 μm.

D.3.2 Time resolution

Regarding the time resolution, similar plots will be presented (see figures D.5a-D.5b) as shown in section 3.4.4.2.

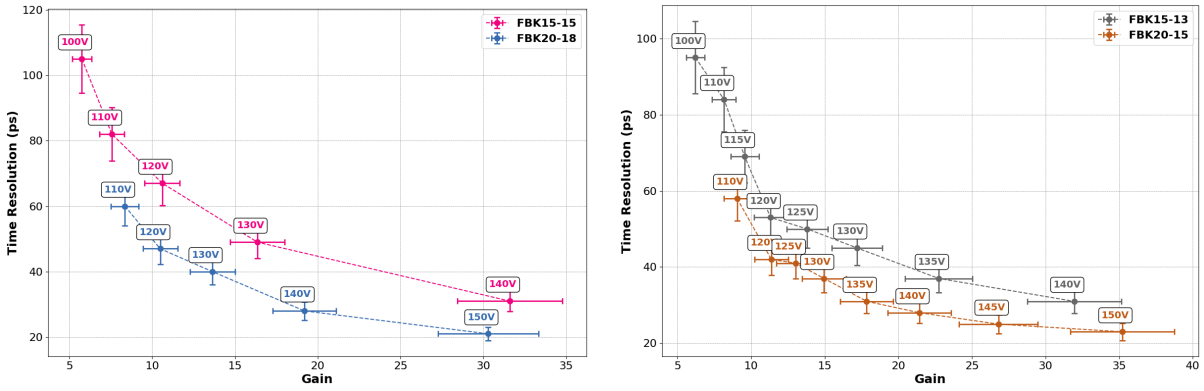

(a) (b)

Figure D.5: (a) Plot of time resolution for single LGAD sensors (back) with thicknesses of 15 and 20 μm as a function of gain. (b) Plot of time resolution for single LGAD sensors (front) with thicknesses of 15 and 20 μm as a function of gain.

As shown in figures D.5b and D.5a, the results obtained by the 20 μm sensors are very good even though they are in their single LGAD configuration; on the other hand, the 15 μm sensors show slightly worse performance, because although it is true that for thinner sensors the effect of the Landau fluctuations are smaller, at the same time the signal is much smaller and also the number of pairs produced (see figures D.3d and D.3c), so in general they have a greater impact on the results as already anticipated in section D.2. The S/N when compared between these two types of sensors goes from about 10-25 for the 20 μm sensors to about 5-15 for the 15 μm sensors, as shown

in figure 3.25b. However, the results for single sensors obtained are in line with what was expected and especially with previous studies with thicker sensors as shown in [76]-[77].

Bibliography

[1] "The ALICE experiment – A journey through QCD", ALICE Collaboration, https://arxiv.org/abs/2211.04384v1

[2] ALICE Collaboration, K. Aamodt et al., The ALICE experiment at the CERN LHC, JINST 3 (2008) S08002.

[3] F. Wilczek, Quantum field theory, Rev. Mod. Phys. 71 (1999) S85S95, arXiv:hep-th/9803075

[4] E. V. Shuryak, Theory of Hadronic Plasma, Sov. Phys. JETP 47 (1978) 212219.

[5] D. J. Gross, The discovery of asymptotic freedom and the emergence of QCD, Proc. Nat., Acad. Sci. 102 (2005) 90999108. https://doi.org/10.1073/pnas.0503831102

[6] A. Andronic, S. Borsanyi, Z. Fodor, J. N. Guenther, R. Kara, S. D. Katz, P. Parotto, A. Pasztor, C. Ratti, and K. K. Szabo, QCD Crossover at Finite Chemical Potential from Lattice Simulations, Phys. Rev. Lett. 125 (2020) 052001, arXiv:2002.02821 [hep-lat].

[7] P. F. Kolb and U. W. Heinz, Hydrodynamic description of ultrarelativistic heavy ion collisions, arXiv:nucl-th/0305084.

[8] JE. Annala, T. Gorda, A. Kurkela, J. NÍ attilÍ a, and A. Vuorinen, Evidence for quark-matter cores in massive neutron stars, Nature Phys. 16 (2020) 907910,arXiv:1903.09121 [astro-ph.HE].

[9] ALICE Collaboration, Letter of Intent for A Large Ion Collider Experiment [ALICE], CERN-LHCC-93-016, LHCC-I-4, tech. rep., CERN, Geneva, 1993, https://cds.cern.ch/record/290825.

[10] https://home.cern/resources/image/experiments/alice-images-gallery

[11] A. Kurkela and A. Mazeliauskas and J.-F. Paquet and S. Schlichting and D. Teaney, "Effective kinetic description of event-by-event pre-equilibrium dynamics in high-energy heavy-ion collisions", Phys. Rev. C 99, arXiv:1805.00961.

[12] P. Shukla, "Glauber model for heavy ion collisions from low energies to high energies", Springer Proc. Phys. 250, arXiv:nucl-th/0112039.

[13] F. Gelis and E. Iancu and J. Jalilian-Marian and R. Venugopalan, "The Color Glass Condensate", Ann. Rev. Nucl. Part. Sci. 60, arXiv:1002.0333.

[14] P. Huovinen and P. F. Kolb and U. W. Heinz and P. V. Ruuskanen and S. A. Voloshin, "Radial and elliptic flow at RHIC: further predictions", Phys. Lett. B 503, arXiv:hep-ph/0101136.

[15] P. F. Kolb and U. W. Heinz, "Hydrodynamic description of ultrarelativistic heavy-ion collisions", p. 634 (2003), arXiv:nucl-th/0305084.

[16] R. J. Fries, B. Muller, C. Nonaka, and S. A. Bass, Hadron production in heavy-ion collisions: Fragmentation and recombination from a dense parton phase, Phys. Rev. C 68 (2003) 044902, arXiv:nucl-th/0306027.

[17] M. I. Gorenstein, H. Stoecker, G. D. Yen, S. N. Yang, W. Greiner, "Chemical freezeout in relativistic A+A collisions: is it close to the QGP?", https://arxiv.org/abs/nucl-th/9711055.

[18] Johann Rafelski, Giorgio Torrieri, Jean Letessier, "Strangeness and QGP freeze-out dynamics", https://arxiv.org/abs/hep-ph/0104132

[19] G. S. Denicol and S. Jeon and C. Gale,"Transport Coefficients of Bulk Viscous Pressure in the 14-moment approximation", Phys. Rev. C 90, arXiv:1403.0962.

[20] Kevin Dusling, Ismail Zahed,"Parton energy loss in a classical strongly coupled QGP", https://doi.org/10.1016/j.nuclphysa.2009.12.006.

[21] Liliana Apolinário, Yen-Jie Lee, Michael Winn, "Heavy quarks and jets as probes of the QGP", https://doi.org/10.1016/j.ppnp.2022.103990.

[22] C. Gale and S. Jeon and B. Schenke, "Hydrodynamic Modeling of Heavy-Ion Collisions", Int. J. Mod. Phys. A 28, arXiv:1301.5893.

[23] S. Plumari, "Anisotropic flows and the shear viscosity of the QGP within an event-by-event massive parton transport approach", https://doi.org/10.1140/epjc/s10052-018-6510-9.

[24] Cristina Manuel, Juan M. Torres-Rincon, "Dynamical evolution of the chiral magnetic effect: Applications to the quark-gluon plasma", Phys. Rev. D 92, 074018, https://doi.org/10.1103/PhysRevD.92.074018.

[25] Rupa Chatterjee, Dinesh K. Srivastava, "Formation Time of QGP from Thermal Photon Elliptic Flow", https://doi.org/10.1016/j.nuclphysa.2009.10.043.

[26] Johann Rafelski, Michal Petrá, "Universal QGP Hadronization Conditions at RHIC and LHC", https://doi.org/10.1051/epjconf/20147806004.

[27] M. McNelis and U. Heinz, "Modified equilibrium distributions for Cooper-Frye particlization", Phys. Rev. C 103, 064903, https://doi.org/10.1103/PhysRevC.103.064903.

[28] ALICE Collaboration, N. Ahmad et al., ALICE: Technical proposal for a Large Ion collider Experiment at the CERN LHC, CERN-LHCC-95-71, tech. rep., Geneva, 1995, http://cds.cern.ch/record/293391.

[29] ALICE Collaboration, B. Abelev et al., Performance of the ALICE Experiment at the CERN LHC, Int.J.Mod.Phys. A29 (2014) 1430044, arXiv:1402.4476 [nucl-ex].

[30] Chiara Zampolli, "ALICE data processing for Run 3 and Run 4 at the LHC", https://arxiv.org/abs/2012.04391v1.

[31] ALICE Collaboration, "Letter of intent for ALICE 3: A next-generation heavy-ion experiment at the LHC", https://arxiv.org/abs/2211.02491v1

[32] A. Andronic et al. Eur. Phys. J. C76 (2016) no. 3,107, arXiv:1506.03981[nucl-ex].

[33] LHCb Collaboration, R. Aaij et al., Observation of an exotic narrow doubly charmed tetraquark, arXiv:2109.01038 [hep-ex].

[34] LHCb Collaboration, R. Aaij et al., Study of the doubly charmed tetraquark T_{cc}^{+}, arXiv:2109.01056 [hep-ex].

[35] Y. Kamiya, K. Sasaki, T. Fukui, T. Hyodo, K. Morita, K. Ogata, A. Ohnishi, and T. Hatsuda, Femtoscopic study of coupled-channel NΞ and $\Lambda\Lambda$ interactions, arXiv:2108.09644 [hep-ph].

[36] A. Beraudo et al. arXiv:1803.03824[nucl-th].

[37] V. Lysov, S. Pasterski, and A. Strominger Lows Subleading Soft Theorem as a Symmetry of QED" Phys. Rev. Lett., vol. 113 , no. 11, p. 111601, 2014.

[38] M. Mager, "ALPIDE, the Monolithic Active Pixel Sensor for the ALICE ITS upgrade",https://doi.org/10.1016/j.nima.2015.09.057.

[39] A. Beraudo et al., Extraction of Heavy-Flavor Transport Coefficients in QCD Matter, Nucl. Phys. A 979 (2018) 2186, arXiv:1803.03824 [nucl-th].

[40] R. Rapp, P. Gossiaux, A. Andronic, R. Averbeck, S. Masciocchi, A. Beraudo, E. Bratkovskaya, P. Braun-Munzinger, S. Cao, A. Dainese, and et al., Extraction of heavy-flavor transport coefficients in qcd matter, Nuclear Physics A 979 (Nov, 2018) 2186. http://dx.doi.org/10.1016/j.nuclphysa.2018.09.002.

[41] W. Busza, K. Rajagopal, and W. van der Schee, Heavy ion collisions: The big picture and the big questions, , Annual Review of Nuclear and Particle Science 68 no. 1, (Oct, 2018) 339376. http://dx.doi.org/10.1146/annurev-nucl-101917-020852.

[42] S. Cao, G.-Y. Qin, and S. A. Bass, Modeling of heavy-flavor pair correlations in Au-Au collisions at 200A GeV at the BNL Relativistic Heavy Ion Collider, Phys. Rev. C 92 no. 5, (2015) 054909, arXiv:1505.01869 [nucl-th].

[43] ALICE Collaboration, S. Acharya et al., Investigating charm production and fragmentation via azimuthal correlations of prompt D mesons with charged particles in pp collisions at s =13 TeV, arXiv:2110.10043 [nucl-ex].

[44] ALICE Collaboration, R. Vértesi, Jet measurements with ALICE: substructure, dead cone, charm jets, PoS LHCP2020 (2021) 143, arXiv:2009.11228 [hep-ex].

[45] NA50 Collaboration, M. C. Abreu et al., Evidence for deconfinement of quarks and gluons from the J/ψ suppression pattern measured in Pb + Pb collisions at the CERN SPS, Phys. Lett. B 477 (2000) 2836.

[46] Belle Collaboration, S. K. Choi et al., Observation of a narrow charmonium-like state in exclusive $B^{\pm} \to K^{\pm}\pi^{+}\pi^{+}J/\psi$ decays, Phys. Rev. Lett. 91 (2003) 262001, arXiv:hep-ex/0309032.

[47] LHCb Collaboration, R. Aaij et al., Observation of a narrow pentaquark state, $P_c(4312)^+$, and of two-peak structure of the $P_c(4312)^+$, Phys. Rev. Lett. 122 no. 22, (2019) 222001, arXiv:1904.03947 [hep-ex].

[48] G. Aarts and A. Nikolaev, Electrical conductivity of the quark-gluon plasma: perspective from lattice QCD, Eur. Phys. J. A 57 no. 4, (2021) 118, arXiv:2008.12326 [hep-lat].

[49] M. Greif, I. Bouras, C. Greiner, and Z. Xu, Electric conductivity of the quark-gluon plasma investigated using a perturbative QCD based parton cascade, Phys. Rev. D 90 no. 9, (2014) 094014, arXiv:1408.7049 [nucl-th].

[50] F. E. Low, Bremsstrahlung of very low-energy quanta in elementary particle collisions, Phys. Rev. 110 (1958) 974977.

[51] S. Weinberg, Infrared photons and gravitons, Phys. Rev. 140 (1965) B516B524.

[52] ALICE Collaboration, F. Carnesecchi, Performance of the ALICE Time-Of-Flight detector at the LHC, JINST 14 no. 06, (2019) C06023, arXiv:1806.03825[physics.ins-det].

[53] W. Snoeys et al., A process modification for CMOS monolithic active pixel sensors for enhanced depletion, timing performance and radiation tolerance, Nucl. Instrum. Meth. A 871 (2017) 9096.

[54] G. Pellegrini et al., Technology developments and first measurements of Low Gain Avalanche Detectors (LGAD) for high energy physics applications, Nucl. Instrum. Meth. A 765 (2014) 1216.

[55] N. Cartiglia et al., Design optimization of ultra-fast silicon detectors, Nucl. Instrum. Meth. A 796 (2015) 141148.

[56] Silicon photomultipliers (SiPM), https://doi.org/10.1016/B978-1-78242-445-1.00008-7.

[57] Stefan Gundacker and Arjan Heering,"The silicon photomultiplier: fundamentals and applications of a modern solid-state photon detector", https://doi.org/10.1088/1361-6560/ab7b2d.

[58] Donald A. Neamen, "SEMICONDUCTOR PHYSICS AND DEVICES Basic Principles", Fourth Edition.

[59] Dimitrijev, S., "Principles of Semiconductor Devices", New York: Oxford University Press, 2006.

[60] Pierret, "R. F. Semiconductor Device Fundamentals". Reading, MA: Addison-Wesley, 1996.

[61] Shockley, W. "Electrons and Holes in Semiconductors". New York: D. Van Nostrand, 1950.

[62] McKelvey, J. P. "Solid State Physics for Engineering and Materials Science". Malabar, FL.: Krieger Publishing, 1993.

[63] Navon, D. H. "Semiconductor Microdevices and Materials". New York: Holt, Rinehart& Winston, 1986.

[64] Hartmut F-W Sadrozinski et al., "4D tracking with ultra-fast silicon detectors", 2018 Rep. Prog. Phys. 81 026101, 10.1088/1361-6633/aa94d3.

[65] Hartmut F-W Sadrozinski, Abraham Seiden and Nicolò Cartiglia, "4D tracking with ultra-fast silicon detectors", 10.1088/1361-6633/aa94d3.

[66] H.F.-W. Sadrozinski, M. Baselga, S. Ely, "Sensors for ultra-fast silicon detectors", https://doi.org/10.1016/j.nima.2014.05.006.

[67] N. Wermes, "Recent Developments in Silicon Detectors, https://indico.cern.ch/event/391665/contributions/1827285/attachments/1228252/1799476/Wermes_Vienna_160215.pdf.

[68] H. F.W. Sadrozinski, Exploring charge multiplication for fast timing with silicon sensors, 20th RD50 Workshop, Bari, Italy, May 30 June 1, 2012, and references therein https://indico.cern.ch/conferenceOtherViews.py?view=standard&confId=175330.

[69] D. Breton et al, "Measurements of timing resolution of ultra-fast silicon detectors with the SAMPIC waveform digitizer", NIMA in press, 10.1016/j.nima.2016.08.019.

[70] N. Cartiglia, Properties of LGAD, TREDI 2017,https://indico.cern.ch/event/587631/contributions/2486830/attachments/1418630/2172952/Tredi_Cartiglia.pdf

[71] H. F.-W. Sadrozinski et al, "Measurements of the timing resolution of Ultra-Fast Silicon Detectors vs. Temperature, Fluence, Thickness, Manufacturer", 30th RD50 Workshop Krakow, Poland, June 5-7 2017. https://indico.cern.ch/event/637212/contributions/2608650/attachments/1470870/2276102/RD50-short.pdf

[72] Cenna, F., et al.: Weightfield2: A fast simulator for silicon and diamond solid state detector. NIMA 796, 149153 (2015). https://doi.org/10.1016/j.nima.2015.04.015

[73] N. Cartiglia, R. Arcidiacono, M. Baselga, R. Bellan et al.,"Design optimization of ultra-fast silicon detectors", https://doi.org/10.1016/j.nima.2015.04.025

[74] Gabriele Giacomini, Wei Chen, Francesco Lanni, Alessandro Tricoli, "Development of a technology for the fabrication of Low-Gain Avalanche Diodes at BNL", https://doi.org/10.1016/j.nima.2019.04.073.

[75] Gabriele Giacomini, Wei Chen, Francesco Lanni, Alessandro Tricoli, "Spectroscopic performance of Low-Gain Avalanche Diodes for different types of radiation", https://doi.org/10.1016/j.nima.2024.169605.

[76] F. Carnesecchi, S. Strazzi, A. Alici, R. Arcidiacono, G. Borghi, M. Boscardin, N. Cartiglia, M. Centis Vignali, D. Cavazza, G.-F. Dalla Betta, S. Durando, M. Ferrero, F. Ficorella, O. Hammad Ali, M. Mandurrino, A. Margotti, L. Menzio, R. Nania, L. Pancheri, G. Paternoster, G. Scioli, F. Siviero, V. Sola, M. Tornago, G. Vignola, "Beam test results of 25 μm and 35 μm thick FBK UFSD", https://doi.org/10.48550/arXiv.2208.05717.

[77] F. Carnesecchi, S. Strazzi, A. Alici, R. Arcidiacono, N. Cartiglia, D. Cavazza, S. Durando, M. Ferrero, A. Margotti, L. Menzio, R. Nania, B. Sabiu, G. Scioli, F. Siviero, V. Sola, G. Vignola, "A new Low Gain Avalanche Diode concept: the double-LGAD",http://dx.doi.org/10.1140/epjp/s13360-023-04621-x

[78] https://www.caen.it/sections/power-supply/

[79] url: https://download.tek.com/manual/6487-901-01(B-Mar2011)(Ref).pdf.

[80] http://www.minicircuits.com

[81] https://www.teledynelecroy.com/oscilloscope/wavesurfer-4000hd-oscilloscopes

[82] Johannes Bernhard, Filipa Carvalho, Sébastien Evrard, Erwan Harrouch, Giulia Romagnoli, "CERN Proton Synchrotron East Area Facility : Upgrades and renovation during Long Shutdown 2", http://dx.doi.org/10.23731/CYRM-2021-004.

[83] P. Cassette, "^{55}Fe - Comments on evaluation of decay data", Faculty of Physics, Sofia University, "St. Kliment Ohridski".